UNIVERSIDADE FEDERAL DE PELOTAS
Pró-Reitoria de Pesquisa e Pós-Graduação
Centro de Desenvolvimento Tecnológico
Programa de Pós-Graduação em Ciência e Engenharia de Materiais

Tese

Perovskita livre de chumbo para tratamento de efluentes e combate a patógenos: $NaNbO_3$ com propriedades fotocatalítica e antibacteriana

Daiane Fernandes Gonçalves

Pelotas, 2025

Daiane Fernandes Gonçalves

Perovskita livre de chumbo para tratamento de efluentes e combate a patógenos: $NaNbO_3$ com propriedades fotocatalítica e antibacteriana

Tese apresentada ao Programa de Pós-Graduação em Ciência e Engenharia de Materiais do Centro de Desenvolvimento Tecnológico da Universidade Federal de Pelotas, como requisito parcial à obtenção do título de Doutora em Ciência e Engenharia de Materiais.

Orientador: Prof. Dr. Sergio da Silva Cava

Coorientadora: Profª. Drª. Cristiane Wienke Raubach

Pelotas, 2025

Universidade Federal de Pelotas / Sistema de Bibliotecas
Catalogação da Publicação

G635p Gonçalves, Daiane Fernandes

Perovskita livre de chumbo para tratamento de efluentes e combate a patógenos [recurso eletrônico] : $NaNbO_3$ com propriedades fotocatalítica e antibacteriana / Daiane Fernandes Gonçalves ; Sergio da Silva Cava, orientador ; Cristiane Wienke Raubach, coorientadora. — Pelotas, 2025.
157 f. : il.

Tese (Doutorado) — Programa de Pós-Graduação em Ciência e Engenharia de Materiais, Centro de Desenvolvimento Tecnológico, Universidade Federal de Pelotas, 2025.

1. Perovskita. 2. Niobato de sódio. 3. Síntese hidrotérmica assistida por micro-ondas. 4. Fotocatálise heterogênea. 5. Atividade antibacteriana. I. Cava, Sergio da Silva, orient. II. Raubach, Cristiane Wienke, coorient. III. Título.

CDD 620.11063

Elaborada por Simone Godinho Maisonave CRB: 10/1733

Daiane Fernandes Gonçalves

Perovskita livre de chumbo para tratamento de efluentes e combate a patógenos: $NaNbO_3$ com propriedades fotocatalítica e antibacteriana

Tese aprovada, como requisito parcial para obtenção do grau de Doutora em Ciência e Engenharia de Materiais, Programa de Pós-Graduação em Ciência e Engenharia de Materiais, Centro de Desenvolvimento Tecnológico, Universidade Federal de Pelotas.

Data da defesa: 30 de abril de 2025.

Banca examinadora:
Prof. Dr. Sergio da Silva Cava (Orientador)
Doutor em Química pela Universidade Federal de São Carlos.

Profª. Drª. Cristiane Wienke Raubach (Coorientadora)
Doutora em Química pela Universidade Federal de São Carlos.

Prof. Dr. Alejandro Cristians Rios Cuadros
Doutor em Física pela Universidade Federal de Minas Gerais.

Prof. Dr. Maurício Jeomar Piotrowski
Doutor em Física pela Universidade Federal de Santa Maria.

Prof. Dr. Wiliam Boschetti
Doutor em Química pela Universidade Federal do Rio Grande do Sul.

Prof. Dr. Mateus Meneghetti Ferrer (SUPLENTE)
Doutor em Química pela Universidade Federal de São Carlos.

Prof. Dr. Pedro Lovato Gomes Jardim (SUPLENTE)
Doutor em Física pela Universidade Federal do Rio Grande do Sul.

Dedico este trabalho a Deus, dono de toda a ciência.

Agradecimentos

Agradeço primeiramente a Deus, pelas bênçãos que tem derramado sobre minha vida. Pela saúde, pelo amor e pela paz que só Ele pode oferecer. Tudo o que sou e tenho é fruto da Sua graça e bondade.

À minha amada mãe, Eliane, meu maior exemplo e a base para realização de todos os meus sonhos.

Com carinho aos colegas do grupo de pesquisa Crescimento de Cristais Avançados e Fotônica (CCAF). Em especial à minha amiga Thissiana da Cunha Fernandes.

À minha coorientadora, Profª. Drª. Cristiane Wienke Raubach, por acreditar em mim e guiar meus passos. Não é o fim da nossa caminhada, temos uma bela jornada ainda pela frente.

Minha mais sincera gratidão ao meu orientador, Prof. Dr. Sergio da Silva Cava, pelo comprometimento e paciência. Se não fosse por ele, eu não estaria completando esta etapa tão importante na minha vida.

Aos Professores Dr. Carlos Frederico de Oliveira Graeff, Dr. Eduardo Ceretta Moreira e Dr. Valmor Mastelaro, que foram fundamentais para conclusão deste trabalho. Sem o apoio de vocês, eu não teria conseguido chegar até aqui.

À Universidade Federal de Pelotas pela oportunidade de realização do doutorado.

À Fundação Coordenação de Aperfeiçoamento de Pessoal de Nível Superior - Brasil (CAPES) pela bolsa concedida.

Ao Conselho Nacional de Desenvolvimento Científico e Tecnológico (CNPq) e à Fundação de Amparo à Pesquisa do Estado do Rio Grande do Sul (FAPERGS) pelo financiamento de projetos que possibilitaram a conclusão desta pesquisa.

Por fim, mas não menos importante, agradeço aos meus amigos e família.

Ninguém vence sozinho; portanto, a conclusão desta etapa é uma vitória de todos nós, foi um trabalho em equipe.

Obrigada a todos.

Seja você quem for, seja qual for a posição social que você tenha na vida, a mais alta ou a mais baixa, tenha sempre como meta muita força, muita determinação e sempre faça tudo com muito amor e com muita fé em Deus, que um dia você chega lá. De alguma maneira você chega lá.

(Ayrton Senna)

Resumo

GONÇALVES, Daiane Fernandes. **Perovskita livre de chumbo para tratamento de efluentes e combate a patógenos: $NaNbO_3$ com propriedades fotocatalítica e antibacteriana.** Orientador: Prof. Dr. Sergio da Silva Cava. 2025. 157 f. Tese (Doutorado em Ciência e Engenharia de Materiais) - Centro de Desenvolvimento Tecnológico, Universidade Federal de Pelotas, Pelotas, 2025.

A fotocatálise heterogênea tem se consolidado como uma tecnologia eficaz para o enfrentamento de desafios ambientais, especialmente no tratamento de efluentes contendo poluentes recalcitrantes. Entre os materiais investigados como fotocatalisadores, o niobato de sódio ($NaNbO_3$), um semicondutor com estrutura cristalina do tipo perovskita, tem despertado interesse devido às suas propriedades físico-químicas favoráveis para este fim. Embora propriedades antibacterianas representem um diferencial importante nos materiais devido ao avanço de cepas resistentes, o uso do $NaNbO_3$ em aplicações antimicrobianas ainda é pouco explorado. Diante disso, o objetivo desta tese, estruturada em cinco artigos científicos, foi investigar as propriedades fotocatalítica e antibacteriana do $NaNbO_3$ e de suas modificações estruturais e composicionais, visando sua aplicação na remoção de poluentes emergentes em meio aquoso e no combate a bactérias patogênicas. No primeiro artigo, o $NaNbO_3$ foi sintetizado pelo método hidrotérmico assistido por micro-ondas (MHAM), seguido de tratamento térmico, resultando em nanofios e nanograos com elevada atividade fotocatalítica. O aumento da temperatura de calcinação promoveu a conversão dos nanofios em nanograos, que apresentaram desempenho superior na degradação do corante Rodamina B (RhB) sob luz UV. A elevada eficiência fotocatalítica foi atribuída à combinação entre alta cristalinidade e morfologia favorável. No segundo artigo, foi desenvolvido um fotocatalisador heteroestruturado a partir dos nanograos de $NaNbO_3$ previamente obtidos e eumelanina (pigmento extraído de resíduo de cabelo humano). A ampla absorção óptica da eumelanina, aliada à separação eficiente de cargas promovida pela junção dos materiais, possibilitou a degradação do RhB sob luz visível. Nos três artigos seguintes, o $NaNbO_3$ foi sintetizado, também pelo MHAM, e a influência da dopagem com Cu(II), Al(III) e Zn(II) na sua atividade fotocatalítica foi analisada. A inserção desses dopantes promoveu alterações na simetria cristalina e influenciou significativamente as propriedades ópticas da perovskita. Em concentrações otimizadas, a dopagem reduziu o *band gap* e a taxa de recombinação das cargas fotogeradas, resultando em maior eficiência na degradação do RhB. Nos estudos com Cu(II) e Zn(II), também foi avaliada a atividade antibacteriana. A dopagem com Cu(II) resultou na inibição do crescimento da bactéria *Escherichia coli* (*E. coli*). No estudo com Zn(II), o $NaNbO_3$ puro exibiu ação antibacteriana expressiva contra *E. coli*, *Staphylococcus aureus* (*S. aureus*) e *Klebsiella pneumoniae (K. pneumoniae)*, enquanto a amostra dopada também inibiu o crescimento bacteriano, mas com eficácia dependente da concentração. Dessa forma, os resultados obtidos evidenciam o grande potencial do $NaNbO_3$ como fotocatalisador para purificação de águas residuais e como agente antimicrobiano. Adicionalmente, os artigos produzidos no âmbito desta tese foram os primeiros a reportar a atividade antibacteriana do $NaNbO_3$ puro, sem estímulo adicional, frente à *E. coli*, bem como a demonstrar sua eficácia contra *K. pneumoniae* e *S. aureus*.

Palavras-chave: perovskita; niobato de sódio; síntese hidrotérmica assistida por micro-ondas; fotocatálise heterogênea; atividade antibacteriana.

Abstract

GONÇALVES, Daiane Fernandes. **Lead-free perovskite for wastewater treatment and pathogen control: $NaNbO_3$ with photocatalytic and antibacterial properties** Advisor: Prof. Dr. Sergio da Silva Cava. 2025. 157 f. Thesis (PhD in Science and Materials Engineering) - Technological Development Center, Federal University of Pelotas, Pelotas, 2025.

Heterogeneous photocatalysis has been established as an effective technology for addressing environmental challenges, particularly in the treatment of wastewater containing recalcitrant pollutants. Among the materials investigated as photocatalysts, sodium niobate ($NaNbO_3$), a semiconductor with a perovskite-type crystalline structure, has attracted interest due to its physicochemical properties favorable for this purpose. Although antibacterial properties represent an important advantage in materials due to the rise of resistant strains, the use of $NaNbO_3$ in antimicrobial applications remains underexplored. In this context, the aim of this thesis, structured in five papers, was to investigate the photocatalytic and antibacterial properties of $NaNbO_3$ and its structural and compositional modifications, aiming at its application in the removal of emerging pollutants from aqueous media and in the combat against pathogenic bacteria. In the first paper, $NaNbO_3$ was synthesized using the microwave-assisted hydrothermal method (MAHM), followed by thermal treatment, resulting in nanowires and nanograins with high photocatalytic activity. Increasing the calcination temperature promoted the transformation of nanowires into nanograins, which exhibited superior performance in the degradation of Rhodamine B (RhB) under UV light. The high photocatalytic efficiency was attributed to the combination of high crystallinity and favorable morphology. In the second paper, a heterostructured photocatalyst was developed from the previously obtained $NaNbO_3$ nanograins and eumelanin (a pigment extracted from human hair waste). The broad optical absorption of eumelanin, combined with the efficient charge separation promoted by the junction of the materials, enabled the degradation of RhB under visible light. In the following three papers, $NaNbO_3$ was synthesized also synthesized via the MAHM, and the influence of doping with Cu(II), Al(III), and Zn(II) on its photocatalytic activity was investigated. The insertion of these dopants promoted changes in the crystal symmetry and significantly influenced the optical properties of $NaNbO_3$. At optimized concentrations, doping reduced the band gap and the recombination rate of the photogenerated charges, resulting in greater efficiency in the degradation of RhB. In the studies with Cu(II) and Zn(II), antibacterial activity was also evaluated. Doping with Cu(II) resulted in the inhibition of *Escherichia coli* (*E. coli*) growth. In the study involving Zn(II), pure $NaNbO_3$ exhibited significant antibacterial activity against *E. coli*, *Staphylococcus aureus* (*S. aureus*), and *Klebsiella pneumoniae* (*K. pneumoniae*), while the doped sample also inhibited bacterial growth, although its effectiveness was dependent on the sample concentration. Thus, the results obtained highlight the great potential of $NaNbO_3$ as a photocatalyst for wastewater purification and as an antimicrobial agent. Additionally, the papers produced within the scope of this thesis were the first to report the antibacterial activity of pure $NaNbO_3$, without additional stimulation, against *E. coli*, as well as to demonstrate its effectiveness against *K. pneumoniae* and *S. aureus*.

Keywords: perovskite; sodium niobate; microwave-assisted hydrothermal synthesis; heterogeneous photocatalysis; antibacterial activity.

Sumário

1 Introdução

A poluição ambiental é um desafio global que ameaça a sobrevivência de ecossistemas inteiros. Dentre os diversos problemas ambientais que, consequentemente, comprometem a qualidade de vida, a contaminação da água é uma das preocupações mais significativas. Isso se deve à importância vital desse recurso natural para a sustentação da vida na Terra. Entre os poluentes emergentes, os corantes orgânicos — amplamente utilizados em indústrias alimentícias, papeleiras, farmacêuticas, têxteis, entre outras — se destacam por sua elevada toxicidade, persistência ambiental e baixa biodegradabilidade [1-3]. Um exemplo representativo é o corante rodamina B (RhB), que induz efeitos cancerígenos e mutagênicos na biodiversidade. Pertencente à classe dos corantes xantenos, possui anéis aromáticos em sua estrutura que lhe conferem maior estabilidade e, portanto, maior resistência à degradação. Além de representar um contaminante real relevante, o RhB é comumente utilizado como molécula modelo para testar a eficiência de materiais fotocatalíticos, devido à sua alta estabilidade química, forte absorção na região do visível que possibilita fácil monitoramento óptico, ampla referência na literatura e capacidade de simular outros compostos poluentes [4-6]. Dessa forma, a remoção do RhB de águas residuais não apenas é crucial para a preservação dos recursos hídricos, como também permite avaliar de maneira padronizada e comparável o desempenho de novos fotocatalisadores aplicáveis à remediação ambiental.

Dentre as tecnologias para o tratamento de efluentes, os processos oxidativos avançados (POAs), ou *Advanced Oxidation Processes (AOPs),* como são internacionalmente conhecidos, têm se destacado por sua capacidade de degradar poluentes recalcitrantes [7,8]. Em especial, a fotocatálise heterogênea é uma abordagem que apresenta elevada eficácia, promovendo a total degradação destas substâncias ou transformando-as em menos tóxicas ou inócuas. O mecanismo fotocatalítico consiste na ativação de um fotocatalisador, geralmente semicondutores, por fótons com energia suficiente para excitar os elétrons da banda de valência (BV) para a banda de condução (BC). Os elétrons fotoexcitados podem então participar de reações de redução na BC, enquanto as lacunas geradas na BV podem participar de reações de oxidação. Como resultado, esta dinâmica é capaz de degradar diferentes compostos contaminantes [9-11].

A eficiência da fotocatálise é influenciada por diversos fatores, especialmente pelas propriedades do fotocatalisador. Características importantes incluem, por exemplo, o tamanho das partículas: quanto menores, maior é a área superficial, favorecendo as reações fotocatalíticas, uma vez que estas ocorrem na superfície do semicondutor [12]. Assim, o desenvolvimento de sínteses que permitam o controle da morfologia se mostra altamente vantajoso. Além desta propriedade, uma limitação significativa de muitos fotocatalisadores é sua ativação restrita à luz ultravioleta (UV). Isso representa um desafio considerável para aplicações sob luz natural, pois a radiação UV corresponde a menos de 5% do espectro total que atinge a superfície da Terra [13]. Outro desafio a ser superado é a rápida recombinação dos pares elétron/lacuna (e^-/h^+), que reduz o tempo de vida útil destas cargas [14]. Além disso, muitos fotocatalisadores sofrem fotocorrosão (degradação do material devido à interação com a luz), o que limita sua reutilização em ciclos sucessivos [15].

Frente a essas limitações, estratégias têm sido exploradas para aprimorar a eficiência dos fotocatalisadores e viabilizar sua aplicação prática. Entre elas, a dopagem tem sido reconhecida como um método eficaz [16-18]. A inserção de íons dopantes na rede semicondutora pode reduzir o *band gap*, o que diminui a energia necessária para gerar os pares e^-/h^+. Adicionalmente, a recombinação das cargas fotogeradas pode ser retardada, devido a formação de níveis de energia intermediários. Outra estratégia que tem mostrado avanços significativos é o desenvolvimento de heteroestruturas, ou seja, que envolvem a combinação de dois ou mais materiais distintos [19,20]. Esse tipo de estrutura permite a migração eletrônica entre os componentes envolvidos, o que contribui para retardar a recombinação dos portadores de carga. Ademais, um dos materiais pode absorver luz em comprimentos de onda maiores, ampliando sua resposta à radiação luminosa.

Um dos semicondutores mais utilizados em processos fotocatalíticos é o dióxido de titânio (TiO_2). No entanto, apresenta algumas limitações como a rápida recombinação das cargas fotogeradas, o que tem motivado a busca por novos materiais com desempenho aprimorado. Nesse contexto, o niobato de sódio ($NaNbO_3$) tem emergido como uma alternativa promissora. Trata-se de um semicondutor com estrutura do tipo perovskita, que apresenta diversas propriedades de interesse tecnológico, incluindo elevada atividade fotocatalítica [21–26]. É termodinamicamente estável, resistente à corrosão, possui baixa toxicidade e é

insolúvel em água — características que o tornam altamente atrativo para seu uso como fotocatalisador. Além disso, pode ser obtido em diferentes formatos de partículas, como fios/hastes (unidimensional), cubos e grãos, dependendo da rota sintética empregada, o que influencia diretamente sua resposta fotocatalítica [22,27-29]. Pesquisas demonstram que o $NaNbO_3$ unidimensional (1D) apresenta atividade fotocatalítica superior em comparação às partículas cúbicas, que correspondem à sua forma natural, devido à maior probabilidade de ocorrência de sítios ativos [22,26]. No que diz respeito à dopagem, estudos têm investigado a inserção de íons na estrutura do $NaNbO_3$, mas com foco predominante em análises estruturais ou luminescentes [30-38]. Poucos trabalhos, entretanto, exploram o impacto da dopagem na atividade fotocatalítica; para esse fim, estudos com N, Ca, K, V e Ta já foram conduzidos [39-43]. Quanto ao desenvolvimento de fotocatalisadores heteroestruturados baseados em $NaNbO_3$, materiais como In_2O_3, ZnO, CdS, Bi_2O_3, Cu_2O, Ru, Au, BiOI, Ag_2O, Ag_2SO_3, Bi_2WO_6, g-C_3N_4, Fe_2O_3 e $CuBi_2O_4$ foram utilizados [13,14,40,44-55]. Esse panorama destaca o potencial de investigar uma gama de íons dopantes e combinar o $NaNbO_3$ com outros materiais, principalmente de menor custo, visando à obtenção de compósitos inovadores e eficientes.

Apesar do crescente interesse em materiais antibacterianos, o uso do $NaNbO_3$ para essa finalidade ainda é pouco explorado. Por exemplo, *Escherichia coli* (*E. coli*) foi inativada via fotopiezocatálise usando $NaNbO_3$ e $NaNbO_3$/ZnO [56,57], enquanto o $NaNbO_3$/CdS provou ser eficaz contra *Salmonella* através do efeito piroelétrico [58]. Resultados promissores contra *E. coli* também foram obtidos usando $NaNbO_3$ polarizado modificado com Ca e Mg [59]. Na ausência de estímulos externos, *E. coli* e *Staphylococcus aureus* (*S. aureus*) foram inativadas com $BiFeO_3$/$NaNbO_3$ [60]. Diante disso, a avaliação da atividade antibacteriana intrínseca do $NaNbO_3$, sem estímulos externos, configura uma abordagem relevante para viabilizar aplicações com menor complexidade operacional. Ademais, a dopagem com certos íons pode representar uma estratégia eficaz para intensificar tal atividade. Elementos como Cu(II) e Zn(II), por exemplo, são conhecidos por sua potente ação contra diversas bactérias, mesmo em concentrações relativamente baixas. Esses íons podem penetrar nas células e alterar a síntese proteica, promover a degradação do DNA, interferir em processos metabólicos essenciais e na função da membrana. Tais interações provocam danos irreversíveis, culminando na morte celular ou na inibição

do crescimento bacteriano [61-63]. Estudos recentes têm explorado suas incorporações em diversas matrizes, como polímeros, carvão ativado, complexos orgânicos e semicondutores, demonstrando resultados notáveis [64-71].

Considerando o exposto, este trabalho foi conduzido com o objetivo de contribuir para o avanço do desenvolvimento de materiais fotocatalíticos e antibacterianos. A presente tese, estruturada em cinco artigos científicos, explorou diferentes estratégias de modificação do $NaNbO_3$, incluindo o controle de morfologia, a dopagem com íons metálicos e a construção de uma heteroestrutura. Essas abordagens visaram aprimorar o desempenho fotocatalítico do material para ser aplicado no tratamento de efluentes. Adicionalmente, investigou-se a eficácia da perovskita no combate a patógenos clinicamente relevantes. É importante destacar que o $NaNbO_3$, semicondutor base da pesquisa, é uma perovskita livre de chumbo, o que reforça seu potencial para aplicações que visam enfrentar os desafios ambientais e de saúde pública.

1.1 Objetivos

1.1.1 Objetivo geral

Investigar as propriedades fotocatalítica e antibacteriana do $NaNbO_3$ e de suas modificações estruturais e composicionais, visando sua aplicação na remoção de poluentes emergentes em meio aquoso e no combate a bactérias patogênicas.

1.1.2 Objetivos específicos

Com base no objetivo geral, os objetivos específicos desta tese são:

a) Sintetizar $NaNbO_3$ 1D, otimizando o tempo de síntese para alcançar o menor valor reportado na literatura, com foco em aplicações fotocatalíticas;

b) Obter partículas nanométricas de $NaNbO_3$, visando aprimorar a eficiência fotocatalítica;

c) Desenvolver um fotocatalisador heteroestruturado à base de $NaNbO_3$/eumelanina, com atividade sob irradiação de luz visível;

d) Sintetizar $NaNbO_3$ 1D dopado com Al(III), avaliando o impacto da dopagem na propriedade fotocatalítica;

e) Sintetizar $NaNbO_3$ 1D dopado com Cu(II), avaliando o impacto da dopagem nas suas propriedades fotocatalítica e antibacteriana;

f) Sintetizar $NaNbO_3$ 1D dopado com Zn(II), investigando sua propriedade fotocatalítica e sua atividade frente a bactérias patogênicas;

g) Avaliar a eficiência fotocatalítica dos materiais obtidos na degradação do corante RhB como modelo de poluente emergente;

h) Investigar a atividade antibacteriana dos materiais sintetizados contra cepas de *S. aureus*, *E. coli* e *K. pneumoniae*;

i) Caracterizar as propriedades estruturais, morfológicas e ópticas dos materiais sintetizados, visando correlacionar tais características com suas atividades fotocatalítica e antibacteriana.

2 Revisão da literatura

2.1 Perovskita

Em 1839, o geólogo alemão Gustav Rouse descobriu um novo mineral nos Montes Urais, na Rússia, o composto titanato de cálcio ($CaTiO_3$). Ele nomeou essa nova estrutura cristalina de perovskita, em homenagem ao mineralogista russo Count Lev Alexevich von Perovski. Com o tempo, esta nomenclatura passou a designar uma ampla classe de materiais que compartilham organização estrutural similar à do mineral original; caracterizada pela estequiometria do tipo ABX_3, onde os sítios A e B são ocupados por cátions metálicos e o sítio X por um ânion não-metal, geralmente oxigênio ou halogênio [72,73].

A simetria perovskita é idealmente cúbica, com o cátion A, de maior tamanho, ocupando o sítio central, enquanto o cátion B, menor, é cercado por seis ânions X, formando uma estrutura hexacoordenada de geometria octaédrica (Figura 1). Entretanto, devido à flexibilidade da rede em acomodar uma variedade de elementos da tabela periódica, encontram-se variações ortorrômbicas, tetragonais, monoclínicas ou romboédricas, dependendo dos tamanhos relativos dos íons envolvidos e do fator de tolerância de Goldschmidt [72,74].

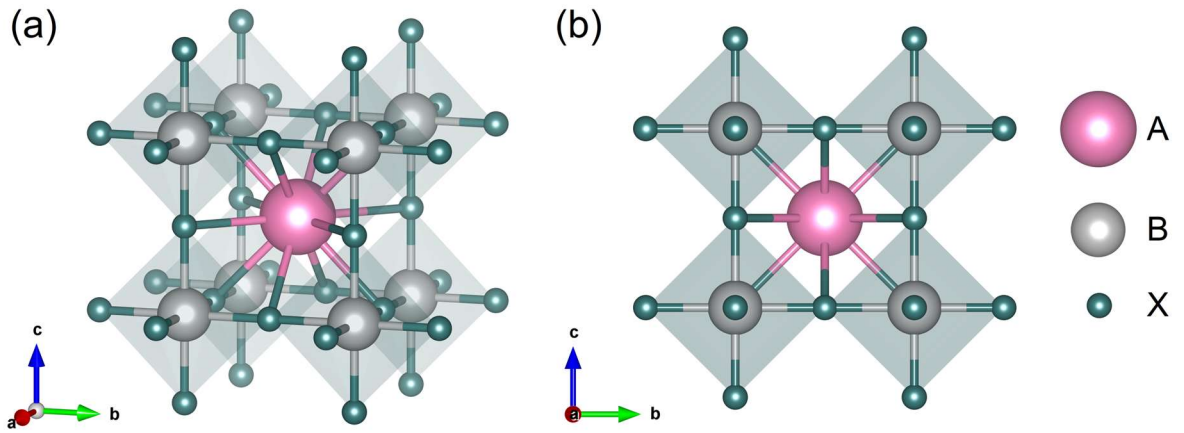

Figura 1 - Célula unitária de uma estrutura perovskita ideal, mostrando o cátion B coordenado a seis ânions X, formando os octaedros [BX_6], e o cátion A ocupando o sítio central do cubo. As setas indicam os eixos cristalográficos a, b e c. (a) Vista tridimensional e (b) Projeção bidimensional.
Fonte: Elaborado pela autora, 2025.

O fator de tolerância de Goldschmidt (Equação 1) é utilizado para prever a estabilidade e a simetria de compostos com estrutura do tipo perovskita ABX_3. Esse parâmetro foi proposto para descrever como os tamanhos relativos dos íons A, B e X influenciam a formação da estrutura cristalina, especialmente no que diz respeito à sua conformação cúbica ideal [72,74].

$$t = (r_A + r_X) / \sqrt{2}\,(r_B + r_X) \quad (1)$$

Onde t representa o fator de tolerância de Goldschmidt, r_A é o raio iônico do cátion A, r_B é o raio iônico do cátion B e r_X é o raio iônico do ânion. Quando o fator de tolerância se aproxima de 1, a estrutura cúbica ideal é favorecida. No entanto, valores de $t < 1$ (geralmente entre 0,75 e 1,0), indicam desajustes entre os tamanhos dos íons, o que leva a distorções na estrutura. Nessas condições, a perovskita pode exibir simetrias ortorrômbica, tetragonal, romboédrica ou monoclínica. Por outro lado, valores de $t > 1$ indicam que o cátion A é relativamente grande em comparação com B e X, o que pode dificultar a formação da estrutura perovskita. Nesses casos, há uma tendência à formação de fases alternativas, como hexagonais, por exemplo. De modo geral, considera-se que o intervalo ideal para a formação de perovskitas está compreendido entre aproximadamente 0,8 e 1,0. Valores fora dessa faixa crítica, especialmente abaixo de 0,8 ou acima de 1,0, tendem a comprometer a estabilidade da estrutura, favorecendo a formação de fases distintas ou altamente distorcidas [72,74].

Materiais com estrutura do tipo perovskita têm atraído grande interesse devido a diversas propriedades como ferroeletricidade, alta absorção óptica e condutividade elétrica e iônica. Essas características os tornam promissores para o avanço de tecnologias emergentes, incluindo sensores, supercapacitores, catalisadores, células solares, cerâmicas piezoelétricas, LEDs, lasers, entre outras [75-79]. Um exemplo notável são as células fotovoltaicas híbridas orgânico-inorgânicas baseadas em chumbo (Pb), que têm revolucionado o campo da energia solar ao atingir eficiências de conversão superiores a 25% [80]. Isto representa um marco significativo nas pesquisas por fontes de energia renovável, impulsionando ainda mais o interesse pelas perovskitas. Outro exemplo importante são as cerâmicas piezoelétricas, que dominam o mercado de materiais piezoelétricos, especialmente

o titanato de chumbo-zircônio (PZT) [81,82]. No entanto, a toxicidade do Pb e os riscos ambientais associados representam um enorme desafio.

Apesar do alto desempenho alcançado por dispositivos utilizando perovskitas contendo Pb, a toxicidade intrínseca desse elemento representa uma ameaça significativa à saúde humana e ao meio ambiente. Trata-se de um metal pesado altamente tóxico, com forte tendência à bioacumulação e elevada persistência ambiental [83-86]. Estudos demonstram que compostos solúveis formados a partir da degradação das perovskitas, como PbI_2, podem ser liberados sob condições de calor, umidade ou estresse mecânico, contaminando solos e águas subterrâneas [86]. Essa liberação não apenas compromete ecossistemas inteiros, mas também oferece riscos diretos ao organismo humano, incluindo neurotoxicidade, disfunções cardiovasculares, anemia, distúrbios reprodutivos e impactos no desenvolvimento infantil [84,86]. A gravidade desses efeitos é intensificada pela capacidade do Pb de imitar íons essenciais como Ca^{2+}, Fe^{2+} e Zn^{2+}, interferindo assim em funções fisiológicas normais e induzindo estresse oxidativo [86]. Este cenário tem motivado cada vez mais as pesquisas em busca de perovskitas livres de chumbo (*lead-free*), com o objetivo de garantir a segurança ambiental sem comprometer o desempenho dos dispositivos [87].

2.2 Niobato de sódio

Um dos primeiros trabalhos a mencionar o $NaNbO_3$ foi publicado pelo físico Eric Cross na década de 1940, em meio a suas pesquisas nos campos da piezoeletricidade e ferroeletricidade [88]. Desde então, o material passou a ser amplamente estudado no contexto das piezocerâmicas *lead-free*, como uma alternativa ao PZT, devido às suas notáveis propriedades ferroelétricas e piezoelétricas [89,90]. Com o avanço das investigações científicas, emergiu como uma perovskita promissora e atrativa para uma gama maior de aplicações, incluindo catalíticas, armazenamento e conversão de energia, além de usos biomédicos [56,91-96].

O $NaNbO_3$, do ponto de vista estrutural, é a perovskita que mais apresenta polimorfismo. Em 1974, Megaw [97] listou sete fases cristalinas em função da temperatura, conforme apresentado na Tabela 1.

Tabela 1 - Fases do $NaNbO_3$ em função da temperatura.

FASE	SIMETRIA	GRUPO ESPACIAL	TEMP. APROX. (K)
N	Romboédrica	R3c	< 250
P	Ortorrômbica	Pbcm	250 - 645
R	Ortorrômbica	Pbnm	645 - 710
S	Ortorrômbica	Pbnm	710 - 790
T1	Ortorrômbica	Ccmm	790 - 845
T2	Tetragonal	P4/mbm	845 - 925
U	Cúbica	Pm3m	> 925

Fonte: Adaptada da referência [97].

Yuzyuk et al. [98] também investigaram a estrutura cristalina do $NaNbO_3$ e seus experimentos sugeriram que a fase P consiste em três simetrias: monoclínica (Pm) entre 250 e 410 K, uma fase incomensurável (INC) entre 410 e 460 K e ortorrômbica (Po) entre 460 e 633 K. Em relação à fase INC, os autores atribuíram ao efeito Invar, associado às rotações do octaedro NbO_6 na direção ao longo do eixo b. Além disso, estudos mostram diferenças nas temperaturas de transições de fase para cristais com tamanhos micrométricos, submicrométricos e nanométricos, indicando uma dependência conforme o tamanho dos grãos [99,100]. Devido à complexidade estrutural do $NaNbO_3$, diferentes simetrias ortorrômbicas podem coexistir no material. As mais comumente reportadas são os grupos espaciais P21ma e Pbma (Figura 2) [101-103]. A formação preferencial de uma dessas simetrias pode ser influenciada pelas condições de síntese, já que ambas são termodinamicamente estáveis e apresentam características similares. A fase polar P21ma é favorecida pela cristalização em temperaturas relativamente baixas (600 °C), mas se transforma em temperaturas mais altas (abaixo de 950 °C) na estrutura centrossimétrica estável Pbma [101]. Embora o $NaNbO_3$ seja amplamente estudado, possui uma estrutura cristalina bastante complexa e ainda existem controvérsias em relação ao seu diagrama de fases [104].

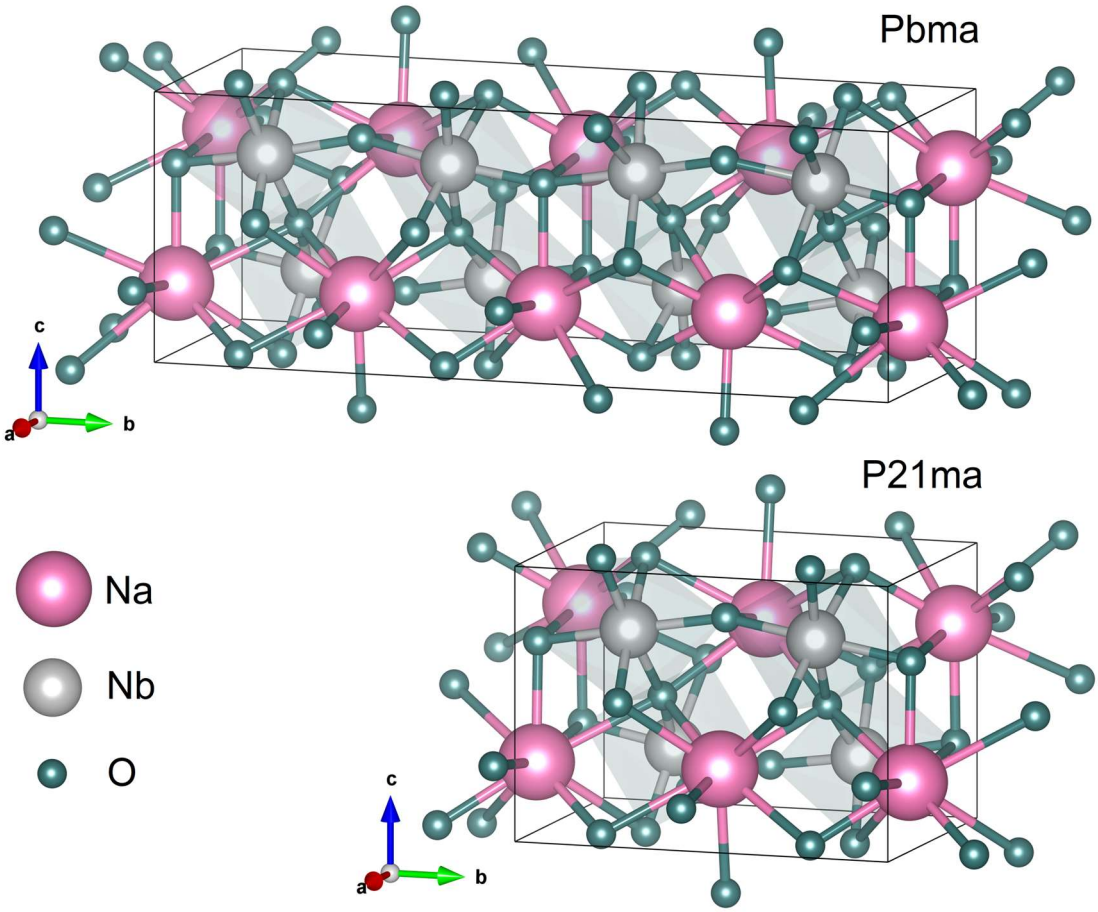

Figura 2 - Representações estruturais das fases ortorrômbicas assumidas pelo $NaNbO_3$ com simetrias espaciais Pbma (a = 5,5679 Å, b = 15,5156 Å e c = 5,5029 Å) e P21ma (a = 5,5690 Å, b = 7,7900 Å e c = 5,5180 Å). As setas indicam os eixos cristalográficos a, b e c.
Fonte: Elaborado pela autora, 2025.

Além da complexidade estrutural, a morfologia e o crescimento de grãos do $NaNbO_3$ são fortemente influenciados pelas condições de síntese. Em rotas hidrotérmicas, inicialmente forma-se uma fase metaestável de nanofios de hexaniobato de sódio ($Na_2Nb_2O_6 \cdot H_2O$) e à medida que a síntese avança, ocorre a nucleação de cristais em forma de cubos sobre estes nanofios, por serem termodinamicamente mais estáveis, resultando na transformação morfológica. A obtenção do $NaNbO_3$ na forma de fios ou hastes só é possível a partir da calcinação da fase $Na_2Nb_2O_6 \cdot H_2O$. Isso se deve ao fato de que, para preservar a morfologia 1D a nucleação precisa ocorrer em um ambiente confinado, como durante a calcinação, onde há difusão restrita. Caso a nucleação aconteça em solução aquosa (meio não

confinado), o comportamento natural favorece a formação de grãos com morfologia cúbica [22,105-111]. Esse processo está ilustrado esquematicamente na Figura 3.

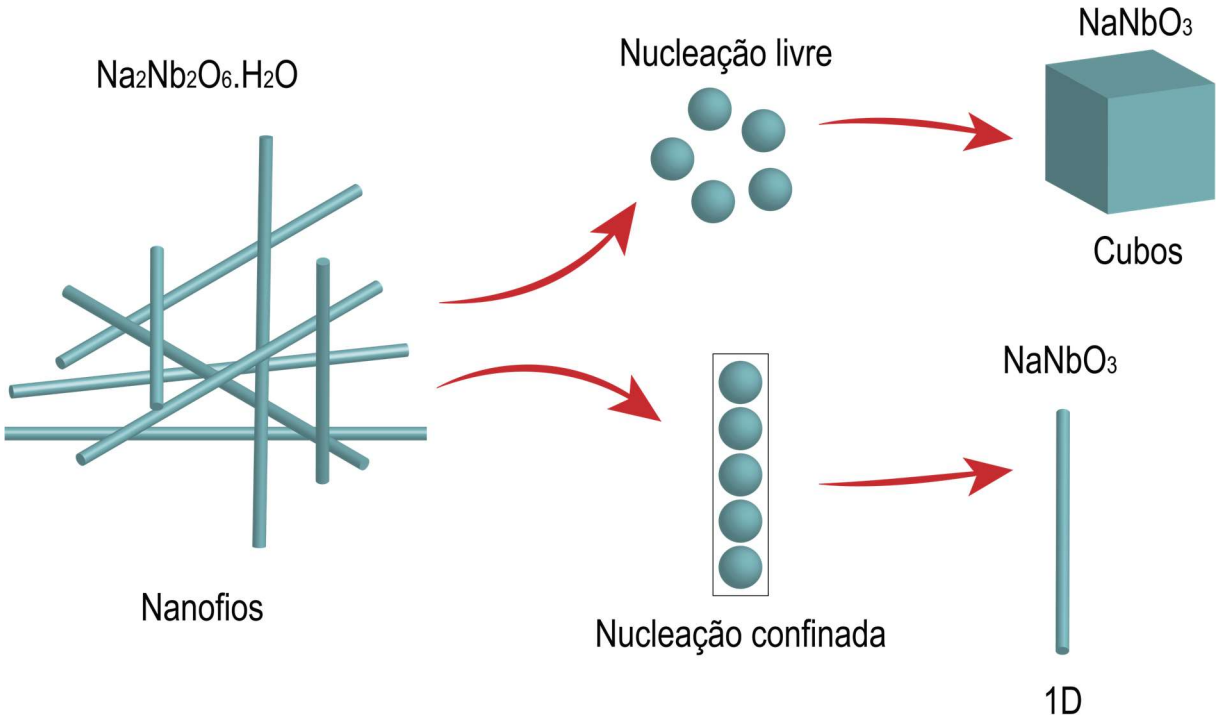

Figura 3 - Esquema representativo do mecanismo de formação do $NaNbO_3$ em sínteses hidrotérmicas, por dois caminhos distintos: nucleação livre, que leva à formação de partículas cúbicas, e nucleação confinada, que favorece o crescimento unidimensional (1D).
Fonte: Elaborado pela autora, 2025.

2.3 Síntese hidrotérmica assistida por micro-ondas

A síntese hidrotérmica assistida por micro-ondas é um método que combina a abordagem hidrotérmica tradicional com a eficiência do aquecimento proporcionado pelas micro-ondas, ou seja, radiação eletromagnética na faixa de frequência entre 0,3 e 300 GHz. O uso de micro-ondas em processos químicos começou a ser investigado na década de 1980, com trabalhos pioneiros de Gedye [112] e Giguere [113], que demonstraram os benefícios desta radiação para acelerar reações orgânicas. No entanto, foi a partir da década de 1990 que sua associação a sistemas hidrotérmicos passou a ser explorada na síntese de materiais inorgânicos.

Komarneni et al. [114] relataram não só a obtenção de zeólitas e outros óxidos metálicos, como destacaram os mecanismos que tornam este método vantajoso, como o aquecimento volumétrico e a rápida transferência de energia.

O aquecimento por micro-ondas baseia-se no mecanismo dielétrico, o qual ocorre devido à interação de ondas eletromagnéticas na faixa de micro-ondas (geralmente 2,45 GHz nos equipamentos comerciais) com materiais dielétricos. Quando expostas a um campo eletromagnético alternado, as moléculas polares, tentam alinhar seus dipolos com a direção do campo, gerando calor por fricção intermolecular e relaxamento dipolar [115]. A eficiência desse mecanismo depende da frequência das micro-ondas e das propriedades dielétricas do material, como a constante dielétrica (ϵ') e o fator de perda dielétrica (ϵ''). A tangente de perda ($\tan \delta = \epsilon''/ \epsilon'$) é uma métrica que permite avaliar a eficiência do aquecimento: materiais com alta tangente de perda, para uma dada frequência, tendem a absorver mais energia e aquecer de forma mais eficaz [116,117]. A distribuição de energia ocorre de forma volumétrica, o que possibilita que toda a reação seja aquecida de maneira uniforme, evitando os gradientes térmicos típicos dos métodos convencionais, favorecendo a homogeneidade estrutural [117,118]. Como consequência, o aquecimento por micro-ondas é mais rápido, eficiente e uniforme. Além disso, o calor induzido promove o aumento da pressão interna do reator, criando condições específicas para reações químicas que dependem de tais parâmetros.

A Figura 4 ilustra o sistema utilizado para a síntese das amostras reportadas nos artigos que compõem esta tese. O arranjo foi desenvolvido a partir de um forno de micro-ondas doméstico, incorporando um conjunto de componentes adicionais que permitem o monitoramento e controle das condições reacionais. Conta com um controlador programável, um termopar para medição precisa da temperatura em tempo real e um manômetro acoplado à célula reacional, que permite o acompanhamento da pressão interna durante as sínteses. Adicionalmente, uma válvula de alívio foi instalada na célula para garantir a segurança do processo. O recipiente onde ocorre a reação é constituído de politetrafluoroetileno (PTFE), garantindo compatibilidade química e resistência às condições operacionais. Todos os dispositivos utilizados foram devidamente aferidos, assegurando a confiabilidade dos dados obtidos. Ainda que esse sistema tenha se mostrado eficaz e seguro para os objetivos desta pesquisa, vale ressaltar que existem equipamentos comerciais

específicos para este tipo de síntese com certificações específicas para uso laboratorial.

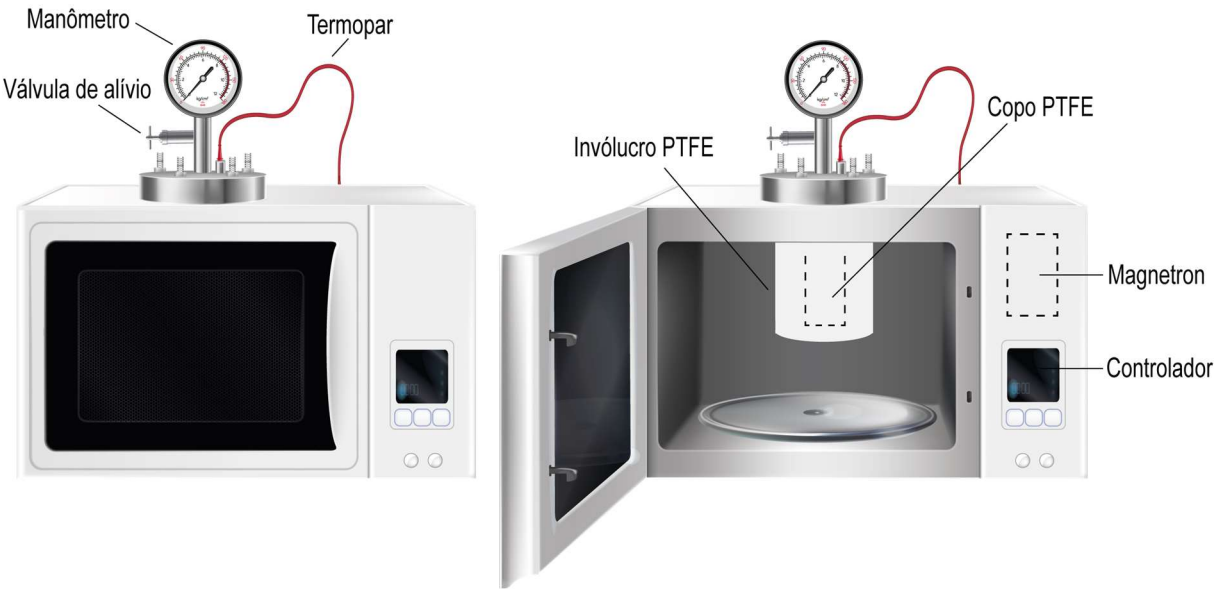

Figura 4 - Esquema ilustrativo de um sistema utilizado para realizar sínteses assistidas por micro-ondas, adaptado a partir de um forno de micro-ondas doméstico.
Fonte: Elaborado pela autora, 2025.

Esta técnica tem se mostrado uma abordagem altamente promissora para a síntese de materiais. Ao associar as micro-ondas como fonte de energia à síntese hidrotérmica, muitos benefícios podem ser alcançados como, por exemplo, economia de custos devido a uma cinética mais favorável, reações com rendimentos mais altos e em menor tempo, além de nucleação e cristalização mais homogêneas [119-121]. A Tabela 2 apresenta estudos que obtiveram o $NaNbO_3$ 1D pelo método hidrotérmico convencional e associado às micro-ondas, permitindo observar as diferenças nos tempos de obtenção do material.

Tabela 2 - Estudos que obtiveram $NaNbO_3$ 1D.

SÍNTESE Temperatura/Tempo	TRATAMENTO TÉRMICO Temperatura/Tempo	REFERÊNCIA
HID-C 180 ºC/2 h	300 ºC/12 h	[22]
HID-C 150 ºC/5 h	500 ºC/4 h	[26]
HID-AM 160 ºC/40 min	550 ºC/4 h	[102]
HID-C 120 ºC/3 h	400 ºC/NE*	[107]
HID-C 200º C/24 h	550 ºC/4 h	[108]
HID-C 150 ºC/10 h	NE/NE*	[109]
HID-AM 180 ºC/1 h	550 ºC/4 h	[110]
HID-C 183 ºC/2 h	600 ºC/6 h	[122]
HID-C 150 ºC/4 h	400 ºC/12 h	[123,124]
HID-C 140 ºC/6 h	700 ºC/3 h	[125]
HID-C 200 ºC/8 h	400 ºC/3 h	[126]
HID-C 160 ºC/6 h	NE/NE*	[127]
HID-C 160 ºC/6 h	500 ºC/2 h	[128]
HID-AM 180 ºC/30 min	550 ºC/4 h	[129]
HID-C 160 ºC/6 h	450 ºC/1 h	[130]
HID-C 150 ºC/5 h	500 ºC/4 h	[131]
HID-C 200 ºC/4 h	500 ºC/3 h	[132]
HID-C 150 ºC/6 h	600 ºC/6 h	[133]
HID-C 180 ºC/2 h	NE/NE*	[134]
HID-C 150 ºC/4 h	500 ºC/8 h	[135]
HID-C 180 ºC/100 min	550 ºC/4 h	[136]

Legenda: HID-C (Hidrotérmica convencional) e HID-AM (Hidrotérmica assistida por micro-ondas).

*NE (não especificado).

Fonte: Elaborado pela autora, 2025.

2.4 Fotocatálise heterogênea

2.4.1 Mecanismo e aplicações

Fotocatálise heterogênea é o processo de acelerar reações químicas através da ação de um catalisador sólido usando a luz como fonte de energia. Sua gênese data de 1972, devido ao trabalho pioneiro de Fujishima e Honda [137]. Os pesquisadores reportaram a oxidação da água, em uma célula eletroquímica, incidindo luz sobre um eletrodo de TiO_2. Neste mecanismo fotocatalítico (Figura 5), o semicondutor ao absorver fótons (hν) com energia igual ou superior ao seu *band gap*, tem seus elétrons excitados da BV para a BC, gerando pares e^-/h^+. Estas cargas fotogeradas podem, então, participar de reações de oxidação e redução na superfície do fotocatalisador [11,12].

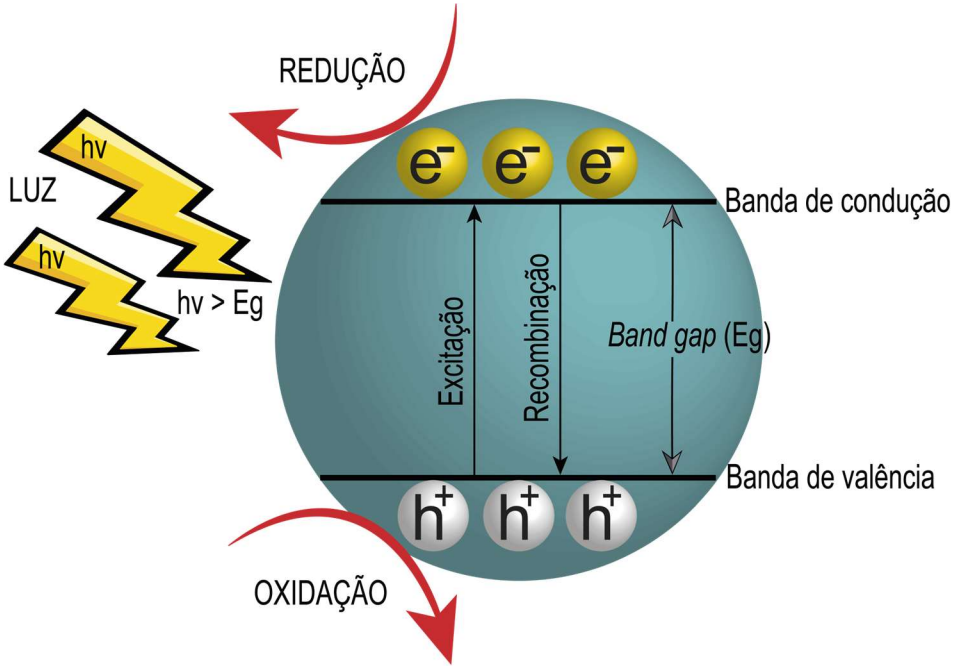

Figura 5 - Esquema simplificado mostrando o mecanismo básico da fotocatálise heterogênea, a partir da fotoativação de um semicondutor.
Fonte: Elaborado pela autora, 2025.

A tecnologia fotocatalítica tem se alavancado como uma abordagem promissora para enfrentar os desafios energéticos e ambientais, com avanços

significativos nos últimos anos. Entre suas aplicações, podemos destacar a produção H_2 para ser utilizado como combustível limpo [138]. O processo é eficiente e sustentável, já que utiliza a energia abundante do sol e a água como insumo. Além disso, materiais fotocatalíticos podem ser aplicados em superfícies para promover autolimpeza, inativar microrganismos patogênicos e reduzir gases nocivos no ar, por exemplo [139-141]. Outra aplicação notável é o tratamento de águas, onde fotocatalisadores são usados para decompor poluentes orgânicos, como corantes orgânicos, herbicidas e fármacos [9,142].

A fotocatálise aplicada à degradação de poluentes orgânicos, utilizando semicondutores como fotocatalisadores, ocorre por meio de dois mecanismos principais: oxidação direta e indireta [143]. No mecanismo de oxidação direta, o poluente é primeiramente adsorvido na superfície do fotocatalisador, onde é oxidado diretamente pelas h^+ fotogeradas na BV do semicondutor. No mecanismo de oxidação indireta, os pares e^-/h^+ fotogerados nas bandas do semicondutor reagem com o meio formando radicais livres, altamente reativos, que são capazes de oxidar/reduzir os compostos orgânicos. A fotocatálise indireta apresenta uma série de reações envolvidas, as quais são apresentadas a seguir:

$$\text{Semicondutor}_{(s)} + h\nu \rightarrow \text{Semicondutor}_{(s)} + e^-_{(BC)} + h^+_{(BV)} \quad (2)$$

$$h^+ + H_2O \rightarrow OH^\bullet + H^+ \text{ e } h^+ + OH^- \rightarrow OH^\bullet \quad (3)$$

$$e^- + O_2 \rightarrow O_2^{\bullet-} \quad (4)$$

$$O_2^{\bullet-} + H^+ \rightarrow HO_2^\bullet \quad (5)$$

$$HO_2^\bullet + HO_2^\bullet \rightarrow H_2O_2 + O_2 \quad (6)$$

$$O_2^{\bullet-} + HO_2^\bullet \rightarrow HO_2^- + O_2 \quad (7)$$

$$HO_2^- + H^+ \rightarrow H_2O_2 \quad (8)$$

$$H_2O_2 + e^- \rightarrow OH^- + OH^\bullet \quad (9)$$

$H_2O_2 + O_2^{\bullet-} \rightarrow OH^- + OH^\bullet + O_2$ (10)

Poluente orgânico + $OH^\bullet \rightarrow$ Produtos intermediários (11)

Poluente orgânico + $OH^\bullet \rightarrow CO_2 + H_2O$ (12)

Quando a luz incide sobre o semicondutor fotocatalisador, ele absorve os hν e promove os e^- da BV para a BC, formando pares e^-/h^+ (Equação 2). As h^+ na BV podem reagir com a água (H_2O) ou íons hidróxido (OH^-), gerando radicais hidroxila ($OH^\bullet$) (Equação 3). Os e^- na BC podem reagir com o oxigênio (O_2), formando ânions superóxidos ($O_2^{\bullet-}$) (Equação 4). Os $O_2^{\bullet-}$ desencadeiam uma série de reações, que levam à formação e quebra de peróxido de hidrogênio (H_2O_2) (Equações 5 a 10). Os $OH^\bullet$ são altamente reativos e atacam o poluente orgânico, quebrando suas ligações e promovendo a formação de produtos intermediários, na maioria das vezes, com toxicidade inferior (Equação 11). Em casos ideais, pode levar à mineralização completa do poluente orgânico, transformando-o em CO_2 e água (Equação 12).

2.4.2 Estratégias para melhorar a eficiência dos fotocatalisadores

A dopagem tem se mostrado um método eficiente para aumentar a atividade dos fotocatalisadores [16-18]. Trata-se de uma técnica que consiste em introduzir íons dopantes na estrutura cristalina do semicondutor, seja em sítios intersticiais ou substitucionais (Figura 6). Esse processo induz desordem na rede hospedeira que, consequentemente, altera as propriedades eletrônicas do material. Diversos benefícios podem ser obtidos, como a redução do *band gap*, o que diminui a energia necessária para gerar pares e^-/h^+ [16-18,144]. Além disso, a dopagem pode aumentar a capacidade de absorção de luz e modificar a interação das substâncias de interesse com a superfície do fotocatalisador [42,144]. Outro efeito relevante é o retardamento da recombinação das cargas fotogeradas, resultado da formação de níveis intermediários de energia. Isso ocorre porque os elétrons transitam por esses níveis antes de retornar ao estado fundamental do semicondutor, prolongando a vida útil dos pares e^-/h^+ [41,43,144].

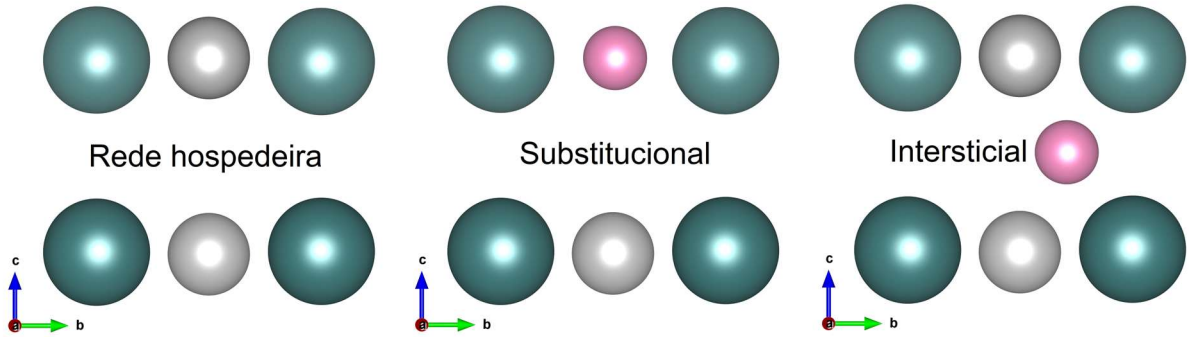

Figura 6 - Representação esquemática bidimensional dos tipos de dopagem em semicondutores: rede hospedeira (sem dopantes), dopagem substitucional, em que um átomo da rede é substituído por um dopante (esfera rosa), e dopagem intersticial, na qual o dopante ocupa uma posição entre os átomos da rede cristalina. As setas indicam os eixos cristalográficos a, b e c.
Fonte: Elaborado pela autora, 2025.

Na dopagem, o deslocamento do nível de Fermi pode alterar significativamente a condutividade do material e a sua resposta à radiação luminosa. O nível de Fermi é um nível de energia que controla a ocupação de estados de energia por partículas de férmions, como elétrons e lacunas. Dopantes do tipo n adicionam elétrons ao sistema, elevando o nível de Fermi em direção à BC, enquanto dopantes do tipo p criam lacunas, deslocando o nível de Fermi para mais próximo da BV [145]. Um fenômeno recorrente na dopagem de semicondutores, muito comum em semicondutores degenerados, é o efeito Burstein-Moss, no qual o aumento na densidade de portadores de carga empurra o nível de Fermi para o interior da BC (Figura 7) [146,147]. Isso eleva a energia necessária para que um fóton induza a transição eletrônica, ou seja, ocorre um aumento aparente do *band gap* (azulamento da absorção óptica) [40,148]. Embora o nível de Fermi seja deslocado, o aumento aparente do *band gap* é observado apenas em medidas ópticas, não em medidas puramente eletrônicas. Ademais, a dopagem pode introduzir níveis eletrônicos que atuam como centros de recombinação para os pares e^-/h^+, reduzindo a vida útil das cargas fotogeradas [17]. Assim, a incorporação de dopantes inadequados ou em excesso pode ter efeitos negativos para fins fotocatalíticos.

Além da dopagem, o desenvolvimento de fotocatalisadores heteroestruturados também tem se destacado como uma estratégia eficaz para fins fotocatalíticos [19,20,149]. Nesse tipo de abordagem, dois ou mais materiais são combinados de forma a atuarem sinergicamente, formando uma única estrutura

funcional. A interface gerada entre os componentes permite controlar a mobilidade dos portadores de carga, favorecendo sua separação e reduzindo a recombinação. Como resultado, pode-se alcançar um desempenho fotocatalítico superior em comparação com os materiais isolados. Ademais, a arquitetura das heteroestruturas possibilita a modulação de outras propriedades importantes, como o intervalo de absorção da radiação e a adsorção seletiva de moléculas na superfície do fotocatalisador [149].

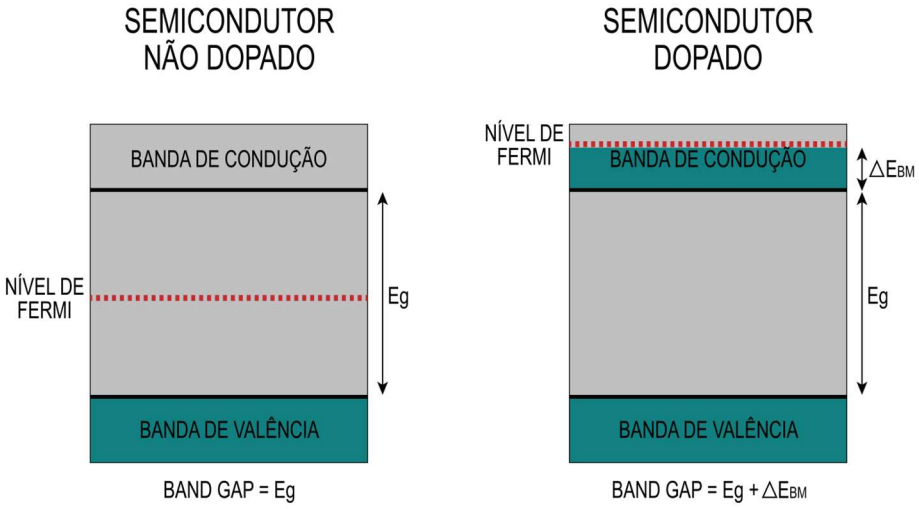

Figura 7 - Representação esquemática do efeito Burstein-Moss, resultando em um alargamento aparente do *band gap*.
Fonte: Elaborado pela autora, 2025.

As heteroestruturas formadas por semicondutores podem ser classificadas em três tipos, conforme ilustrado na Figura 8. No sistema do tipo I, a borda da BC do semicondutor 1 tem um potencial mais elevado em relação ao do semicondutor 2, enquanto a borda da sua BV possui um potencial inferior ao da BV do semicondutor 2. Como consequência, os e^- e as h^+ tendem a se acumular nos níveis da BC e BV do semicondutor com menor *band gap*, ou seja, no semicondutor 2. Essa configuração não promove uma separação eficiente das cargas fotogeradas, tornando-se inadequada para aplicações fotocatalíticas [149,150]. Por outro lado, na heteroestrutura do tipo II, a migração das cargas fotogeradas ocorre em direções opostas, de modo que os e^- são acumulados em um semicondutor, enquanto as h^+

acumulam-se no outro. Essa separação espacial dos pares e^-/h^+ resulta da relação entre as bandas dos semicondutores, cujas posições de borda favorecem essa dinâmica. Como efeito, a taxa de recombinação é reduzida, tornando essa configuração benéfica para fins fotocatalíticos [149,150]. Na heteroestrutura do tipo III, a migração dos portadores de carga ocorre de maneira semelhante à do tipo II. No entanto, não há sobreposição dos *gaps*, por isso é também conhecida como heterojunção "*broken gap type*". Além disso, o desalinhamento acentuado das bandas dificulta significativamente a mobilidade eletrônica através da interface. Como resultado, esse tipo de heterojunção também é inadequada para aplicações fotocatalíticas [149,150].

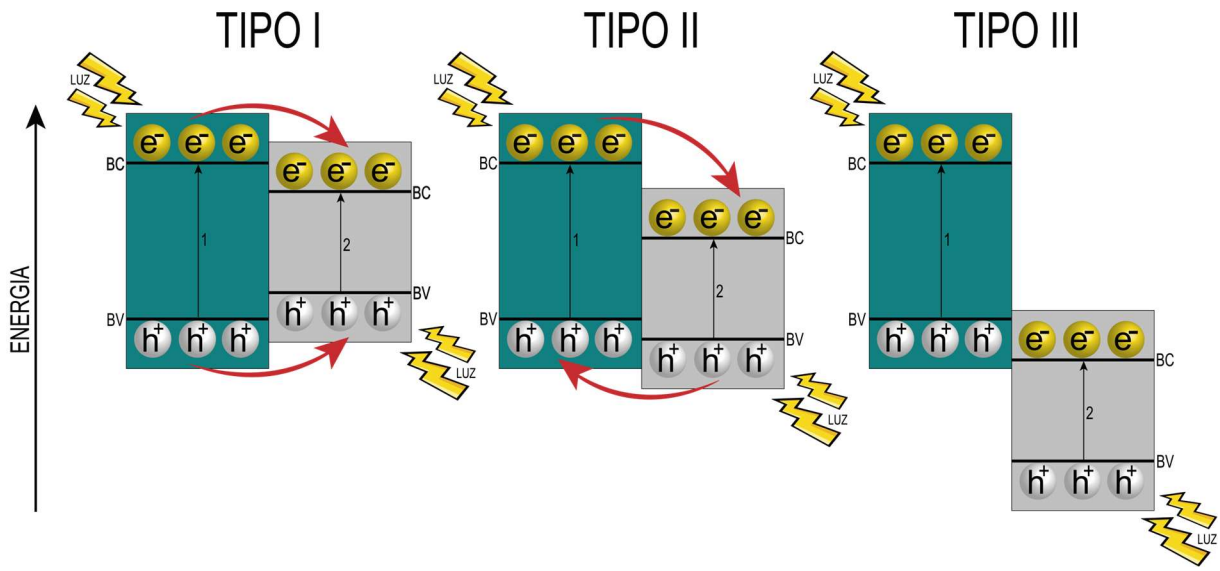

Figura 8 - Ilustração esquemática dos tipos de heteroestruturas formadas entre dois semicondutores, conforme o alinhamento das bandas de energia: Tipo I, Tipo II e Tipo III.
Fonte: Elaborado pela autora, 2025.

Existem ainda outros tipos de heteroestruturas, tais como a junção p-n, esquema-Z direto e a junção Schottky (Figura 9). A heteroestrutura p-n é formada pela junção de um semicondutor do tipo p com outro do tipo n. Quando esses dois materiais entram em contato, ocorre uma migração dos portadores de carga entre eles, até que se atinja o equilíbrio dos níveis de Fermi. Esse processo de difusão eletrônica gera um campo elétrico interno na interface p-n. Sob a influência desse

campo, os pares e^-/h^+ migram de um semicondutor para o outro. Esse dinâmica resulta na separação espacial das cargas e no aumento do tempo de vida das mesmas [149]. A construção da heteroestrutura esquema-Z direto foi inspirada no processo natural de fotossíntese, no qual o movimento das cargas ocorre em forma de ziguezague, formando a letra "Z". Esse sistema consegue reter os e^- na BC do semicondutor 1 e as h^+ na BV do semicondutor 2, resultando na efetiva separação das cargas fotogeradas [149-151]. A junção Schottky, nomeada em homenagem ao físico Walter H. Schottky, é formada por uma combinação metal-semicondutor (tipo n ou p). Nesse sistema, os e^- fluem do semicondutor para o metal, fazendo com que este apresente excesso de carga negativa, enquanto o semicondutor adquire excesso de carga positiva. Assim como nas heteroestruturas do tipo p-n, um campo elétrico é gerado na interface dos materiais, denominado barreira Schottky, que contribui para a separação efetiva dos portadores de carga [149,152].

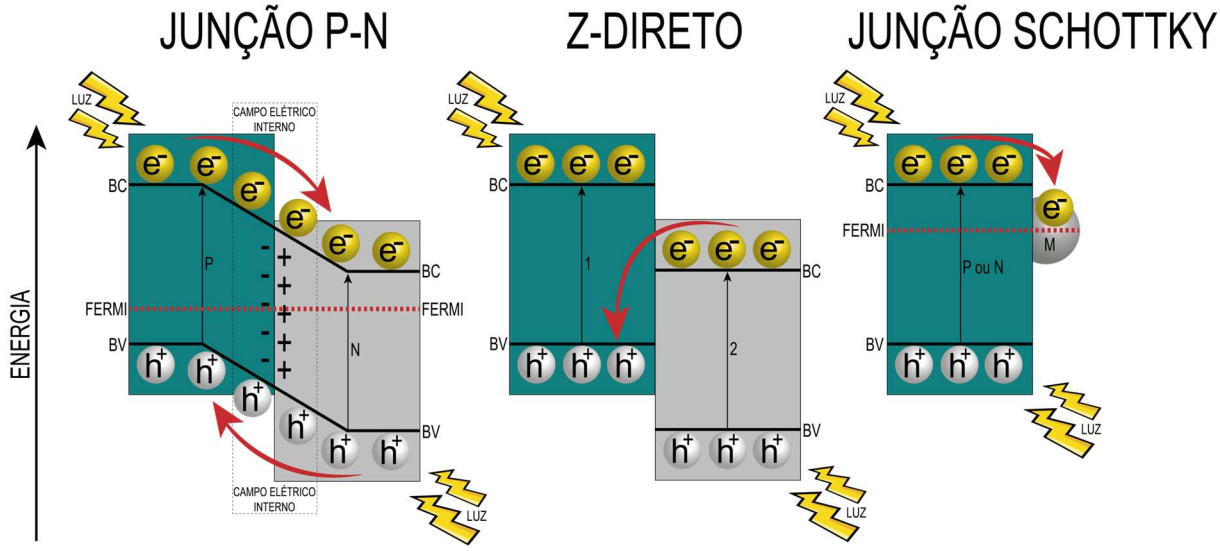

Figura 9 - Ilustração esquemática dos tipos de heteroestruturas:
Junção p-n, Esquema-Z direto e Junção Schottky.
Fonte: Elaborado pela autora, 2025.

2.5 Niobato de sódio como fotocatalisador

2.5.1 Efeitos de morfologia

A fim de comparar a atividade fotocatalítica do $NaNbO_3$ 1D com a sua forma natural (partículas cúbicas), Shi et al. [108] conduziram um estudo para gerar H_2 e os nanofios apresentaram desempenho significativamente superior. Esse resultado foi atribuído a sua maior cristalinidade, maior razão superfície/volume e anisotropia estrutural, que favorecem o transporte e separação de cargas, além de disponibilizar mais sítios ativos para as reações.

Liu et al. [22] também avaliaram a influência da morfologia na resposta fotocatalítica, comparando nanofios e cubos de $NaNbO_3$, para a geração de H_2. Os nanofios apresentaram a maior taxa de evolução do gás, enquanto os cubos exibiram desempenho muito inferior. Os autores explicaram essa diferença com base na maior cristalinidade, menor concentração de defeitos e na estrutura 1D, que favorece a separação eficiente dos pares e^-/h^+, melhora a absorção de luz e aumenta o número de sítios ativos acessíveis.

De forma semelhante, Yan et al. [26] compararam o desempenho de nanofios e cubos de $NaNbO_3$, mas com base na degradação dos corantes orgânicos RhB e vermelho X-GRL (CRX). Os nanofios exibiram resposta claramente superior, com constantes cinéticas de degradação aproximadamente 1,96 vezes maiores para RhB e 20 vezes maiores para CRX. Essa maior atividade foi atribuída à maior área superficial específica, que proporciona mais sítios ativos disponíveis para as reações.

2.5.2 Efeitos de dopagem

Visando estender a atividade fotocatalítica do $NaNbO_3$ para a região do visível, Shi et al. [39] doparam a perovskita com N. O experimento realizado consistiu na degradação do 2-propanol, observada pela taxa de geração de acetona. As amostras dopadas exibiram melhor desempenho, superando o $NaNbO_3$ puro, que mostrou atividade desprezível sob luz visível. Segundo os autores, isso se deve a substituição de alguns átomos de O por N, o que contribuiu para a formação de estados N 2p acima da BV, permitindo a absorção de luz visível. Contudo, observaram que o

aumento excessivo da dopagem levou à diminuição da atividade, possivelmente devido a geração de centros de recombinação dos pares e^-/h^+.

Singh et al. [40] também com o objetivo de obter resposta fotocatalítica sob luz visível, exploraram a dopagem do $NaNbO_3$ com Ca e a formação de uma heterojunção com nitreto de carbono grafítico (g-C_3N_4). O estudo demonstrou atividade sob luz visível, evidenciada pela degradação do corante azul de metileno (AM) e pela geração de H_2 sob luz solar natural. Esse desempenho superior foi atribuído a criação de vacâncias de O e a interação sinérgica entre o $NaNbO_3$ dopado e o g-C_3N_4 que favoreceram a separação eficiente das cargas fotogeradas e reduziram sua recombinação. Além disso, os autores observaram que, em concentrações mais elevadas de dopagem, foi observado um aumento do *band gap*, atribuído ao efeito Burstein-Moss.

No estudo reportado por Wu et al. [42], a influência da dopagem do $NaNbO_3$ com V foi investigada. O $NaNbO_3$ dopado apresentou maior atividade fotocatalítica para degradar os antibióticos Tetraciclina, Ciprofloxacino e Enrofloxacino. A dopagem não apenas reduziu o *band gap*, como também favoreceu a separação das cargas fotogeradas e diminuiu sua taxa de recombinação, resultando em maior resposta fotocatalítica. Adicionalmente, foi observado que os materiais dopados apresentaram uma taxa de adsorção superior para as moléculas de Ciprofloxacino, o que foi atribuído a maior área superficial específica e presença de mais sítios ativos na superfície, intensificando a interação com esse poluente.

No trabalho realizado por Jana et al. [41], a dopagem do $NaNbO_3$ com K e V foi explorada com o objetivo de aprimorar sua atividade fotocatalítica na degradação do corante AM. Os resultados mostraram que a dopagem conjunta (K+V) exibiu maior eficiência de degradação, superando os sistemas dopados individualmente. Esse comportamento foi associado a maior distorção de rede induzida pelos dopantes, redução do *band gap* e geração de vacâncias de O que atuaram como centros de aprisionamento, favorecendo a separação dos pares e^-/h^+.

Diferente de outros estudos com $NaNbO_3$ que obtiveram partículas 1D e cúbicas, Praxedes et al. [153] reportaram uma abordagem inovadora ao empregar o método de spray-pirólise para obter esferas ocas de $NaNbO_3$ dopado com K. A dopagem com K promoveu distorções estruturais e polarização da rede, resultando na redução do *band gap*. Essa modificação estrutural favoreceu a absorção de fótons

e a transferência de carga, o que impulsionou a atividade fotocatalítica na degradação do corante Basic blue 41, sob irradiação UV. Além disso, o formato oco das partículas desempenhou um papel importante na adsorção do poluente.

Fazendo uso também da estratégia da dopagem para melhorar a atividade fotocatalítica do $NaNbO_3$, Farooq et al. [43] investigaram o efeito da inserção de Ta no sítio do Nb. Embora a dopagem tenha aumentado o *band gap,* devido a substituição de Nb^{5+} por Ta^{5+}, observou-se uma melhoria na performance fotocatalítica, observada pela degradação do corante AM e geração de H_2. Os autores atribuíram esse desempenho ao aumento da área superficial, modificação favorável do potencial da BC e redução da recombinação das cargas fotogeradas.

2.5.3 Construção de heteroestruturas

Lv et al. [44] reportaram a construção de um compósito $In_2O_3/NaNbO_3$ com desempenho superior na geração de H_2 sob luz visível, alcançando o dobro da taxa obtida com o $NaNbO_3$ puro e sete vezes mais que o In_2O_3 isolado. Esse resultado foi atribuído a eficiente separação e transporte dos portadores de carga, favorecidos pelo alinhamento de bandas, comportamento típico de uma heteroestrutura do tipo II, embora o termo não tenha sido mencionado diretamente. De forma semelhante, Feng et al. [50] sintetizaram compósitos $Ag_2SO_3/NaNbO_3$ com alta eficiência na degradação dos corantes RhB e alaranjado de metila (LM) sob luz visível, superando os semicondutores individuais. Essa melhora foi associada à formação de uma junção eficaz que promoveu a separação dos pares e^-/h^+, também compatível com uma heteroestrutura do tipo II. Rajan et al. [55] desenvolveram um compósito $NaNbO_3/CuBi_2O_4$ com desempenho expressivo em condições piezo-fotocatalíticas para degradação do corante RhB. A eficiência foi atribuída a ação combinada da piezoeletricidade do $NaNbO_3$, forte absorção na região visível do $CuBi_2O_4$ e a presença de um campo elétrico gerado, que direciona os portadores de carga e cria múltiplos sítios reativos. Embora o mecanismo envolva fenômenos adicionais, os autores descrevem um comportamento compatível com uma heteroestrutura do tipo II, ainda que o termo não tenha sido mencionado de forma direta no estudo.

Alguns estudos mencionam diretamente a formação de heteroestruturas do tipo II, como o estudo de Qiao et al. [52]. Os pesquisadores desenvolveram

compósitos $NaNbO_3/Bi_2WO_6$ com desempenho superior na degradação do corante RhB sob luz visível, atingindo uma taxa 40 vezes maior que a do $NaNbO_3$ e 2,5 vezes maior que a do Bi_2WO_6, quando testados individualmente. Esse resultado foi atribuído a formação de uma heterojunção estável e com forte interação entre os semicondutores, favorecendo significativamente a separação de cargas fotoexcitadas. Zhang et al. [53] reportaram compósitos de $NaNbO_3/g\text{-}C_3N_4$ com alta atividade fotocatalítica para a degradação do antibiótico Ofloxacino sob luz solar simulada, alcançando uma constante de degradação 29,6 vezes maior que a do $NaNbO_3$ puro. A elevada eficiência foi atribuída ao forte acoplamento interfacial, que promoveu a separação eficiente dos pares e^-/h^+. Na mesma linha, Kumar et al. [46] sintetizaram uma heteroestrutura $NaNbO_3$/CdS, a qual exibiu desempenho significativamente superior na degradação do corante AM sob luz visível. Os autores associaram esse efeito a combinação entre maior área superficial, ampliação da absorção na região visível e a separação direcionada dos portadores de carga promovida pela estrutura de bandas, do tipo II, entre o núcleo de $NaNbO_3$ e a casca de CdS.

Pesquisas também exploraram a formação de heteroestruturas com junção p–n, como o de Xu et al. [45], que sintetizaram compósitos $NaNbO_3$/ZnO e observaram desempenho superior na degradação do corante AM sob luz UV. Esse resultado foi atribuído a formação da junção entre o $NaNbO_3$ e o ZnO, a qual favoreceu a separação dos pares e^-/h^+ e restringiu sua recombinação. De forma similar, Sun et al. [48] desenvolveram heteroestruturas BiOI/$NaNbO_3$ com elevada atividade para degradar AM sob luz visível. Essa atividade foi atribuída ao aumento da absorção de luz visível proporcionado pelo BiOI e a um campo elétrico interno gerado na interface dos semicondutores, favorecendo a separação eficiente dos pares e^-/h^+. Zhang et al. [49] relataram uma junção entre Ag_2O (tipo p) e $NaNbO_3$ (tipo n), obtendo excelente resposta na degradação do corante RhB sob luz visível, atribuído tanto a separação de cargas quanto à redução do *band gap*. Fan et al. [47] desenvolveram um compósito $Cu_2O/NaNbO_3$ com alta atividade fotocatalítica na degradação do corante LM sob luz visível. Essa configuração alcançou eficiência de degradação até nove vezes maior do que uma mistura mecânica simples dos dois materiais. O bom desempenho foi atribuído ao acoplamento eficaz entre os semicondutores, formação de um campo elétrico interno e maior absorção de luz

visível promovida pelo Cu_2O, além da supressão da recombinação das cargas fotogeradas.

Com relação a construção de sistemas esquema-Z, Chen et al. [14] desenvolveram um fotocatalisador baseado na combinação de Bi_2O_3 e $NaNbO_3$. Os compósitos apresentaram desempenho fotocatalítico significativamente superior na degradação do corante RhB, atingindo uma taxa de degradação 6,3 vezes maior que a do $NaNbO_3$ puro sob luz UV. Os autores atribuíram esse aumento de eficiência a formação desta estrutura, que promoveu uma eficiente separação dos portadores de carga.

Em outra abordagem, Baeissa et al. [13] reportaram a construção de um compósito Au/$NaNbO_3$. Comparado ao $NaNbO_3$ puro, o compósito apresentou desempenho 22 vezes maior na degradação do corante verde malaquita sob luz visível. Essa atividade foi atribuída a redução do *band gap*, ao aumento da separação dos pares e^-/h^+ e a alta dispersão do Au sobre o $NaNbO_3$, promovendo maior eficiência na geração e transporte das cargas. Embora os autores não mencionem o termo “junção Schottky”, o estudo indica fortemente que se trata desse tipo de junção.

Por fim, um estudo de Chen et al. [51] demonstrou uma abordagem diferente construindo compósitos $NaNbO_3$/Ru. A heteroestrutura apresentou desempenho significativamente superior na degradação do corante RhB sob luz visível. Desempenho atribuído a combinação de auto-fotossensibilização do corante, forte interação na interface Ru/$NaNbO_3$ e ao efeito de “auto-dopagem” por vacâncias de oxigênio no $NaNbO_3$.

2.6 Niobato de sódio como agente antibacteriano

No trabalho desenvolvido por Sharma et al. [56], atividade antibacteriana do $NaNbO_3$ foi investigada por meio da fotopiezocatálise. O material apresentou ação expressiva contra *E. coli.* Esse efeito foi atribuído à atuação conjunta da fotocatálise e da piezocatálise: enquanto a fotocatálise promove a geração dos pares e^-/h^+ por meio da absorção de luz, a piezocatálise contribui para a separação dessas cargas por meio do potencial piezoelétrico gerado. Dessa forma, as cargas fotogeradas têm sua vida útil prolongada, favorecendo a formação de espécies reativas de oxigênio

(ROS), capazes de danificar as estruturas celulares bacterianas. Ainda no campo da piezocatálise, outro estudo de Sharma et al. [57] avaliou a atividade antibacteriana de um compósito $NaNbO_3$/ ZnO. O material foi testado contra *E. coli* e apresentou ação eficaz. No entanto, os autores atribuíram esse efeito à geração de ROS e destacaram exclusivamente a contribuição do ZnO, reconhecido por suas propriedades antibacterianas.

Um estudo conduzido por Ummer et al. [60] investigou a atividade antibacteriana de compósitos $BiFeO_3$/$NaNbO_3$. A análise foi realizada por meio do contato direto dos materiais com as bactérias *E. coli* e *S. aureus*, e os resultados demonstraram a inativação de ambas. Os autores atribuíram esse efeito à liberação de íons metálicos Fe(II) e à geração de ROS que interagem com a parede celular bacteriana, promovendo sua ruptura.

Já no estudo de Min et al. [58], foi explorado um mecanismo alternativo de ativação catalítica, baseado no efeito piroelétrico. Os autores desenvolveram um compósito $NaNbO_3$/CdS e testaram sua atividade sob ciclos térmicos, simulando flutuações de temperatura ambiente. Os resultados indicaram uma elevada taxa de inativação de *Salmonella typhimurium*. A formação da heterojunção foi apontada como responsável pela melhora na separação de cargas, favorecendo assim a formação de ROS.

Por último, Zhang et al. [59] investigaram o uso do $NaNbO_3$ modificado com íons Ca(II) e Mg(II), obtido por sinterização e posterior polarização. Os materiais apresentaram excelente atividade antibacteriana contra *E. coli*, sem a necessidade de qualquer estímulo externo adicional. Esse efeito foi atribuído à alta polarização remanescente e ao elevado potencial elétrico de superfície nas cerâmicas. O estudo indica que a presença de cargas na superfície do material promove a atração das bactérias, facilitando o contato e contribuindo para sua inativação.

3 Artigos

O conteúdo deste capítulo apresenta as abordagens metodológicas e os resultados obtidos referentes ao desenvolvimento da tese, organizados em forma de artigos. Durante o período de pesquisa, foram desenvolvidos cinco artigos, que sintetizam as principais contribuições e avanços alcançados ao longo do doutorado.

3.1 Artigo 1

O artigo intitulado *"Fast synthesis of $NaNbO_3$ nanoparticles with high photocatalytic activity for degradation of organic dyes"* é apresentado conforme publicado no periódico *Journal of the American Ceramic Society* (*Online* ISSN:1551-2916 *and Print* ISSN:0002-7820), classificação A1 na área de Materiais.

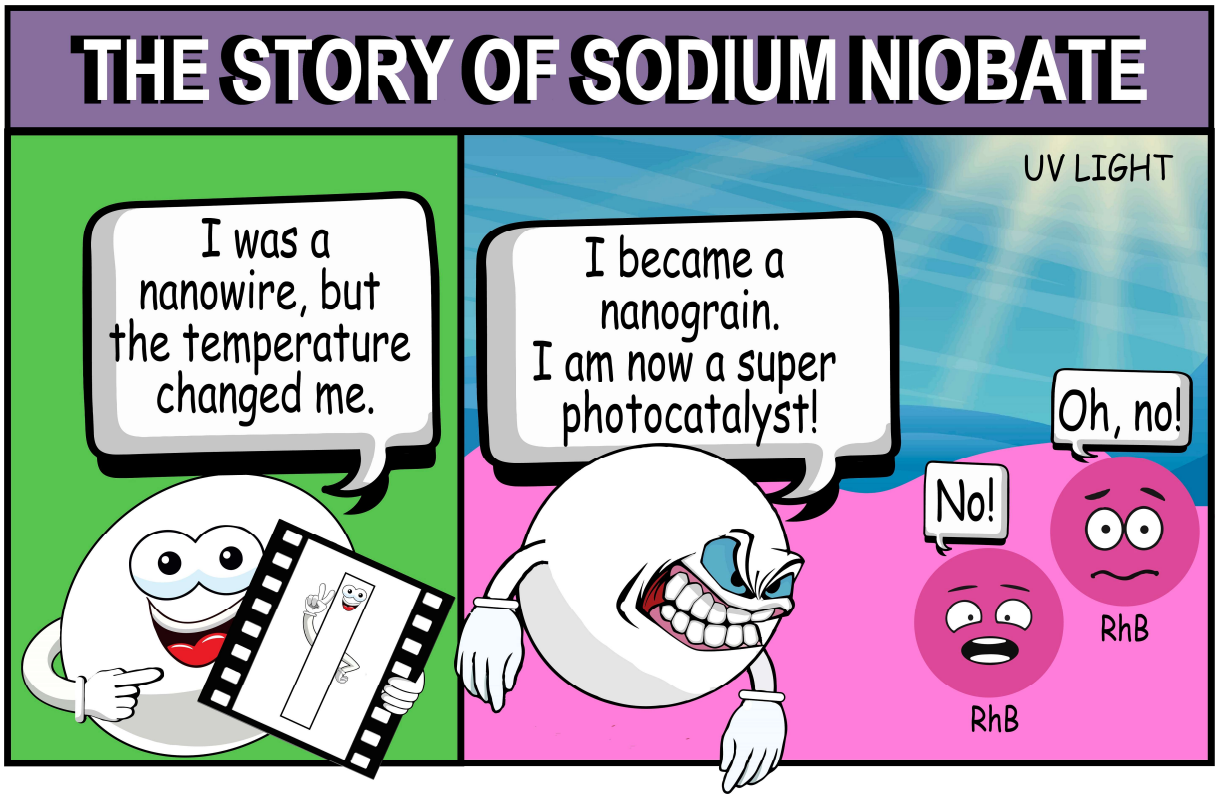

Figura 10 - Resumo gráfico Artigo 1.

Fonte: Elaborado pela autora, 2022.

Fast synthesis of $NaNbO_3$ nanoparticles with high photocatalytic activity for degradation of organic dyes

Daiane Fernandes[a,*], Mateus M. Ferrer[a], Cristiane W. Raubach[a], Mario L. Moreira[a,b], Pedro L.G. Jardim[a,b], Eduardo Ceretta Moreira[c], Carlos F. O. Graeff[d,e], Sergio S. Cava[a,b]

[a]Post-Graduate Program in Materials Science and Engineering, Federal University of Pelotas, 96010-610, Pelotas, RS, Brazil

[b]Post-Graduate Program in Physics, Federal University of Pelotas, 96160-000, Capão do Leão, RS, Brazil

[c]Spectroscopy Laboratory, Federal University of Pampa, 96413-172, Bagé, RS, Brazil

[d]Post-Graduate Program in Materials Science and Technology, São Paulo State University, 17033-360, Bauru, SP, Brazil

[e]Department of Physics, São Paulo State University, 17033-360, Bauru, SP, Brazil

*Corresponding author: daiane.fg.eng@outlook.com

A B S T R A C T

$NaNbO_3$ nanoparticles were obtained using the microwave-assisted hydrothermal method followed by heat treatment. It has been shown that heat treatment to increase the crystallinity of the material and modifies particle shape, from nanowires to nanograins. Nanowires with a diameter of approximately 35 nm and a length of tens of micrometers were obtained in the shortest time ever reported in the literature. Particles in the shape of nanograins with a diameter of approximately 35 nm were obtained by burning the nanowires. The photocatalytic activity of the nanoparticles was investigated through the photodegradation of Rhodamine B dye. Electronic structure analysis using density functional theory (DFT) along with experimental techniques were performed to help understand the photocatalytic activity of each sample. The obtained nanoparticles were highly favorable for photocatalytic applications, especially the nanograins, which degraded 100% of the dye in 50 min.

Keywords: sodium niobate; nanoparticles; photocatalysis; dye degradation.

1. Introduction

Currently, the planet is undergoing progressive technological development and population density, resulting in increased generation of various effluents. Therefore, it is necessary that they receive the appropriate treatment to be degraded into harmless substances or less toxic to the environment and to humans. Among the different treatment methods, the advanced oxidative processes have received increasing attention, because they can totally or partially degrade compounds that are difficult to degrade[1], mainly originating from the textile and pharmaceutical industry.

Heterogeneous photocatalysis is one of the most applied oxidative methods and had its mechanism explained in 1972, by Japanese researchers Fujishima and Honda, who reported the division of water molecules using as photocatalyst the semiconductor Titanium dioxide.[2] In this type of process, the semiconductor when absorbing photons with energy equal to or greater than its band gap value, has its electrons excited from the valence band (VB) to the conduction band (CB), generating an electron/hole pair, thus forming oxidizing and reducing sites on its surface, degrading in turn several pollutants.

Although heterogeneous photocatalysis is a promising and sustainable approach to environmental remediation, existing photocatalysts still face major limitations, for example, the fast recombination of photoinduced charge carriers, limiting photocatalytic activity. For this purpose, great advances have been made using the strategy of building heterostructures, which allows the migration of charges between the materials involved, causing this spatial separation to prevent their rapid recombination.[3-11] Others factors also contribute to the performance of photocatalysts such as crystal structure, particle shape, electronic structure, and others.[12] It is also known that the reduction of the diffusion length is interesting, because the smaller the particle, the smaller the transfer distance of the photogenerated electron to the surface, also because the particle ends up having a high surface/volume ratio and a kinetically desirable structure.[13] This makes nanoscale particles very promising for this application.

Sodium niobate ($NaNbO_3$) is a semiconductor that has Perovskite crystal structure, that is, has ABX_3 type stoichiometry, where the A and B sites are occupied by metallic cations and the X site is occupied by an element of the non-metals

group.[14] It has many technological application properties and, among them, the photocatalytic applications presented in the literature showed excellent results.[13,15-23] Being a promising photocatalyst because it is thermodynamically stable, has high corrosion resistance and is non-toxic.[22,24] However, studies have shown that the natural particle shape of $NaNbO_3$ is cubic and presents low photocatalytic activity, but in syntheses with hydrothermal conditions followed by heat treatment it is possible to obtain the semiconductor in the form of nanowires, with high photocatalytic activity.[15,18,21,25]

Under hydrothermal conditions, before the formation of $NaNBO_3$, a metastable phase of sodium hexaniobate nanowires is formed ($Na_2Nb_2O_6.H_2O$) and as the synthesis process progresses, the process of nucleation of the crystals in the form of cubes on the wires occurs, through the Ostwald ripening.[18,25-29] To obtain Perovskite in the shape of nanowires, it is necessary that its nucleation takes place in a confined space, with short-range diffusion, as is the heat treatment step.[18] Therefore, to obtain $NaNbO_3$ in the form of nanowires, it is necessary to synthesize $Na_2Nb_2O_6.H_2O$ and apply a subsequent heat treatment.[18,25-29]

To date, $NaNbO_3$ particles in the form of nanowires are extensively studied, as they are considered the most promising for photocatalytic applications. Several research has been devoted to elucidating its growth process and comparing it with the natural cubic particle. However, Farooq et. al.[13] obtained nanoparticles with a grain/cuboid shape with sizes between 5-30nm, with high photocatalytic activity. The nanoparticles were obtained by the polymeric citrate precursor method, for 22 h and then calcined for 12 h. Given the above, it is highly desirable to study other synthesis routes, preferably faster, to obtain this type of nanoparticle and compare with the nanowires. Therefore, in the present work, we present a shorter time route to obtain $NaNbO_3$ nanowires and we demonstrated that it is possible to obtain nanoparticles similar to those reported by Farooq et. al.[13], in a shorter time as well, through the ‘’breaking’’ of these nanowires. The samples obtained had their photocatalytic activity measured through the photodegradation of Rhodamine B (RhB), a dye widely used in industries and known for its high toxicity, good stability and non-biodegradability.[30] An analysis of electronic structure using first-principles calculations based on density functional theory (DFT) together with experimental techniques were performed to understand the photocatalytic activity of each sample. Therefore, in the present work,

we present a shorter time route to obtain $NaNbO_3$ nanowires, through microwave-assisted hydrothermal synthesis, followed by a heat treatment process. The heat treatment was carried out at temperatures between 300 ºC and 800 ºC, to analyze the influence on the crystalline structure, electronic structure, particle shape and photocatalytic activity, which was measured through the photodegradation of Rhodamine B (RhB), a dye widely used in industries and known for its high toxicity, good stability and non-biodegradability.[30] An analysis of electronic structure using first-principles calculations based on density functional theory (DFT) together with experimental techniques were performed to understand the photocatalytic activity of each sample.

2. Experimental procedure

2.1. Sample preparation

The samples were obtained according to the synthesis presented in a previous study[31], with some modifications. NaOH (Merck, 99.0%) and $NbCl_5$ (Brazilian Mining and Metallurgy Company, 99.0%) were solubilized in distilled water by magnetic stirring at room temperature, com concentrations of 6 M and 0.6 M, respectively. This solution was heated at 180 ºC in the adapted microwave (800 W, 2.45 GHz, PANASONIC) for 15 min. The precipitate obtained was washed and centrifuged until the pH was neutralized and then oven dried overnight. The final powder was submitted to a thermal treatment in a tubular oven at 300-800 ºC during 2 h using a heating rate of 10 ºC/min and naturally cooled to room temperature.

2.2. Sample characterization

The thermal analyzes were investigated using a TG-DTA-DTG equipment (STA449F3, NETZSCH), with atmosphere controlled by nitrogen. X-ray diffraction was performed using a diffractometer (Ultima IV, RIGAKU) with Cu-Kα radiation (λ=1.5406 Å), scanning from 2θ of 10° to 90° with speed of 10°/min. Micrographs were obtained by scanning electron microscopy using a FEG electron microscope (JSM7500F, JEOL). The transmission electron microscopy (TEM) images were performed in an electron microscope (CM200, PHILIPS) operated at 200 Kv. The optical gap of the samples was estimated by diffuse reflection spectroscopy by a UV-Vis spectrometer (HR2000+, OCEAN OPTICS). The photoluminescence of the

samples was analyzed using a fluorescence spectrometer (Cary Eclipse, AGILENT), with excitation laser of 280 nm. The surface area estimated using equipment (Quantchrome Instrument, Nova 4200) in the presence of liquid nitrogen (77 K). The surface area was determined using the Multipoint Brunauer, Emmett and Teller (BET) equation, done automatically by the instrument.

2.3. Photocatalytic analysis

The photocatalytic activity of each sample was evaluated through the degradation of the organic dye RhB ($C_{28}H_{31}ClN_2O_3$), in solution. The experiment was carried out in a closed box at a temperature of 25 °C, internally lit by five UVC lamps of 15 W each (TUV, PHILIPS, maximum intensity at 254 nm). The photocatalytic reaction was carried out with 25 mg of powder dispersed in 50 mL of RhB solution (1×10^{-5} mol.L^{-1}), under magnetic stirring. Each sample was first stirred in the solution in the dark for 30 min, to achieve the balance between adsorption and desorption. After the light was on, aliquots of the solution were collected and centrifuged for further analysis of absorption. The variation in RhB concentration was recorded by monitoring the absorbance at 554 nm, using a UV-Vis spectrophotometer (SP200 UV, BEL PHOTONICS).

For reuse tests, each powder was separated by centrifugation after analysis, washed once with distilled water and once with ethanol and dried. The powders were then weighed, and the ratio between catalyst (0.5 mg) and the RhB solution (1 mL) was maintained.

2.4. Theoretical calculations

Density Functional Theory (DFT) was used to evaluate the electronic structure. The simulations were performed using the CRYSTAL17 package[32] with the HSE06 hybrid functional. Such a functional was selected because it generated values close to the experimental results.[33] All atomic basis was defined using Triple-Zeta Valence with Polarization Gaussian basis sets (POB-TZVP), Na center developed by Oliveira et al.[34] and Nb and O centers by Laun et al.[35] The Coulomb and exchange series thresholds (overlap and penetration for Coulomb integrals, the overlap for HF exchange integrals, and the pseudo-overlap) used in the CRYSTAL17 package, were

set as 8, 8, 8, 8, 16 (10–8, 10–8, 10–8, 10–8, and 10–16). The Pack–Monkhorst and Gilat net parameters were set as 6 and 6, respectively.

The phase evaluation was performed according Rietveld refinement analysis of the XRD patterns using General Structure Analysis System (GSAS) program.[35] In this simulation, the background and the peak profiles was adjusted using a Chebyshev polynomial of the first kind and Thompson-Cox-Hastings pseudo-Voigt (pV–TCH), respectively.[36]

3. Results and discussion

3.1. Structural and morphological characterization

Figure 1 shows the XRD patterns of the sample as prepared and with different heat treatment temperatures. The peaks observed in the sample as prepared suggest the structure reported as $Na_2Nb_2O_6 \cdot H_2O$, monoclinic phase, space group C2/c, with the cell parameters: a=17.114 Å, b=5.0527 Å, c=16.5587 Å and β=113.947º.[18,25-29,31,38-46] As the heat treatment temperature of 300 °C is applied, it is possible to observe that the peaks located in 2θ=11º-14º and 28º-31º, characteristic of the $Na_2Nb_2O_6 \cdot H_2O$ phase, begin to decrease. Raising the temperature to 400 °C, and there is the appearance of the peaks of the $NaNbO_3$ phase. In samples treated between 500 °C and 800 °C, only the peaks belonging to a single-phase $NaNbO_3$ phase are observed, orthorhombic phase, space group P21ma (JCPDS 82-606).[13,39,47] In the sample tratead 600 ºC is possible to observe a shift in the main peaks, possibly caused by the diffusion of sodium ions in the lattice. When this occurs, the material reduces its surface area to reduce free energy caused by the tension in the lattice. At 700 ºC, the volatilization of sodium ions occurs and the free energy decreases and the surface area increases again. This behavior is seen in the samples, as presented in Section 3.5. In addition, the mean value of the crystallographic domains was estimated by the Scherrer equation, resulting in 21.90 nm, 23.13 nm, 24.05 nm and 27.43 nm for the $NaNbO_3$ samples treated at 500 ºC, 600 ºC, 700 ºC and 800 ºC, respectively. This demonstrates an increase in crystallinity as the temperature rises, as can be seen by the more defined diffraction peaks as well. The crystalline phase of the $NaNBO_3$ samples was confirmed by Rietveld refinement (Fig. S1, Table S1). All samples showed good convergence to the orthorhombic phase P21ma, according to χ^2 and RBragg (Table S2).

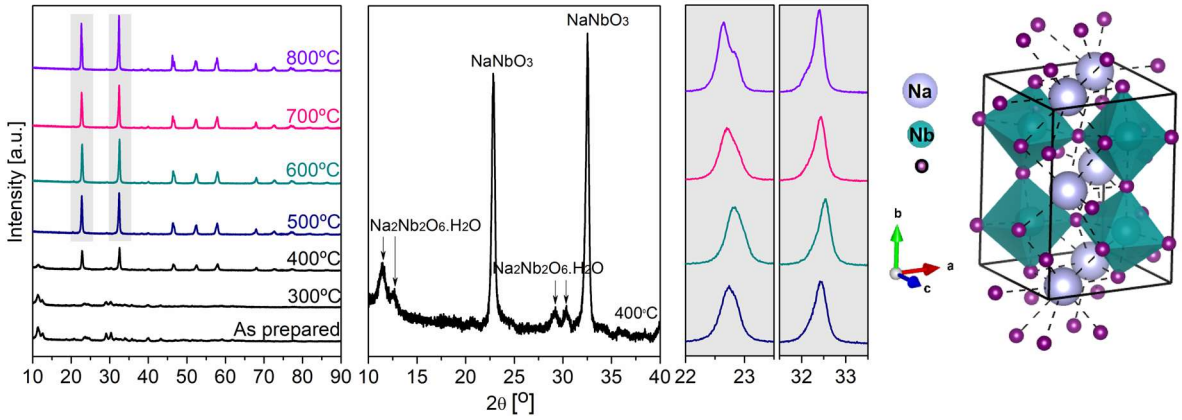

Figure 1. XRD patterns.

To better understand the processes involved in the formation and transformation of the Perovskite phase, a TG-DTA-DTG thermal analysis was performed, shown in Figure 2. Through the TG curve, an initial mass loss is observed that occurs until the temperature of 181 °C, this activity corresponds to the evaporation of the water adsorbed on the surface of the $Na_2Nb_2O_6 \cdot H_2O$. Between the temperatures of 181 ºC and 305 ºC, an endothermic peak is observed, accompanied by another loss of mass, this activity corresponds to the dehydration of the $Na_2Nb_2O_6 \cdot H_2O$.[18,25-29,31,38-46] The DTA curve shows a sharp exothermic peak in the temperature range between 487 °C and 549 °C, without mass loss indicating the complete formation of the $NaNbO_3$ phase, result compatible with that observed in XRD (Figure 1). From 620 °C, an endothermic event is observed in the DTA curve with a mass loss, indicating that from this temperature onwards, the volatilization of sodium ions occurs. At high temperatures, the evaporation of alkaline ions is high.[47,48]

Micrographs of the sample as prepared and at different heat treatment temperatures are shown in Figure 3. The sample as prepared (Figure 3a) has a nanowire particle shape, compatible with $Na_2Nb_2O_6 \cdot H_2O$[18,25-29,38-46], with an average diameter of approximately 35 nm and a length of tens of micrometers. With heat treatment at 500 ºC (Figure 3b), where the complete formation of $NaNbO_3$ occurs, the shape of nanowires is preserved, without significant changes. When the temperature is raised to 600 ºC (Figure 3c) and 700 ºC (Figure 4d), it is possible to observe that the nanowires begin to break and turn into smaller particles, due to the rearrangement of crystals.[47,49] In the sample treated at 800 ºC (Figure 3e), particles in the form of nanowires are no longer observed, but a nanograin-like particle with an

average diameter of approximately 35 nm. In addition, TEM was performed on the samples treated at 500 ºC (Fig. 4a) and 800 ºC (Fig. 4b), to better observe the morphological aspects and the size of the nanoparticles. Through this analysis, it is observed that both sample present shape and size consistent with the micrographs obtained by SEM.

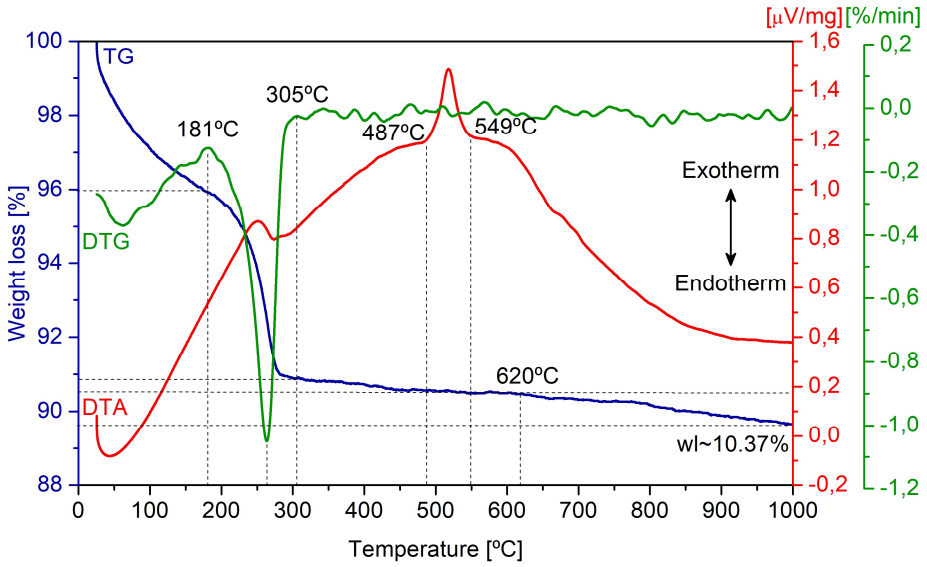

Figure 2. TG-DTA-DTG curves.

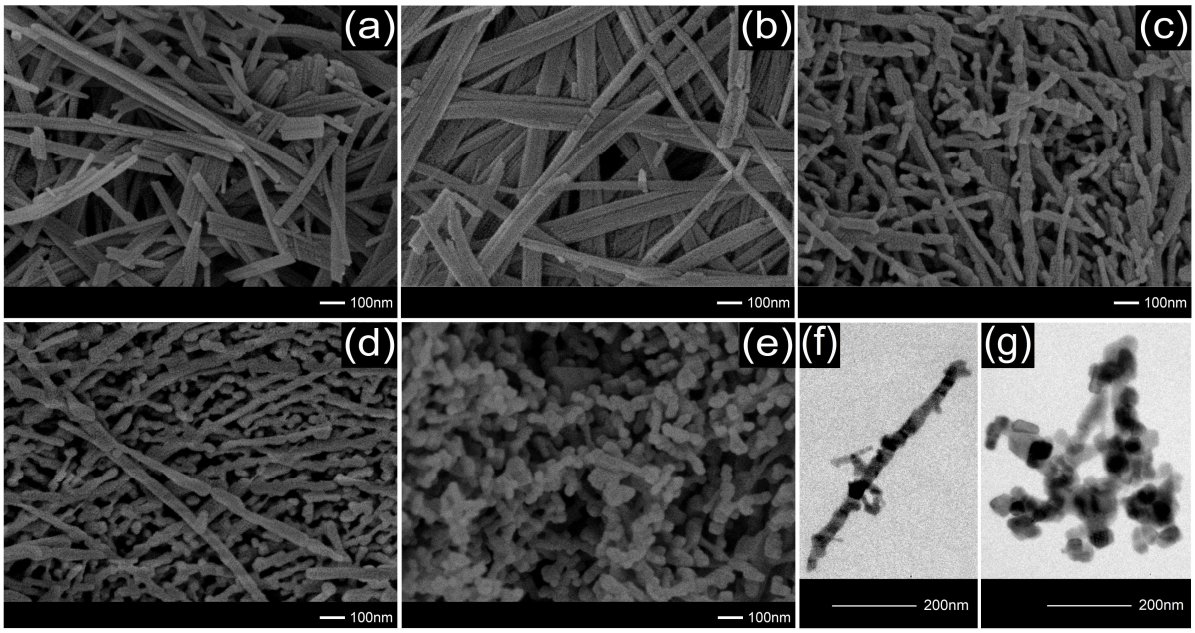

Figure 3. SEM-FEG: (a) as prepared, (b) 500 °C, (c) 600 °C, (d) 700 °C, (e) 800 ºC, and TEM: (f) 500 °C, and (g) 800 °C.

Gu et al.[47] presented a study, where through a solvothermal synthesis, at 230 ºC for 16 h, using isopropanol as a reaction medium, obtained 1D particles of $Na_7(H_3O)Nb_6O_{19}.14H_2O$. That after being subjected to heat treatment for 4 h, at different temperatures with a maximum of 800 ºC, gave rise to $NaNbO_3$ particles with the same particle shape transformation process obtained in this work. However, the precursor $Na_7(H_3O)Nb_6O_{19}.14H_2O$ presented a larger particle diameter, approximately 193.2 nm, resulting in $NaNbO_3$ 1D with a diameter of approximately 305.1 nm and $NaNbO_3$ in the form of ellipsoids with a width and length of approximately 512.3 and 548.6 nm, respectively. Therefore, we can observe with this study that the 1D precursor of $Na_2Nb_2O_6{\cdot}H_2O$ originates 1D $NaNbO_3$ particles with very small diameter and by raising the heat treatment temperature above 700 ºC, it was possible to obtain even smaller particles, highly desirable for photocatalytic applications. Furthermore, given the results presented, it is also possible to verify the obtaining of $NaNbO_3$ nanowires in a shorter time already reported in the literature (Table 1).

Table 1

Synthesis that obtained $NaNbO_3$ nanowires.

SYNTHESIS METHOD Temperature/Time	HEAT TREATMENT Temperature/Time	REFERENCE
HID-C 183 ºC/2 h	600 ºC/6 h	Alexandre et. al. [32]
HID-AM 150 ºC/1 h	350 ºC/2 h	Fernandes et. al. [22]
HID-C 150 ºC/4 h	400 ºC/12 h	Jung et. al. [28]
HID-C 120 ºC/3 h	400 ºC/NE	Ke et. al. [18]
HID-C 180 ºC/2 h	300 ºC/12 h	Liu et. al. [9]
HID-C 140 ºC/6 h	700 ºC/3 h	Pei et. al. [35]
HID-C 200º C/24 h	550 ºC/4 h	Shi et. al. [12,16]
HID-AM 180 ºC/60 min	550 ºC/4 h	Teixeira et. al. [20]
HID-AM 180 ºC/30 min	550 ºC/4 h	Teixeira et. al. [31]
HID-C 200 ºC/8 h	400 ºC/3 h	Wang. et. al [33]
HID-C 160 ºC/6 h	NE/NE	Wang et. al. [34]
HID-C 150 ºC/10 h	NE/NE	Yu et. al. [19]
HID-C 160 ºC/6 h	500 ºC/2 h	Zhang et. al. [30]

HID-C (Conventional hydrothermal), HID-AM (Microwave-assisted hydrothermal) and NE (Not specified).

3.2. Photocatalytic performance

3.2.1. Photocatalytic activity

The photocatalytic activity of each $NaNbO_3$ sample was evaluated by the degradation of the RhB dye in solution, as described in the experimental procedure. Figure 5a shows the dye concentration curves over the analysis time, where C_0 and C indicate the initial concentration of RhB and concentration at a specific time (min), respectively. Through the dye curve, without the semiconductor, it is observed that has a very low photolysis process. Photocatalytic activity is increased using the samples treated with higher heat treatment temperature, reaching maximum dye removal in 50 min. All samples showed high photocatalytic activity, reaching a maximum percentage of dye degradation of 100% and minimum of 72% in a period of 50 min, using the sample treated at 800 °C and 500 °C, respectively. Figure 5b shows the kinetics of RhB degradation in the presence of each sample of $NaNbO_3$.The reaction rate constant (k) was determined using the linear relationship, $-\ln(C/C_0) = kt$, where t is the time in minutes.[1] The results indicate that the dye degradation follows the pseudo-first order kinetics and that the sample treated at 800 ºC has a dye removal rate of 3.09, 2.89 and 1.5 times greater than the sample treated at 500 ºC, 600 ºC and 700 ºC, respectively.

3.2.2. Photocatalytic stability

For the practical application of catalysts, the stability is of great importance. For such, a reuse experiment was carried out, using the samples treated at 500 °C and 800 °C. After 3 consecutive cycles, it was possible to verify that both samples maintained the same photocatalytic performance (Fig. 5c) This demonstrates that $NaNbO_3$ can be considered a stable and highly efficient photocatalyst.

3.2.3. Photocatalytic mechanism

To better understand the mechanism of dye degradation in the photocatalytic process, experiments to identify the active species were performed with samples treated at 500 °C and 800 °C. Isopropyl alcohol (C_3H_8O), silver nitrate ($AgNO_3$), and disodium ethylenediaminetetraacetate (EDTA) were used as scavengers for hydroxyl radicals (·OH), electrons (e^-) and holes (h^+), respectively. Figure 5d shows the percentage of RhB degradation with the presence of scavengers at the end of 50 min.

It is observed that both photocatalysts present similar behavior. The addition of EDTA and C_3H_8O inhibited the degradation of the dye, indicating that the main active species during the photocatalysis process are h^+ and ·OH. In contrast, the addition of $AgNO_3$ in the photocatalytic solution using the sample treated at 500 ºC caused an increase in the discoloration percentage of RhB, from 72% to 100%. This indicates that the restriction of e^- left a greater number of h^+ available to act in the oxidation of the dye. For the reaction using the using the sample treated at 800 ºC the percentage of discoloration was the same 100% with the addition of $AgNO_3$, indicating that the e^- are not active species in the photocatalysis process studied here.

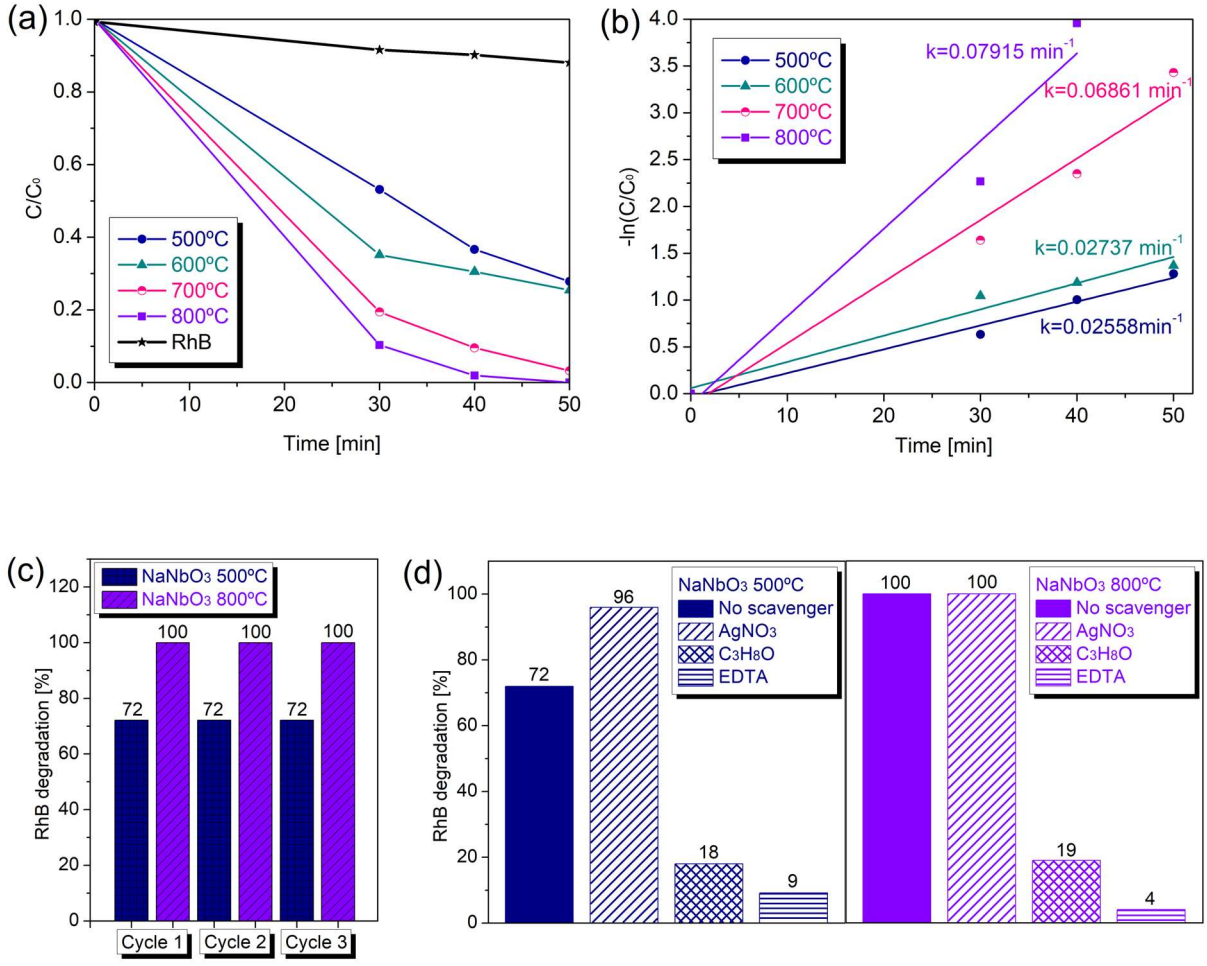

Figure 4. (a) Variation in the RhB concentration with time, (b) Kinetic linear simulation curves of RhB degradation, (c) Reuse of the photocatalysts for 3 cycles, and (d) Percentage of RhB degradation using scavengers.

3.3. DFT Calculations

Figure 6a show the band structure orthorhombic P21ma (O-$NaNbO_3$). The bands demonstrate that the semiconductor O-$NaNbO_3$ presents a direct band gap, with transition at point Γ → Γ and energy of the 3.6 eV. Figure 6b shows pDOS. It is observed that VB is composed mainly by the O 2p orbital and the CB by the Nb 4d orbital. Therefore, its optical gap is mainly determined by these orbitals. In both bands there is a small hybridization between the O 2p/Nb 4d and there are almost no electronic states of Na. This electronic nature is consistent with the literature.[20-22,50-52] The absence of electronic states of Na is due to their high ionicity, which makes it difficult to bond with other atoms by hybridization.[50]

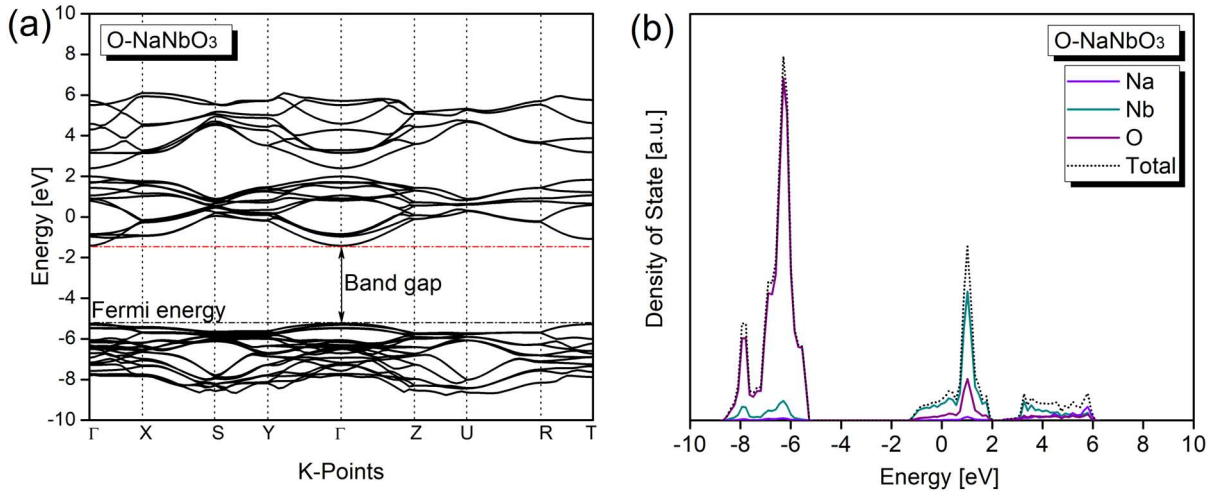

Figure 5. (a) Calculated band structure of $NaNbO_3$ and (b) The pDOS of the $NaNbO_3$.

3.4. Optical characterization

Based on information obtained from the theoretical study of electronic structure, the band gap of the samples was estimated through diffuse reflectance by the Wood/Tauc method.[53] Using the equation $(\alpha h\nu)^n = A(h\nu - Eg)$ where α, h, v, n, A and Eg are the absorption coefficient near the absorption edge, Planck's constant, frequency of light, constant related to the type of electronic transition of the material (n=2 for the direct gap), proportionality constant and band gap energy, respectively. Estimated values are shown in Figure 7a. The samples treated at 500 ºC, 700 ºC and

800 ºC showed a band gap of 3.50 eV, 3.52 eV and 3.55 eV, respectively. This increase occurs due to the increase in crystallinity, as shown by the calculation of crystallographic domains, as the bands are better delimited, making the superposition of wave functions more defined. However, the sample treated at 600 ºC has a band gap of 3.45 eV. This band gap reduction in the material is a consequence of the reduction of the lattice distance that generates a greater expansion of the energy level.[54] Therefore, the sample treated at 600 °C has a slightly smaller band gap because it has smaller cell parameters, as shown by the deviations of diffraction peaks for larger angles, shown in Figure 1. The reduction in bandgap favors photocatalysis, as the semiconductor requires less energy to activate. However, this behavior was not observed in the samples. The band gap does not seem to significantly influence the performance of the photocatalysts studied here.

To complement the understanding of the photocatalytic activity variation between the samples, Photoluminescence spectroscopy (PL) technique was performed, that allows to know the behavior of the recombination of the electron-hole pairs, important criterion for understanding the performance of photocatalysts. The PL emission spectra are shown in Figure 7b. All samples showed similar behavior, with broadband PL in the region between 300 and 450 cm^{-1}, with main emission peaks at 362 and 383 nm, corresponding to an energy of 3.42 and 3.24 eV, respectively. This broadband emission indicates that the recombination takes place by a multiphonon process, in other words, the relaxation occurs with the participation of various energy states, caused by intrinsic defects in the material.[55,56] These intermediate electronic levels are associated with shallow defects, of surface, responsible for the emission of PL in regions of high energy (violet/blue).[57] The presence of these defects favors photocatalysis, because they delay recombination of the photogenerated electron/hole pair. This indicates that the increase in photocatalytic activity is related to the crystallinity of the samples. The more crystalline the lattice, the lower the rate of recombination of the photogenerated charges.

3.5. Surface area analysis

Another important factor that affects photocatalytic activity is surface area. It is known that the greater the surface area of the catalyst, the greater the probability of

available and accessible active sites and also dye adsorption sites.[13,58] As shown in section 3.1, the sample treated at 600ºC showed a deviation in the diffraction peaks, possibly caused by the diffusion of sodium ions in the lattice. When this occurs, the material reduces its surface area to reduce free energy caused by the tension in the lattice. When the temperature is raised, the volatilization of the alkali metal decreases the free energy and the area increases again. This behavior is seen in the samples, which presented surface areas of 28 m²/g, 11 m²/g, 31 m²/g and 32 m²/g for temperatures of 500 ºC, 600 ºC, 700 ºC e 800 ºC, respectively. The increase in surface area is also a consequence of the change in particle shape. Sodium volatilization detaches the crystals initially arranged in the nanowires that ‘’break’’ turning into smaller particles with the shape of nanograins (Figure 3).

Although the sample treated at 500 ºC had a surface area more than twice that of the sample treated at 600 ºC, its photocatalytic activity was lower. This demonstrates that even the surface area being a determining factor for most photocatalysts, it does not directly influence these $NaNbO_3$ samples. The nanograins obtained at 800 ºC showed a slightly larger area compared to the nanowires at 500 ºC, and we observed that their photocatalytic performance was superior. This possibly occurs because the decrease in particle size leads to a reduction in the recombination of charge carriers, as the migration time to the surface is proportional to the square of the particle size.[59] Small particles also have more atoms with incomplete coordination, which makes them more reactive. This demonstrates that particle shape appears to play a very important in photocatalytic activity.

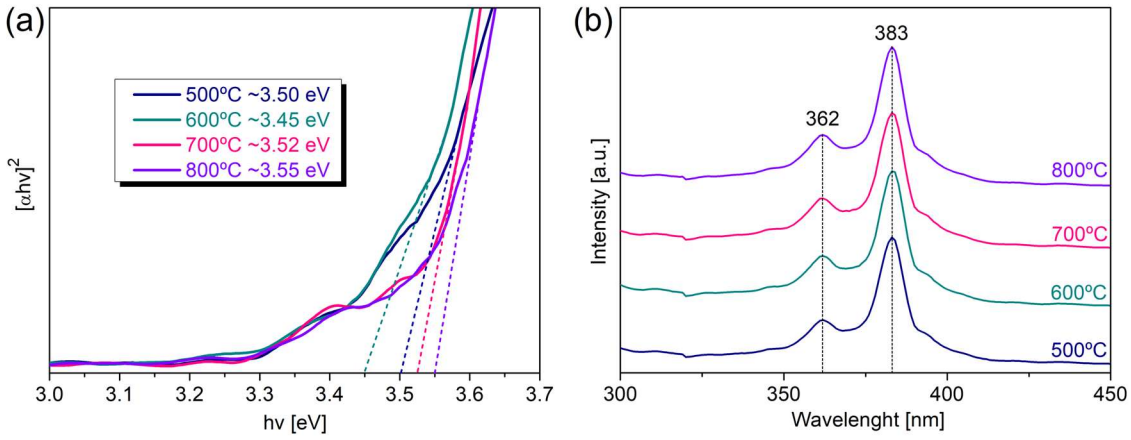

Figure 6. (a) Band gap of the $NaNbO_3$ samples and (b) Photoluminescence curves of the $NaNbO_3$ samples.

4. Conclusions

In this study, we propose a method to obtain $NaNbO_3$ nanowires through the microwave-assisted hydrothermal system, followed by heat treatment, in a shorter time. We demonstrated that with a simple heat treatment it was possible to change the shape of the particles, from nanowires to nanograins. The heat treatment increased the crystallinity of the samples without modifying the phase. All samples showed high photocatalytic activity, especially the nanograins. It was found that the factors that influence the performance of the samples studied here were the crystallinity and shape of the particle. Reuse tests demonstrated the stability of the photocatalysts. Therefore, this study contributes information to obtain highly favorable nanoparticles $NaNbO_3$ for photocatalytic applications.

Acknowledgments

The authors thank Companhia Brasileira de Metalurgia e Mineração (CBMM) for donating the niobium precursor, Núcleo de Apoio à Pesquisa em Ciência e Engenharia de Materiais (NAPCEM-UNIFESP Campus São José dos Campos) for XRD and BET analysis, Laboratory of Thermal Analysis - Department of Chemistry (UNESP Campus Bauru) for TG-DTG-DTA analysis and to colleagues Thissiana Fernandes, Paola Gay, Ramon Dadalto, Silvia Cucatti, Luciano Gularte, Catia Ucker, Caroline Schmechel, Lucas Barcellos, Cristian Fernandes and Fabio Riemke for their support in laboratory activities. This research received support from Coordenação de Aperfeiçoamento de Pessoal de Nível Superior (CAPES), Conselho Nacional de Desenvolvimento Científico e Tecnológico (CNPq) and Fundação de Amparo à Pesquisa do Estado do Rio Grande do Sul (FAPERGS) (17/25510000889-8).

References

1. Ücker CL, Goetzke V, Almeida SR, et al. Photocatalytic degradation of rhodamine B using Nb2O5 synthesized with different niobium precursors: Factorial design of experiments. Ceram. Int. 2021; 47(14):20570-20578.

2. Fujishima A, Honda K, Electrochemical Photolysis of Water at a Semiconductor Electrode. Nature. 1972; 238:37-38.

3. Li S, Hu S, Jiang W, et al. In situ construction of WO3 nanoparticles decorated Bi2MoO6 microspheres for boosting photocatalytic degradation of refractory pollutants. J. Colloid Interface Sci. 2019; 556:335-344.
4. Li S, Chen J, Hu S, et al. Facile construction of novel Bi2WO6/Ta3N5 Z-scheme heterojunction nanofibers for efficient degradation of harmful pharmaceutical pollutants. Chem. Eng. J. 2020; 402: 126165.
5. Li S, Wang C, Liu Y, et al. Photocatalytic degradation of antibiotics using a novel Ag/Ag2S/Bi2MoO6 plasmonic p-n heterojunction photocatalyst: Mineralization activity, degradation pathways and boosted charge separation mechanism. Chem. Eng. J. 2021; 415:128991.
6. Li S, Wang C, Liu Y, et al. Photocatalytic degradation of tetracycline antibiotic by a novel Bi2Sn2O7/Bi2MoO6 S-scheme heterojunction: Performance, mechanism insight and toxicity assessment. Chem. Eng. J. 2022; 429:132519.
7. Wang C, Cai M, Liu Y, et al. Facile construction of novel organic–inorganic tetra (4-carboxyphenyl) porphyrin/Bi2MoO6 heterojunction for tetracycline degradation: Performance, degradation pathways, intermediate toxicity analysis and mechanism insight. J. Colloid Interface Sci. 2022; 605:727-740.
8. Wang C, Li S, Cai M, et al. Rationally designed tetra (4-carboxyphenyl) porphyrin/graphene quantum dots/bismuth molybdate Z-scheme heterojunction for tetracycline degradation and Cr(VI) reduction: Performance, mechanism, intermediate toxicity appraisement. J. Colloid Interface Sci. 2022; 619:307-321.
9. Li S, Wang C, Cai M, et al. Facile fabrication of TaON/Bi2MoO6 core-shell S-scheme heterojunction nanofbers for boosting visible-light catalytic levofloxacin degradation and Cr(VI) reduction. Chem. Eng. J. 2022; 428:131158.
10. Li S, Cai M, Wang C, et al. Rationally designed Ta3N5/BiOCl S-scheme heterojunction with oxygen vacancies for elimination of tetracycline antibiotic and Cr(VI): Performance, toxicity evaluation and mechanism insight. J. Mater. Sci. Technol. 2022; 123:177-190.
11. Li S, Cai M, Liu Y, et al. In situ construction of a C3N5 nanosheet/Bi2WO6 nanodot S-scheme heterojunction with enhanced structural defects for the efficient photocatalytic removal of tetracycline and Cr(vi). Inorg. Chem. Front. 2022; 9:2479-2497.

12. Grabowska E. Selected perovskite oxides: characterization, preparation and photocatalytic properties-a review. Appl. Catal. B: Environ. 2016; 186:97-126.
13. Farooq U, Phul R, Alshehri S, et al. Electrocatalytic and enhanced photocatalytic applications of sodium niobate nanoparticles developed by citrate precursor route. Sci. Rep. 2019; 9:4488.
14. Giorgi G, K. Yamashita, K. Organic-inorganic halide peroviskites: an ambipolar class of materials with enhanced photovoltaic performances. J. Mater. Chem. A. 2015; 3(17):8981-8991.
15. Yan C, Li B, Wang J. A Comparative Study of Photodegradation Behavior Sodium Niobate Nanowires and Microcubes. Key Eng. Mater. 2020; 861:221-227.
16. Van ND. Template-free synthesis and photocatalytic activity of {001}-facets exposed rhombohedral NaNbO3 microcrystals. Ceram. Int. 2018; 44(16):19945-19949.
17. Li G, Yi Z, Bai Y, et al. Anisotropy in photocatalytic oxidization activity of NaNbO3 photocatalyst. Dalton Trans. 2012; 41(34):10194-10198.
18. Liu Q, Zhang L, Chai Y, et al. Facile fabrication and mechanism of single-crystal sodium niobate photocatalyst: insight into the structure features influence on photocatalytic performance for H2 evolution. J. Phys. Chem. C. 2017; 121(46):25898-25907.
19. Nawaz M, Almofty SA, Qureshi F. Preparation, formation mechanism, photocatalytic, cytotoxicity and antioxidant activity of sodium niobate nanocubes. Plos One. 2018; 13(9):e0204061.
20. Hamilton A, O'donnell S, Zoellner B, et al. Flux-mediated synthesis and photocatalytic activity of NaNbO3 particles. J. Am. Ceram. Soc. 2019; 103(1):454-464.
21. Shi H, Wang T, Chen J, et al. Photoreduction of Carbon Dioxide Over NaNbO3 Nanostructured Photocatalysts. Catal. Lett. 2011; 141:525-530.
22. Li P, Ouyang S, Xi G, et al. The effects of crystal structure and electronic structure on photocatalytic H2 evolution and CO2 reduction over two phases of perovskite-structured NaNbO3. J. Phys. Chem. C. 2012; 116(14):7621-7628.
23. Fresno F, Jana P, Reñones P, et al. CO2 reduction over NaNbO3 and NaTaO3 perovskite photocatalysts. Photochem. Photobiol. Sci. 2017; 16(1):17-23.

24. Ahmad T, Farooq U, Phul R. Fabrication and Photocatalytic Applications of Perovskite Materials with Special Emphasis on Alkali Metal based Niobates and Tantalates. Ind. Eng. Chem. Res. 2018; 57(1):18-41.
25. Shi H, Li X, Wang D, et al. NaNbO3 nanostructures: facile synthesis, characterization, and their photocatalytic properties. Catal. Lett. 2009; 132:205-212.
26. Paula AJ, Zaghete MA, Longo E, et al. Microwave-assisted hydrothermal synthesis of structurally and morphologically controlled sodium niobates by using niobic acid as a precursor. Eur. J. Inorg. Chem. 2008; 2008(8):1300-1308.
27. Ke T-Y, Chen H-A, Sheu H-S, et al. Sodium niobate nanowire and its piezoelectricity. J. Phys. Chem. C. 2008; 112(24):8827-8831.
28. Yu A, Qian J, Liu L, et al. Surface sprouting growth of Na2Nb2O6·H2O nanowires and fabrication of NaNbO3 nanostructures with controlled morphologies. Appl. Surf. Sci. 2012; 258(8):3490-3496.
29. Teixeira GF, Zaghete MA, Varela JA, et al. Synthesis and Characterization of NaNbO3 Mesostructure by a Microwave-Assisted Hydrothermal Method. Mater. Res. Soc. 2014; 1675:145-150.
30. Lops C, Ancona A, Di Cesare K, et al. Sonophotocatalytic degradation mechanisms of Rhodamine B dye via radicals generation by micro- and nano-particles of ZnO. Appl. Catal. B: Environ. 2019; 243:629-640.
31. Fernandes D, Raubach CW, Jardim PLG, et al. Synthesis of NaNbO3 nanowires and their photocatalytic activity. Ceram. Int. 2021; 47(7):10185-10188.
32. Dovesi R, Erba A, Orlando R, et al. Quantum-Mechanical Condensed Matter Simulation swith CRYSTAL. WIREs Comput. Mol. Sci. 2018; 8(4):e1360.
33. Krukau AV, Vydrov OA, Izmaylov AF, et al. Influence of the exchange screening parameter on the performance of screened hybrid functionals. J. Chem. Phys. 2006; 125:224106.
34. Oliveira DV, Laun J, Peintinger MF, et al. BSSE-correction scheme for consistent gaussian basis sets of double- and triple-zeta valence with polarization quality for solid-state calculations. J. Comput. Chem. 2019; 40(27):2364-2376.
35. Larson AC, Von Dreele RB. GSAS. Gem. Report lAUR. 1994; 86-748.
36. Thompson P, Cox DE. Hastings, J. B. Rietveld Refinement of Debye-Scherrer Synchrotron X-ray Data from Al2O3. J. Appl. Crystallogr. 1987; 20:79- 83.

37. Laun J, Oliveira DV, Bredow T. Consistent Gaussian basis sets of double- and triple-zeta valence with polarization quality of the fifth period for solid-state calculations. J. Comput. Chem. 2018; 39(19):1285-1290.
38. Xu H, Nyman M, Nenoff TM, et al. Prototype Sandia Octahedral Molecular Sieve (SOMS) Na2Nb2O6,H2O: Synthesis, Structure and Thermodynamic Stability. Chem. Mater. 2004; 16(10):2034-2040.
39. Jung JH, Chen C-Y, Wu WW, et al. In Situ Observation of Dehydration-Induced Phase Transformation from Na2Nb2O6-H2O to NaNbO3. J. Phys. Chem. C. 2012; 116(42):22261-22265.
40. Ji S, Liu H, Sang Y, et al. Synthesis, structure, and piezoelectric properties of ferroelectric and antiferroelectric NaNbO3 nanostructures. Cryst. Eng. Comm. 2014; 16(32):7598-7604.
41. Zhang D, Cheng J, Shi F, et al. Low temperature synthesis of ribbon-like orthorhombic NaNbO3 fibers and their photocatalytic activities for H2 evolution. RSC Adv. 2015; 5(42)33001-33007.
42. Teixeira GF, Ciola RA, Sakamoto WK, et al. Perovskite-Based mesostructures and related composites-influence exerted by morphology and interface. In: Barranco AP, editor. Ferroelectric Materials-Synthesis and Characterization. Cuba: IntechOpen, 2015; p. 59-83.
43. Alexandre M, Bessaguet C, David C, et al. Piezoelectric properties of polymer/lead-free ceramic composites. Phase Transitions. 2016; 89(7-8):708-716.
44. Wang Y. Growth behavior and controllable morphologies of NaNbO3 superfine particles synthesized by hydrothermal method. Ceram. Int. 2018; 44(6): 7276-7279.
45. Wang S, Wu Z, Chen J, et al. Leadfree sodium niobate nanowires with strong piezo-catalysis for dye wastewater degradation. Ceram. Int. 2019; 45(9):11703-11708.
46. Pei L, Wang J, Chaoyang F, et al. The key role of photoisomerisation for the highly selective photocatalytic hydrogenation of azobenzene to hydrazobenzene over NaNbO3 fibre photocatalyst. J. Photochem. Photobiol. A. 2020; 400: 112655.
47. Gu Q, Zhu K, Liu J, et al. Rod-like NaNbO3: mechanisms for stable solvothermal synthesis, temperature-mediated phase transitions and morphological Evolution. RSC Adv. 2014; 4(29):15104-15110.

48. López-Juárez R, Castañeda-Guzmán R, Villafuerte-Castrejón ME. Fast synthesis of NaNbO3 and K0.5Na0.5NbO3 by microwave hydrothermal method. Ceram. Int. 2014; 40(9):14757-14764.
49. Jiang X, Wang Y, Herricks T, et al. Ethylene glycol-mediated synthesis of metal oxide nanowires. J. Mater. Chem. 2004; 14(4):695-703.
50. Xu Y-Q, Wu S-Y, Wu L-N, et al. Structural, elastic, electronic and optical properties of Cubic NaNbO3 crystals under pressure. Int. J. Mod. Phys. B. 2018; 32(25):1850282.
51. Fritsch D. Electronic and Optical Properties of Sodium Niobate: A Density Functional Theory Study. Adv. Mater. Sci. Eng. 2018; 2018: ID6416057.
52. Xu Y-Q, Wu S-Y, Wu L-N, et al. First-principles investigations on the visible light photocatalytic activity of NaNbO3 by N and F doping. Eur. Phys. J. B. 2019; 92:68.
53. Wood DL, Tauc J. Weak Absorption Tails in Amorphous Semiconductors, Phys. Ver. B. 1972; 5:3144-3151.
54. Pan H, Wang B, Zhang F, et al. Preparation and Physical and Photocatalytic Activity of a New Niobate Oxide Material Containing NbO4 Tetrahedra. Int. J. Photoenergy. 2018; 2018:ID 8516356.
55. Raubach CW, Gouveia AF, Santana YVB, et al. Towards controlled synthesis and better understanding of blue shift of the CaS crystals. J. Mater. Chem. C. 2014; 2(15):2743-2750.
56. Ücker CL, Gularte LT, Fernandes CD, et al. Investigation of the properties of niobium pentoxide for use in dye-sensitized solar cells. J. Am. Ceram. Soc. 2019; 102(4):1884-1892.
57. Teixeira GF, Junior ES, Simoes AZ, et al. Unveiling the correlation between structural order-disorder character and photoluminescence emissions of NaNbO3. Cryst. Eng. Comm. 2017; 19(30):4378-4392.
58. Ücker CL, Riemke FC, Andrade Neto NF, et al. Influence of Nb2O5 crystal structure on photocatalytic efficiency. Chem. Phys. Lett. 2021; 764:138271.
59. Morais LA, Adán C, Araujo AS, et al. Synthesis, Characterization, and Photonic Effciency of Novel Photocatalytic Niobium Oxide Materials, Global Challenges. 2017; 1(9):1700066.

Supplementary Material for

Fast synthesis of $NaNbO_3$ nanoparticles with high photocatalytic activity for degradation of organic dyes

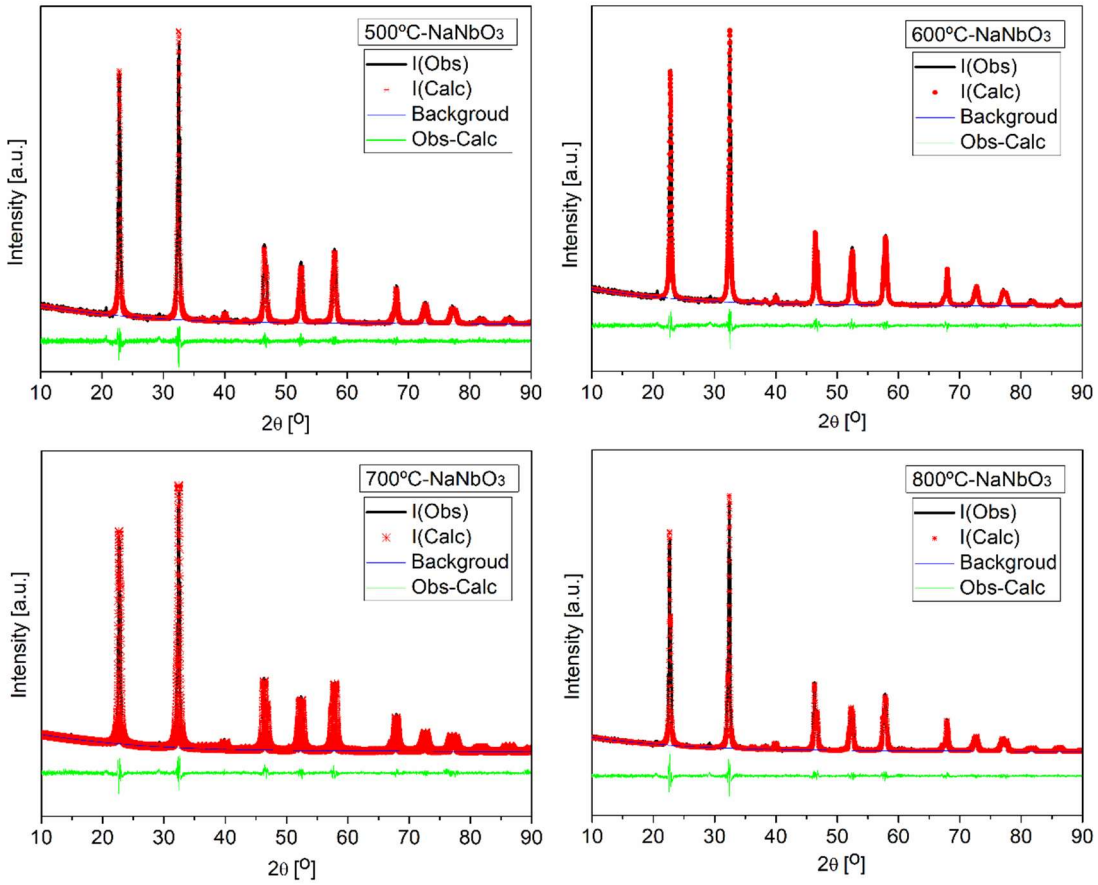

Figure S1: Rietveld refinement.

Table S1: Atomic sites.

$NaNbO_3$ – 500 ºC				$NaNbO_3$ – 600 ºC			
Atoms	**x**	**y**	**z**	**Atoms**	**x**	**y**	**z**
Nb1	0.2507	0.2440	0.2303	Nb1	0.2507	0.2440	0.2303
Na1	0.0000	0.7292	0.2566	Na1	0.0000	0.7346	0.2394
Na2	0.5000	0.2595	0.7259	Na2	0.5000	0.2609	0.7235
O1	0.0000	0.3183	0.2621	O1	0.0000	0.3071	0.2402
O2	0.5000	0.1961	0.2477	O2	0.5000	0.1971	0.2646
O3	0.2775	0.5331	0.4883	O3	0.2740	0.5300	0.4865
O4	0.2221	0.0474	0.5497	O4	0.2142	0.0467	0.5536
$NaNbO_3$ – 700 ºC				$NaNbO_3$ – 800 ºC			
Atoms	**x**	**y**	**z**	**Atoms**	**x**	**y**	**z**
Nb1	0.2528	0.2453	0.2303	Nb1	0.2489	0.2440	0.2300
Na1	0.0000	0.7304	0.2399	Na1	0.0000	0.7313	0.2461
Na2	0.5000	0.2550	0.7347	Na2	0.5000	0.2604	0.7223
O1	0.0000	0.3093	0.2509	O1	0.0000	0.3091	0.2189
O2	0.5000	0.1883	0.2695	O2	0.5000	0.1847	0.2662
O3	0.2756	0.5360	0.4774	O3	0.2747	0.5339	0.4796
O4	0.2153	0.0382	0.5496	O4	0.2156	0.0384	0.5520

Table S1: Crystal structure.

Sample	**Lattice Parameters**			**χ^2**	**RBragg**
	a	**b**	**c**		
500 ºC	7.78	5.52	5.56	1.16	0.03
600 ºC	7.78	5.52	5.56	1.18	0.05
700 ºC	7.77	5.52	5.56	1.31	0.05
800 ºC	7.77	5.52	5.56	1.40	0.03

3.2 Artigo 2

O artigo intitulado *"$NaNbO_3$/Eumelanin composite: A new photocatalyst under visible light"* é apresentado conforme publicado no periódico *Ceramics International (Online* ISSN:1873-3956 *and Print* ISSN:0272-8842), classificação A1 na área de Materiais.

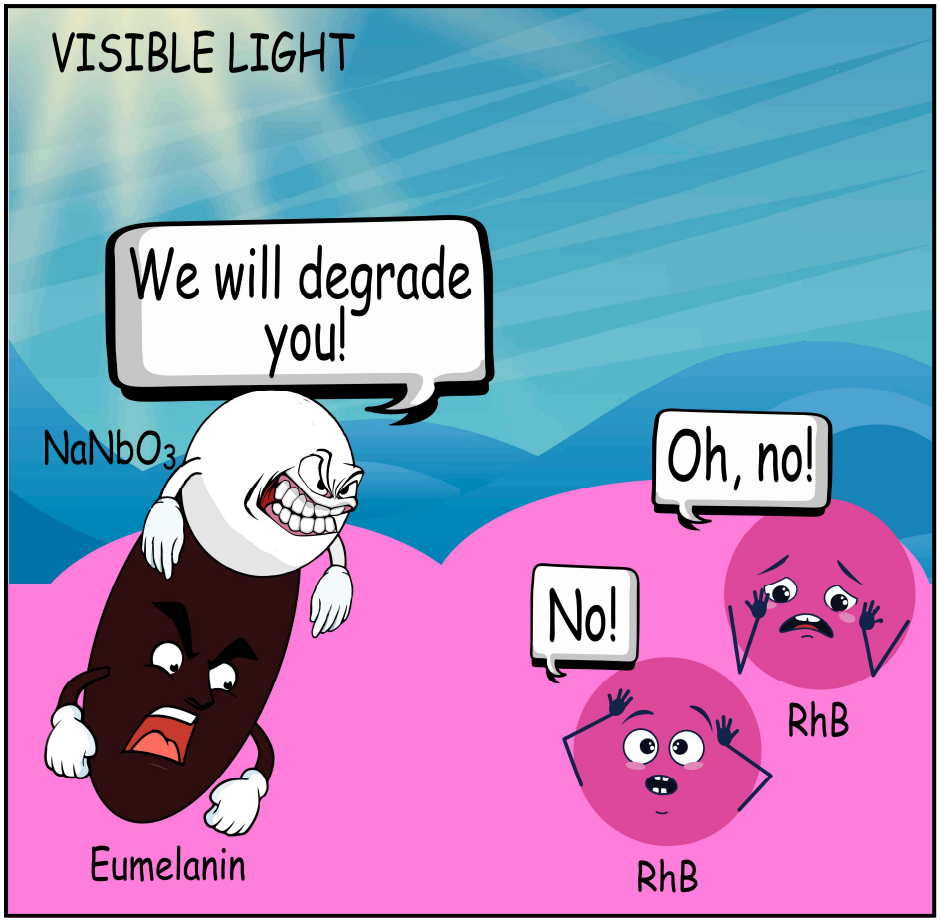

Figura 11 - Resumo gráfico Artigo 2.

Fonte: Elaborado pela autora, 2022.

$NaNbO_3$/Eumelanin composite: a new photocatalyst under visible light

Daiane Fernandes[a,*], Cristiane W. Raubach[a], Mateus M. Ferrer[a], Pedro L. G. Jardim[a,b], Carlos Frederico de O. Graeff[c,d], Mario L. Moreira[a,b], Eduardo C. Moreira[e], Valmor R. Mastelaro[f], Sergio da S. Cava[a,b]

[a]Post-Graduate Program in Materials Science and Engineering, Federal University of Pelotas, 96010-610, Pelotas, RS, Brazil

[b]Post-Graduate Program in Physics, Federal University of Pelotas, 96160-000, Capão do Leão, RS, Brazil

[c]Post-Graduate Program in Materials Science and Technology, São Paulo State University, 17033-360, Bauru, SP, Brazil

[d]Department of Physics, São Paulo State University, 17033-360, Bauru, SP, Brazil

[e]Spectroscopy Laboratory, Federal University of Pampa, 96413-172, Bagé, RS, Brazil

[f]Physics Institute, São Paulo University, 13560-970, São Carlos, SP, Brazil

*Corresponding author: daiane.fg.eng@outlook.com

A B S T R A C T

Sodium niobate ($NaNbO_3$) is a semiconductor with many potential technological applications and, among them, it is considered a promising photocatalyst. However, it only absorbs ultraviolet light, limiting its use in light-dependent processes. Therefore, in this work we synthesized $NaNbO_3$ nanoparticles quickly and used them to prepare a $NaNbO_3$/Eumelanin composite with photocatalytic activity under visible light. Eumelanin was extracted from human hair and is a pigment responsible for the brown-black coloration, abundant in fauna and flora. The results showed that the composite successfully degraded the Rhodamine B dye. Therefore, this study presents a photocatalyst solution with better use of light and serves as inspiration for the development of new photocatalysts.

Keywords: sodium niobate; eumelanin; photocatalysis; visible light.

1. Introduction

Sodium niobate ($NaNbO_3$) is a semiconductor with many potential technological applications and, among them, photocatalysis [1-13]. It is considered a promising photocatalyst since it is thermodynamically stable, corrosion resistant and non-toxic [3,7]. However, the natural shape of its particle is cubic with low with low photocatalytic activity, but researchers have demonstrated that it is possible to obtain nanowires with high photocatalytic activity [5,12,13]. Another shape particle in nanoscale was presented by Farooq et. al. [11] through the method polymeric citrate precursors for 22 h and calcination for 12 h, with high photocatalytic activity. In addition, it only absorbs ultraviolet light, limiting its use. Thus, to make the most of solar radiation, also promoting efficiency in the separation of photoinduced charges, $NaNbO_3$ was combined with other materials, forming heterostructured photocatalysts. The literature has shown great advances in photocatalytic processes using the strategy of building heterostructures [14-18]. Materials such as Cu_2O, Cu, Au, BiOI, Ag_2O, Ag_2SO_3, and Bi_2WO_6 were combined with $NaNbO_3$ for this purpose. [19-25]. Nevertheless, the use of these metals ends up not being economically favorable.

Eumelanin is a pigment present in abundance in fauna and flora, responsible for the black-brown color. It is composed of disordered heteroaromatic networks based on 5,6-dihydroxyindole (DHI) and 5,6- dihydroxyindole carboxylic acid (DHICA) building blocks, which are catechol-derivatives [26-28]. It has many physicochemical properties, of particular interest here is a wide optical absorption ranging from UV to near-infrared (NIR), redox activity and metal-chelating capability [28-30]. Eumelanin and a similar polymer polydopamine (PDA) have been considered in different application [31-38]. In photocatalytic applications, composites with TiO_2, Cds, CuO_2, BiOBr, and MIL-53(Fe) were reported [28,39-50].

Considering the above, we present a rapid method to synthesize $NaNbO_3$ nanoparticles similar to nanograins. These nanoparticles were used to prepare for the first time a $NaNbO_3$/Eumelanin composite with photocatalytic activity under visible light. The photocatalytic activity was analyzed through the degradation of Rhodamine B (RhB), a dye widely used in industry and highly toxic [51].

2. Experimental

2.1. $NaNbO_3$ synthesis

An aqueous solution of NaOH (Merck, 99.0%) and $NbCl_5$ (CBMM, 99.0%) with concentrations of 6 M and 0.6 M, respectively, was taken to an adapted microwave oven (800 W, PANASONIC) for 15 min at 180 ºC. The obtained precipitate was washed and centrifuged until the pH was neutralized and then dried in an oven. Finally, the powder was submitted to thermal treatment at 800 ºC for 2 h and naturally cooled.

2.2. Eumelanin extraction

Eumelanin was extracted from dark brown human hair using the acid isolation method [33]. 2 g of clean hair was immersed in HCl (37%, 70 mL) at 100 °C for 3 h. Finally, the Eumelanin was collected by centrifugation and washed until solution had a neutral pH and then dried in an oven.

2.3. Preparation of $NaNbO_3$/Eumelanin composite

The composite was prepared according to the method reported by Xie. et. al. [35]. A solution of 50 ml of ethanol, 4 mg of Eumelanin and 16 mg of $NaNbO_3$ was sonicated for 30 min and stirred for 5 h at room temperature. The homogeneous suspension was dried in an oven.

2.4. Sample characterization

X-ray diffraction was performed in a diffractometer (Ultima IV, RIGAKU) with Cu-Kα radiation (λ=1.5406 Å), scanning of 10°/min. Raman spectroscopy were done using a micro-positioning system (B&WTek, RAMAN PROBE) and monochromator (Shamrock 303i, ANDOR) with 532 nm excitation. High resolution images were taken using Scanning Electron Microscope, (JSM7500F, JEOL). Optical absorption spectra were obtained using a UV-Vis-NIR spectrometer (Lambda 1050, PERKIN ELMER). The valence band top potential was estimated by X-ray photoelectron spectroscopy (XPS) using a spectrometer (ESCA+, SCIENTIA OMICRON) with a high-performance hemispherical analyzer (EAC2000) and monochromatic Al-Kα radiation (hv=1486.6 eV). In addition, we evaluated the photoluminescence and textural properties of samples (supplementary data file).

2.5. Photocatalytic activity

The photocatalytic activity was evaluated under visible irradiation, using a 100 W LED (MEGAACE, 400 nm < λ < 800 nm, int. máx at 458 and 538 nm). The photocatalytic reaction was carried out with 10 mg of the photocatalyst dispersed in 50 mL of RhB solution (5 $mg.L^{-1}$), under magnetic stirring at room temperature, which was first stirred for 1 h in the dark. The variation in RhB concentration was recorded by absorbance, using a UV-Vis spectrophotometer (SP200 UV, BEL PHOTONICS).

3. Results and discussion

Fig. 1a show the XRD of $NaNbO_3$ sample. The peaks shown in the diffractogram are characteristic of the orthorhombic phase, space group P21ma (JCPDS card files, 82-606). In addition, the mean value of the crystallographic domains was estimated by the Scherrer equation, resulting 27.43 nm. The $NaNbO_3$ obtained presents particle shape similar to nanograins, with an average size of ~28 nm (Fig. 1b).

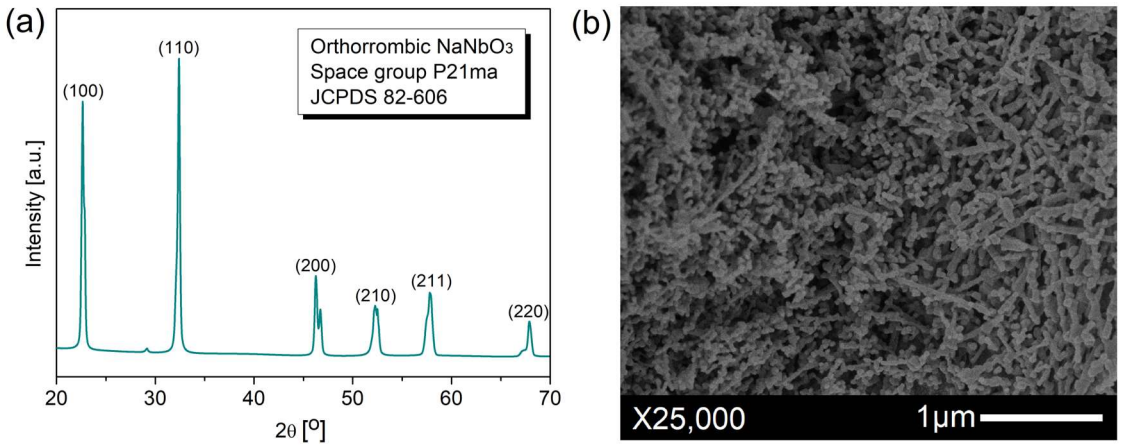

Figure 1. (a) XRD of the $NaNbO_3$ and (b) SEM of the $NaNbO_3$.

Fig. 2a shows the Raman spectrum of the extracted Eumelanin. It is possible to observe two bands around 1358 and 1588 cm^{-1}, which are characteristic of disordered graphitic materials, the D and G bands, [35,52]. Studies indicate that melanin has a graphene sheet-like structure with high-density of vacancy defects [52]. Through deconvolution, using the Gaussian function, four vibrational modes are also observed assigned to their functional groups. The band at ~1344 cm^{-1} corresponds

to the C−OH phenolic stretching (DHI/DHICA) and C−O stretching of the carboxylic acid, the band at ~1484 cm^{-1} is attributed to the C−N group in the IQ, band at ~1574 cm^{-1} is attributed to the C=N stretching (in SQ) or the N−H bending vibration (in IQ) and the band at ~1600 cm^{-1} corresponds to aromatic C=C bond in the indole structure [35,53]. Fig. 2b shows the basic units of Eumelanin DHI and DHICA and their redox forms (5,6-indolequinone (IQ) and semiquinone (SQ)) [35,53]. The extracted Eumelanin presents ellipsoidal shaped particles, with principal axis of ~400 nm and ~1 μm (Fig. 2c), in good agreement with literature [35,54,55].

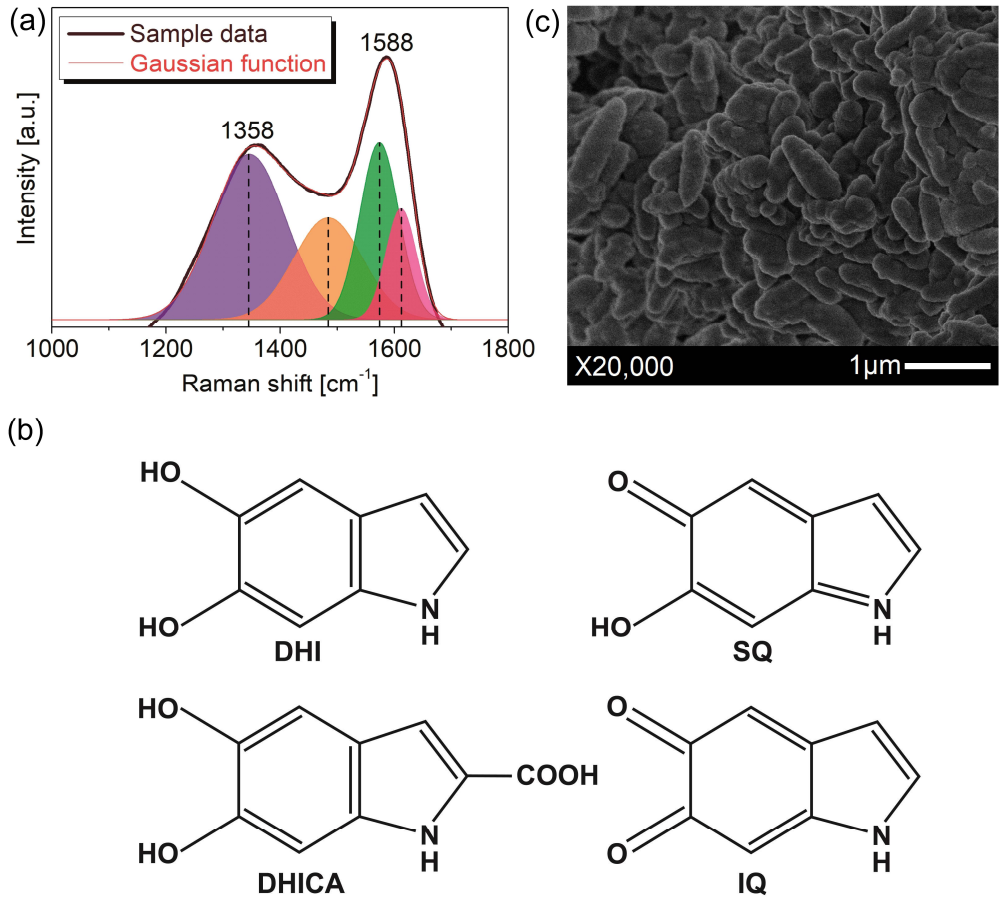

Figure 2. (a) Raman spectra of the Eumelanin, (b) DHI, DHICA, SQ and IQ structures, and (c) SEM of the Eumelanin.

Fig. 3a shows the optical absorbance spectra of the samples. $NaNbO_3$ shows intense absorption in the UV region only and Eumelanin has a broadband absorption spectrum, due to the overlap of a range of absorption peaks of the DHI and DHICA

oligomers [56,57]. In Eumelanin, the electronic states do not have a definite low-energy edge for optical absorption, but tail states [30,56]. Its band gap is associated with the transitions π-π* between molecular orbitals in HOMO (highest occupied molecular orbital) and LUMO (lowest unoccupied molecular orbital) [39,45,56]. The composite maintains the broadband absorption of Eumelanin (Fig. 3a), a little reduced due to $NaNbO_3$ nanoparticles that decorate its surface (Fig. 3b), by Van der Waals interactions, which is possible due to its strong affinity for metallic cations.

The photocatalytic activity of the samples was evaluated through the photo-induced degradation of RhB, where C_0 and C indicate the initial concentration and concentration at a specific time (h), respectively (Fig. 3c). It is observed that only the $NaNbO_3$/Eumelanin composite showed photocatalytic activity, inducing ~96% of dye degradation in 5 h. Although Eumelanin presents high absorption in the visible range, its photocatalytic activity is unsatisfactory. This is because the π-system allows for high mobility of charge carriers, which can easily recombine. To better understand the dye degradation mechanism, experiments to identify the active species were performed. For this, isopropyl alcohol (C_3H_8O), silver nitrate ($AgNO_3$), and disodium ethylenediaminetetraacetate (EDTA) were used as scavengers for hydroxyl radicals (·OH), electrons (e^-), and holes (h^+), respectively. Fig. 3d shows the percentual of RhB degradation with the presence of scavengers at the end of 5 h. It is observed that the addition of EDTA and C_3H_8O inhibited the degradation of the dye, indicating that the main active species during the photocatalysis process are h^+ and ·OH. In contrast, the addition of $AgNO_3$ no change in the percentual, indicating that the e^- are not active species. In addition, a reuse test was carried out. After three successive cycles, the composite maintained the same photocatalytic efficiency, demonstrating that it can be considered a stable photocatalyst.

Based on the results, a possible mechanism is proposed (Fig. 3b). Under visible light irradiation, only the electrons of Eumelanin are excited, from HOMO to LUMO, forming an electron/hole pair (e^-/h^+). The electrons in LUMO are injected into the CB, due to the potential difference. The electrons in the CB can react with oxygen (O_2) to produce superoxide radical ($•O_2^-$), that can react with water (H_2O) to produce •OH. Meanwhile, h^+ in LUMO can react with H_2O or hydroxyl anion ($•OH^-$) to generate •OH and also directly oxidize the RhB dye. With this, an efficient separation of charge and a slower recombination are achieved, resulting in a significant increase in

photocatalytic activity. This agrees with the results obtained in the experiment of active species (Fig. 3d) and also with the photoluminescence analysis (Fig. S1).

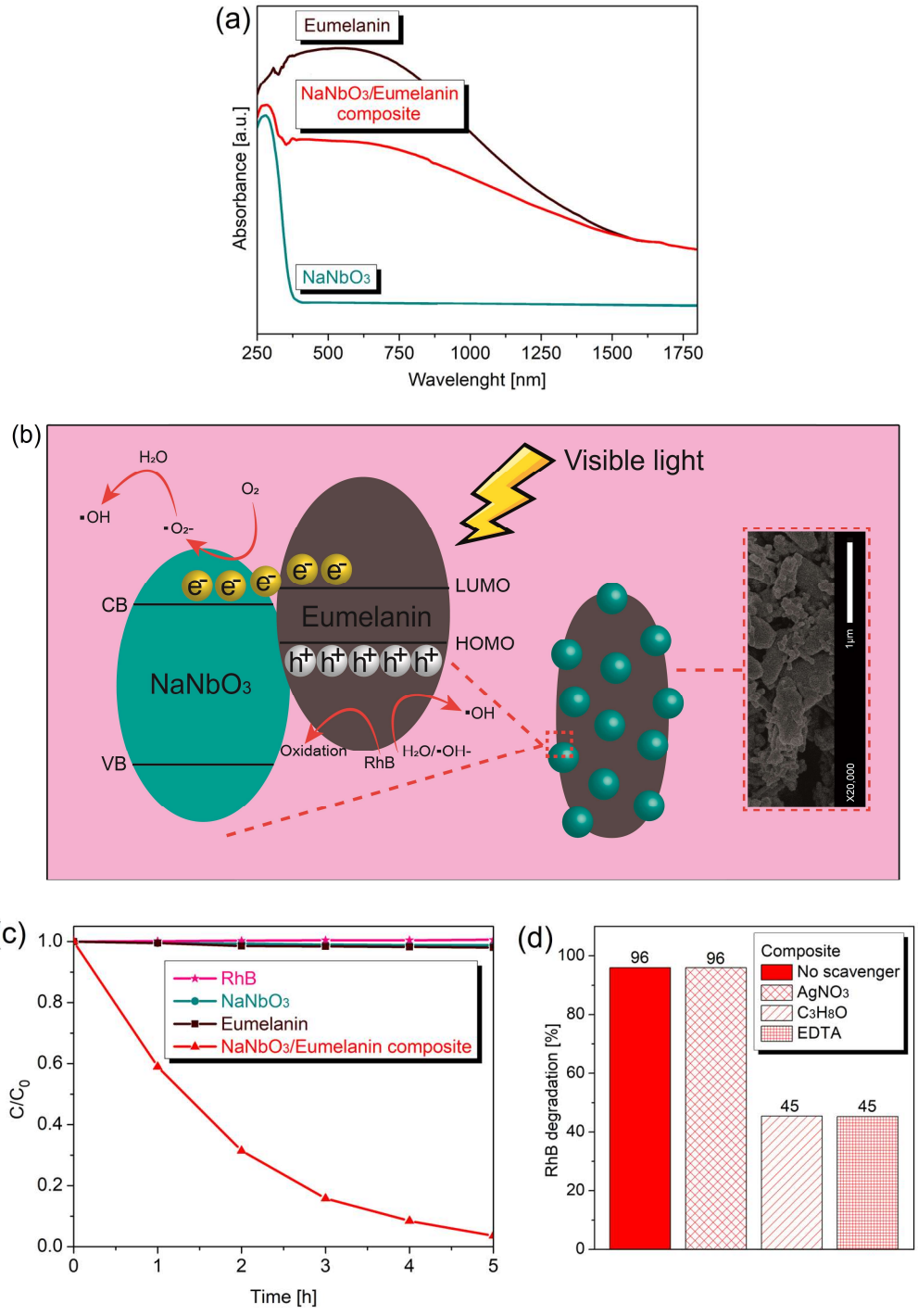

Figure 3. (a) Optical absorbance spectra of the samples, (b) Schematic illustration of the possible mechanism for photodegradation of the RhB, under visible light and SEM-FEG of the $NaNbO_3$/Eumelanin composite, (c) Photocatalytic degradation of the RhB under visible light irradiation, and (d) Percentage of RhB degradation using scavengers.

Potentials of edge of $NaNbO_3$ were determined by the equation $E_{cb}= E_{vb} – E_g$, where E_{cb} is potential of the bottom of the CB, E_{vb} is the potential at the top of the VB and E_g is the band gap energy. According to XPS, E_{vb} is +2.40 eV (Fig. 4a). The band gap was estimated in 3.60 eV (Fig. 4b), by the Wood/Tauc method [58], resulting in -1.20 eV the E_{cb}. The direct location of the HOMO and LUMO of the natural Eumelanin is very difficult to determine due to its structural and energetic disorder. Because of this, researches asume that it is close to that of PDA [59]. The LUMO of the PDA is estimated at -1.4 eV [42,48,60]. Thus, the LUMO of Eumelanin is more electronegative than the CB of $NaNbO_3$ making it possible to transfer charges in the $NaNbO_3$/Eumelanin composite, as proposed in the Fig. 3b.

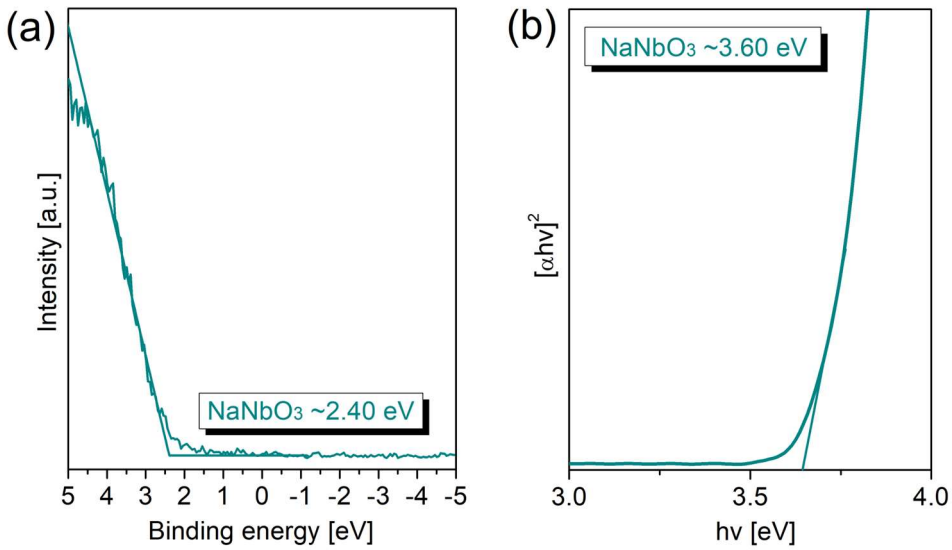

Figure 4. (a) Valence-band XPS spectra of the $NaNbO_3$ and (b) Band gap of the $NaNbO_3$.

4. Conclusions

In this work, $NaNbO_3$ nanograins were obtained by microwave-assisted hydrothermal method followed by heat treatment. The nanoparticles were used to prepare a $NaNbO_3$/Eumelanin composite with photocatalytic activity under visible light. The results showed that pure $NaNbO_3$ and pure Eumelanin do not show photocatalytic activity, while the composite was able to successfully degrade the RhB dye. The heterostructure promoted efficient separation of photogenerated charges

and slower recombination, resulting in a significant increase in photocatalytic activity. Therefore, this study presents an alternative photocatalyst that uses visible light and widely available elements, serving as inspiration for the development of new photocatalysts.

Acknowledgments

The authors thank Companhia Brasileira de Metalurgia e Mineração (CBMM) for donating the niobium precursor, Núcleo de Apoio à Pesquisa em Ciência e Engenharia de Materiais (NAPCEM-UNIFESP Campus São José dos Campos) for XRD analysis, Centro Integrado de Análises (CIA FURG) for BET analysis and to colleagues Paola Gay, Thissiana Fernandes, Lucas Affonço, Ramon Dadalto, Caroline Schmechel and Lucas Barcellos for supporting. This research received support from Coordenação de Aperfeiçoamento de Pessoal de Nível Superior (CAPES), Conselho Nacional de Desenvolvimento Científico e Tecnológico (CNPq) and Fundação de Amparo à Pesquisa do Estado do Rio Grande do Sul (FAPERGS) (17/25510000889-8).

References

[1] D. Fernandes, M. M. Ferrer, C. W. Raubach, M. L. Moreira, P. L. G. Jardim, E. C. Moreira, C. F. O. Graeff, S. S. Cava, Fast synthesis of NaNbO3 nanoparticles with high photocatalytic activity for degradation of organic dyes, J. Am. Ceram. Soc. 106 (2023) 399-409. https://doi.org/10.1111/jace.18740.

[2] H. Shi, T. Wang, J. Chen, C. Zhu, J. Ye, Z. Zou, Photoreduction of Carbon Dioxide Over NaNbO3 Nanostructured Photocatalysts, Catal. Lett. 141 (2011) 525-530. https://doi.org/ 10.1007/s10562-010-0482-1.

[3] P. Li, S. Ouyang, G. Xi, T. Kako, J. Ye, The effects of crystal structure and electronic structure on photocatalytic H2 evolution and CO2 reduction over two phases of perovskite-structured NaNbO3, J. Phys. Chem. C 116 (2012) 7621-7628. https://doi.org/10.1021/jp210106b.

[4] G. Li, Z. Yi, Y. Bai, W. Zhang, H. Zhang, Anisotropy in photocatalytic oxidization activity of NaNbO3 photocatalyst, Dalton Trans. 41 (2012) 10194. https://doi.org/10.1039/c2dt30593c.

[5] Q. Liu, L. Zhang, Y. Chai, W.-L. Dai, Facile fabrication and mechanism of single-crystal sodium niobate photocatalyst: insight into the structure features influence on photocatalytic performance for H2 evolution, J. Phys. Chem. C 121 (2017) 25898-25907. https://doi.org/10.1021/acs.jpcc.7b08819.

[6] F. Fresno, P. Jana, P. Reñones, J. M. Coronado, D. P. Serrano, V. A. O'shea, CO2 reduction over NaNbO3 and NaTaO3 perovskite photocatalysts, Photochem. Photobiol. Sci. 16 (2017) 17-23. https://doi.org/10.1039/C6PP00235H.

[7] T. Ahmad, U. Farooq, R. Phul, Fabrication and Photocatalytic Applications of Perovskite Materials with Special Emphasis on Alkali Metal based Niobates and Tantalates, Ind. Eng. Chem. Res. 52 (2018) 18–4. https://doi.org/10.1021/acs.iecr.7b04641.

[8] M. Nawaz, S. A. Almofty, F. Qureshi, 2018. Preparation, formation mechanism, photocatalytic, cytotoxicity and antioxidant activity of sodium niobate nanocubes. Plos One. 13, e0204061. https://doi.org/10.1371/journal.pone.0204061.

[9] N. Duc Van, Template-free synthesis and photocatalytic activity of {001}-facets exposed rhombohedral NaNbO3 microcrystals, Ceram. Int. 44 (2018) 19945-19949. https://doi.org/10.1016/j.ceramint.2018.07.260.

[10] A. Hamilton, S. O'donnell, B. Zoellner, I. Sullivan, P. Maggard, Flux-mediated synthesis and photocatalytic activity of NaNbO3 particles, J. Am. Ceram. Soc. 103 (2019) 454-464. https://doi.org/10.1111/jace.16765.

[11] U. Farooq, R. Phul, S. Alshehri, J. Ahmed, T. Ahmad, 2019. Electrocatalytic and enhanced photocatalytic applications of sodium niobate nanoparticles developed by citrate precursor route. Sci. Rep. 9, 4488. https://doi.org/10.1038/s41598-019-40745-w.

[12] C. Yan, B. Li, J. Wang, A Comparative Study of Photodegradation Behavior Sodium Niobate Nanowires and Microcubes, Key Eng. Mater. 861 (2020) 221-227. https://doi.org/10.4028/www.scientific.net/KEM.861.221.

[13] D. Fernandes, C. W. Raubach, P. L. G. Jardim, M. L. Moreira, S. S. Cava, Synthesis of NaNbO3 nanowires and their photocatalytic activity, Ceram. Int. 47 (2021) 10185-10188. https://doi.org/10.1016/j.ceramint.2020.12.070.

[14] M. F. Warsi, B. Bashir, S. Zulfqar, M. Aadil, M. U. Khalid, P. O. Agboola, I. Shakir, M. A. Yousuf, M. Shahid, $Mn_{1-x}Cu_xO_2$/ reduced graphene oxide nanocomposites:

Synthesis, characterization, and evaluation of visible light mediated catalytic studies, Ceram. Int. 47 (2021) 5044-5053. https://doi.org/10.1016/j.ceramint.2020.10.082.
[15] B. Bashir, M. U. Khalid, M. Aadil, S. Zulfqar, M. F. Warsi, P. O. Agboola, I. Shakir, $Cu_xNi_{1-x}O$ nanostructures and their nanocomposites with reduced graphene oxide: Synthesis, characterization, and photocatalytic applications, Ceram. Int. 47 (2021) 3603-3613. https://doi.org/10.1016/j.ceramint.2020.09.209.
[16] S. Bashir, A. Habib, A. Jamil, A. Alazmi, M. Shahid, 2022. Fabrication of Ag-doped MoO_3 and its nanohybrid with a two-dimensional carbonaceous material to enhance photocatalytic activity. Adv. Powder Technol. 33, 103482. https://doi.org/10.1016/j.apt.2022.103482.
[17] S. Bashir, A. Jamil, M. S. Khan, A. Alazmi, F. A. Abuilaiwi, M. Shahid, 2022. Gd-doped $BiVO_4$ microstructure and its composite with a flat carbonaceous matrix to boost photocatalytic performance. J. Alloys Compd. 913, 165214. https://doi.org/10.1016/j.jallcom.2022.165214.
[18] M. Aadil, M. Mahmood, M. F. Warsi, I. A. Alsafari, S. Zulfqar, M. Shahid, 2021. Fabrication of MnO_2 nanowires and their nanohybrid with flat conductive matrix for the treatment of industrial effluents. FlatChem. 30, 100316. https://doi.org/10.1016/j.flatc.2021.100316.
[19] M. Fan, B. Hu, X.Yan, C. Song, T. Chen, Y. Feng, W. Shi, Excellent Visible-Light-Driven Photocatalytic Performance of Cu2O Sensitized NaNbO3 Heterostructure, New J Chem. 39 (2015) 6171-6177. https://doi.org/10.1039/C5NJ00751H.
[20] J. Xu, F. Zhang, B. Sun, Y. Du, G. Li, W. Zhang, 2015. Enhanced Photocatalytic Property of Cu Doped Sodium Niobate. Int J Photoenergy. 2015, ID 846121. http://dx.doi.org/10.1155/2015/846121.
[21] E.S. Baeissa, Photocatalytic degradation of malachite green dye using Au/ NaNbO3 nanoparticles, Journal of Alloys and Compounds. 672 (2016) 564-570. https://doi.org/10.1016/j.jallcom.2016.02.024.
[22] M. Sun, Q. Yan, Y. Shao, C. Wang, T. Yan, P. Ji, B. Du, Facile fabrication of BiOI decorated NaNbO3 cubes: A p-n junction photocatalyst with improved visible-light activity, Appl. Surf. Sci. 416 (2017) 288-295. http://dx.doi.org/10.1016/j.apsusc.2017.04.136.
[23] B. Zhang, D. Zhang, Z. Xi, P. Wang, X. Pu, X. Shao, S. Yao, Synthesis of Ag2O/NaNbO3 p-n junction photocatalysts with improved visible light photocatalytic

activities, Sep Purif Technol. 178 (2017) 130-137. http://dx.doi.org/10.1016/j.seppur.2017.01.031.
[24] Y. Feng, Z. Wang, Y. Yang, X. Wu, X. Gon, Y. Liu, Y. Li, Z. Cao, C. Wang, X. Tong, 2018. Chemical Bonds-Conjugated Ag2SO3/NaNbO3 Hybrids as E±cient Photocatalysts: In-situ Fabrication, Characterization and Degradation of Rhodamine B and Methyl Orange. Nano. 13, 1850076. https://doi.org/10.1142/S1793292018500765.
[25] Y. Qiao, X. Meng, Z. Zhang, A new insight into the enhanced visible light-induced photocatalytic activity of NaNbO3/Bi2WO6 type-II heterostructure photocatalyst, Appl. Surf. Sci. 470 (2019) 645-657. https://doi.org/10.1016/j.apsusc.2018.11.048.
[26] Y. J. Kim, W. Wu, S.E. Chun, J.F. Whitacre, C.J. Bettinger, Catechol-mediated reversible binding of multivalent cations in eumelanin half-cells, Adv. Mater. 26 (2014) 6572-6579. https://doi.org/10.1002/adma.201402295.
[27] C. T. Chen, F.J. Martin-Martinez, G.S. Jung, M.J. Buehler, Polydopamine and eumelanin molecular structures investigated with ab initio calculations, Chem. Sci. 8 (2017) 1631-1641. https://doi.org/10.1039/C6SC04692D.
[28] W. Xie, E. Pakdel, Y. Liang, D. Liu, L. Sun, X. Wang, Natural melanin/TiO2 hybrids for simultaneous removal of dyes and heavy metal ions under visible light, 2020. J. Photochem. Photobiol. A. 389, 112292. https://doi.org/10.1016/j.jphotochem.2019.112292.
[29] Y. Liu, J. D. Simon, Metal-ion Interactions and the Structural Organization of Sepia Eumelanin, Pigm. Cell Res. 18 (2005) 42-48. https://doi.org/10.1111/j.1600-0749.2004.00197.x.
[30] P. Meredith, K. Tandy, A. B. Mostert, A Hybrid Ionic–Electronic Conductor: Melanin, the First Organic Amorphous Semiconductor?, in: F. Cicoira, C. Santato (Eds.), Organic Eletronics, Wiley-VCH Verlag GmbH & Co. KGaA, Weinheim, 2013, pp. 91-111.
[31] P. Kumar, E. D. Mauro, S. Zhang, A. Pezzella, F. Soavi, C. Santato, F. Cicoira, Melanin-based flexible supercapacitors, J. Mater. Chem. C. 4 (2016) 9516-9525. https://doi.org/10.1039/C6TC03739A.
[32] L. G. S. Albano, J. V. Paulin, L. D. Trino, S. L. Fernandes, C. F. O. Graeff, 2019. Ultraviolet-protective thin film based on PVA–melanin/rod-coated silver nanowires

and its application as a transparent capacitor. J. Appl. Polym. Sci. 136, 47805. https://doi.org/10.1002/app.47805.

[33] Y. Liang, W. Xie, E. Pakdel, M. Zhang, L. Sun, X. Wang, Homogeneous melanin/silica core-shell particles incorporated in poly (methyl methacrylate) for enhanced UV protection, thermal stability, and mechanical properties, Mater Chem Phys. 230 (2019) 319-325. https://doi.org/10.1016/j.matchemphys.2019.03.081.

[34] W. Xie, E. Pakdel, Y. Liang, Y. J. Kim, D. Liu, L. Sun, X. Wang, Natural Eumelanin and Its Derivatives as Multifunctional Materials for Bioinspired Applications: A Review, Biomacrom. 20 (2019) 4312-4331. https://doi.org/10.1021/acs.biomac.9b01413.

[35] W. Xie, E. Pakdel, D.Liu, L. Sun, X. Wang, Waste-Hair-Derived Natural Melanin/TiO2 Hybrids as Highly Efficient and Stable UV-Shielding Fillers for Polyurethane Films, ACS Sustainable Chem. Eng. 8 (2020) 1343-1352. https://doi.org/10.1021/acssuschemeng.9b03514.

[36] J. V. Paulin, A. P. Coleone, A. Batagin-Neto, G. Burwell, P. Meredith, C. F. O. Graeff, A. B. Moster, Melanin thin-films: a perspective on optical and electrical properties, J. Mater. Chem. C. 9 (2021) 8345-8358. https://doi.org/10.1039/d1tc01440d.

[37] J. V. Paulin, S.L. Fernandes, C. F. O. Graeff, Solid-State Electrochemical Energy Storage Based on Soluble Melanin, Electrochem. 2 (2021) 264-273. https://doi.org/10.3390/electrochem2020019.

[38] J. Lu, J. Fang, Ji. Li, L. Zhu, Engineering highly transparent UV-shielding flms with disassembled polydopamine oligomers as light adsorber, Appl. Surf. Sci. 550 (2021) 149284. https://doi.org/10.1016/j.apsusc.2021.149284.

[38] J. Lu, J. Fang, Ji. Li, L. Zhu, Engineering highly transparent UV-shielding flms with disassembled polydopamine oligomers as light adsorber, Appl. Surf. Sci. 550 (2021) 149284. https://doi.org/10.1016/j.apsusc.2021.149284.

[39] X. Zhou, B. Jin, J. Luo, X. Xu, L. Zhang, J. Li, H. Guan, Dramatic visible light photocatalytic degradation due to the synergetic effects of TiO2 and PDA nanospheres, RSC Adv. 6 (2016) 64446-64449. https://doi.org/10.1039/C6RA10292A.

[40] W.-X. Mao, X.-J. Lin, W. Zhang, Z.-X. Chi, R.-W. Lyu, A.-M. Cao, L.-J. Wan, Core-shell structured TiO2@polydopamine for highly active visible-

light photocatalysis, Chem. Commun. 52 (2016) 7122-7125. https://doi.org/10.1039/C6CC02041K.

[41] Z. Wang, J. Li, F. Tang, J. Lin, Z. Jin, Polydopamine nanotubes-templated synthesis of TiO2 and its photocatalytic performance under visible light, RSC Adv. 7 (2017) 23535-23542. https://doi.org/10.1039/C7RA03063K.

[42] X. Zhou, B. Jin, J.Luo, X. Gu, S. Zhang, Photoreduction preparation of Cu2O@polydopamine nanospheres with enhanced photocatalytic activity under visible light irradiation, J. Solid State Chem. 254 (2017) 55-61. http://dx.doi.org/10.1016/j.jssc.2017.07.007.

[43] D. Hao, Y. Yang, B. Xu, Z. Cai, Bifunctional Fabric with Photothermal Effect and Photocatalysis for Highly Efficient Clean Water Generation, ACS Sustainable Chem. Eng. 6 (2018) 10789-10797. https://doi.org/10.1021/acssuschemeng.8b02094.

[44] X. Hou, Y. Cai, X. Song, Y. Wu, J. Zhang, Q. Wei, Electrospun TiO2 nanofibers coated with polydopamine for enhanced sunlight-driven photocatalytic degradation of cationic dyes, Surf. Interface Anal. 51 (2019) 169-176. https://doi.org/10.1002/sia.6554.

[45] Y. Zou, Z. Wang, Z. Chen, Q.-P. Zhang, Q. Zhang, Y. Tian, S. Ren, Y. Li, Synthetic Melanin Hybrid Patchy Nanoparticle Photocatalysts, J. Phys. Chem. C. 123 (2019) 5345-5352. https://doi.org/10.1021/acs.jpcc.8b10469.

[46] M. Wang, Z. Cui, M. Yang, L. Lin, X. Chen, M. Wang, J. Han, Core/shell structured CdS/polydopamine/TiO2 ternary hybrids as highly active visible-light photocatalysis, J. Colloid. Interface Sci. 544 (2019) 1-7. https://doi.org/10.1016/j.jcis.2019.02.080.

[47] D. Yang, W. Wang, X. Zhao, Z. Zhou, H. Ren, Y. Chen, Z. Zhao, K. An, Z. Jiang, 2020. Synthesis of high-efficient g-C3N4/polydopamine/CdS nanophotocatalyst based on bioinspired adhesion and chelation, Mater. Res. Bull. 131, 110970. https://doi.org/10.1016/j.materresbull.2020.110970.

[48] J. Zhao, J. Chen, Z. Chen, Y. Zhang, D. Xia, Q. Wang, Flexible cotton fabrics/PDA/BiOBr composite photocatalyst using bioinspired polydopamine as electron transfer mediators for dye degradation and Cr(VI) reduction under visible light, 2020. Colloids Surf. A. 593, 124623. https://doi.org/10.1016/j.colsurfa.2020.124623.

[49] F. Chena, L. Zhaoa, W. Yua, Y. Wanga, H. Zhanga, L.-H. Guo, 2020. Dynamic monitoring and regulation of pentachlorophenol photodegradation process by chemiluminescence and TiO2/PDA. J. Hazard. Mater. 399, 123073. https://doi.org/10.1016/j.jhazmat.2020.123073.

[50] S. Menga, W. Zenga, M. Wanga, L. Niua, S. Hua, B. Sua, Y. Yanga, Z. Yanga, Q. Xue, Nature-Mimic Fabricated Polydopamine/MIL-53(Fe): Efficient Visible-light Responsive Photocatalysts for the Selective Oxidation of Alcohols, New J. Chem. 44 (2020) 2102-2110. https://doi.org/10.1039/C9NJ04929K.

[51] L. Carmine, A. Ancona, K. Di Cesare, B. Dumontel, N. Garino, G. Canavese, S. Hernandez, V. Cauda, Sonophotocatalytic degradation mechanisms of Rhodamine B dye via radicals generation by micro- and nano-particles of ZnO, Appl. Catal. B: Environ. 243 (2019) 629-640. https://doi.org/10.1016/j.apcatb.2018.10.078.

[52] Q. Jiang, Z. Luo, Y. Men, P. Yang, H. Peng, R. Guo, Y.Tian, Z. Pang, W. Yang, Red blood cell membrane-camouflaged melanin nanoparticles for enhanced photothermal therapy, Biomaterials. 143 (2017) 29-45. https://doi.org/10.1016/j.biomaterials.2017.07.02.

[53] V. Capozzi, G. Perna, A. Gallone, P.F. Biagi, P. Carmone, A. Fratello, G. Guida, P. Zanna, R. Cicero, Raman and optical spectroscopy of eumelanin films, J. Mol. Struct. 744 (2005) 717-721. https://doi.org/10.1016/j.molstruc.2004.11.074.

[54] Y. Liu, V. R. Kempf, J. B. Nofsinger, E. E. Weinert, M. Rudnicki, K. Wakamatsu, S. Ito, J. D. Simon, Comparison of the Structural and Physical Properties of Human Hair Eumelanin Following Enzymatic or Acid/Base Extraction, Pigment Cell. Res. 16 (2003) 355-365. http://dx.doi.org/10.1034/j.1600-0749.2003.00059.x.

[55] Y. Liu, L. Hong, K. Wakamatsu, S. Ito, B. Adhyaru, C.-Y. Cheng, C. R. Bowers, J. D. Simon, Comparison of Structural and Chemical Properties of Black and Red Human Hair Melanosomes, Photochem. Photobiol. 81 (2005) 135-144. http://dx.doi.org/10.1562/2004-08-03-RA-259.1.

[56] V. Capozzi, G. Perna, P. Carmone, A. Gallone, M. Lastella, E. Mezzenga, G. Quartucci, M. Ambrico, V. Augelli, P.F. Biagi, T. Ligonzo, A. Minafra, L. Schiavulli, M. Pallara, R. Cicero, Optical and photoelectronic properties of melanin, Thin Solid Films. 511 (2006) 362-366. https://doi.org/10.1016/j.tsf.2005.12.065.

[57] P. Meredith, B. J. Powell, J. Riesz, S. P. N.-R., M. R. Pedersonc, E. G. Moore, Towards structure–property–function relationships for eumelanin, Soft Matter. 2 (2006) 37-44. https://doi.org/10.1039/b511922g.
[58] D. L. Wood, J. Tauc, Weak Absorption Tails in Amorphous Semiconductors, Phys. Ver. B. 5 (1972) 3144-3151. https://doi.org/10.1103/PhysRevB.5.3144.
[59] D. Niyonkuru, A. Carrière, R. Ambrose, A. Gouda, M. Reali, A. Camus, A. Pezzella, I. Hillb, C. Santato, Locating the bandgap edges of eumelanin thin films for applications in organic electronic, J. Chem. Technol. Biotechnol. 97 (2022) 837-843.
[60] W. Xu, W. Yang, H. Guo,L. Ge, J. Tu, C. Zhen, Constructing a TiO2/PDA core/shell nanorod array electrode as a highly sensitive and stable photoelectrochemical glucose biosensor, RSC Adv. 10 (2020) 10017-10022. https://doi.org/10.1039/C9RA10445C.

Supplementary Material for

$NaNbO_3$/Eumelanin composite: a new photocatalyst under visible light

TEXTURAL PROPERTIES

Textural properties (Table S1) was estimated using equipment (Gemini, VII 2390A) in the presence of liquid nitrogen (77 K), using the Multipoint Brunauer, Emmett and Teller (BET) equation, done automatically by the instrument.

Table S1: Textural properties.

Sample	S_{BET} (m^2/g)	Pore volume (cm^3/g)	Pore diameter (Å)
$NaNbO_3$	12.0131	0.030793	102.5329
Eumelanin	3.0677	0.014025	182.8708
$NaNbO_3$/Eumelanin composite	8.5091	0.032823	154.2940

PHOTOLUMINESCENCE

Experimental:

The photoluminescence (PL) of the samples was analyzed using a miniPL/Raman spectrometer (Photon Systems), with excitation laser of 248.6 nm (~5.0 eV), monochromator of 1/8 m (Czerny-Turner), diffraction grating of 600 g/mm, and a photomultiplier with detection range 190-800 nm.

Results and discussion:

To complement the understanding of the photocatalytic activity of the samples, the PL spectroscopy technique was performed, which allows knowing the behavior the photogenerated charge recombination process. The spectra are shown in Fig. S1. All profiles have a typical behavior of multiphonic processes, resulting in a broadband emission [1,2]. It is observed that the $NaNbO_3$/Eumelanin composite showed a decrease in intensity luminescence emission, indicating that $NaNbO_3$ inhibits the recombination process of the electron/hole pair, favoring photocatalysis.

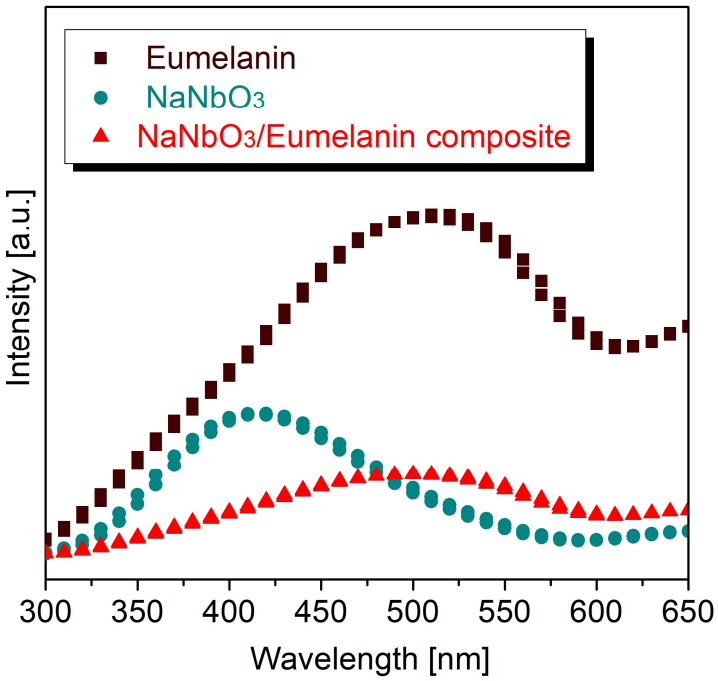

Figure S1: PL spectra.

REFERENCES

[1] C. L. Ücker, L. T. Gularte, C. D. Fernandes, V. Goetzke, E. C. Moreira, C. W. Raubach, M. L. Moreira, S. S. Cava, Investigation of the properties of niobium pentoxide for use in dye-sensitized solar cells, J. Am. Ceram. Soc. 102 (2019) 1884-1892. https://doi.org/10.1111/jace.16080.

[2] C. L. Ücker, F. Riemke, V. Goetzke, M. L. Moreira, C. W. Raubach, E. Longo, S. S. Cava, Facile preparation of Nb2O5/TiO2 heterostructures for photocatalytic application, Chem. Phys. Imp. 4 (2022) 100079. https://doi.org/10.1016/j.chphi.2022.100079.

3.3 Artigo 3

O artigo intitulado *"Cu-doped $NaNbO_3$ nanorods: Enhanced photocatalytic activity for RhB dye removal and antibacterial activity against E. coli"* é apresentado conforme publicado no periódico *Ceramics International (Online* ISSN:1873-3956 *and Print* ISSN:0272-8842), classificação A1 na área de Materiais.

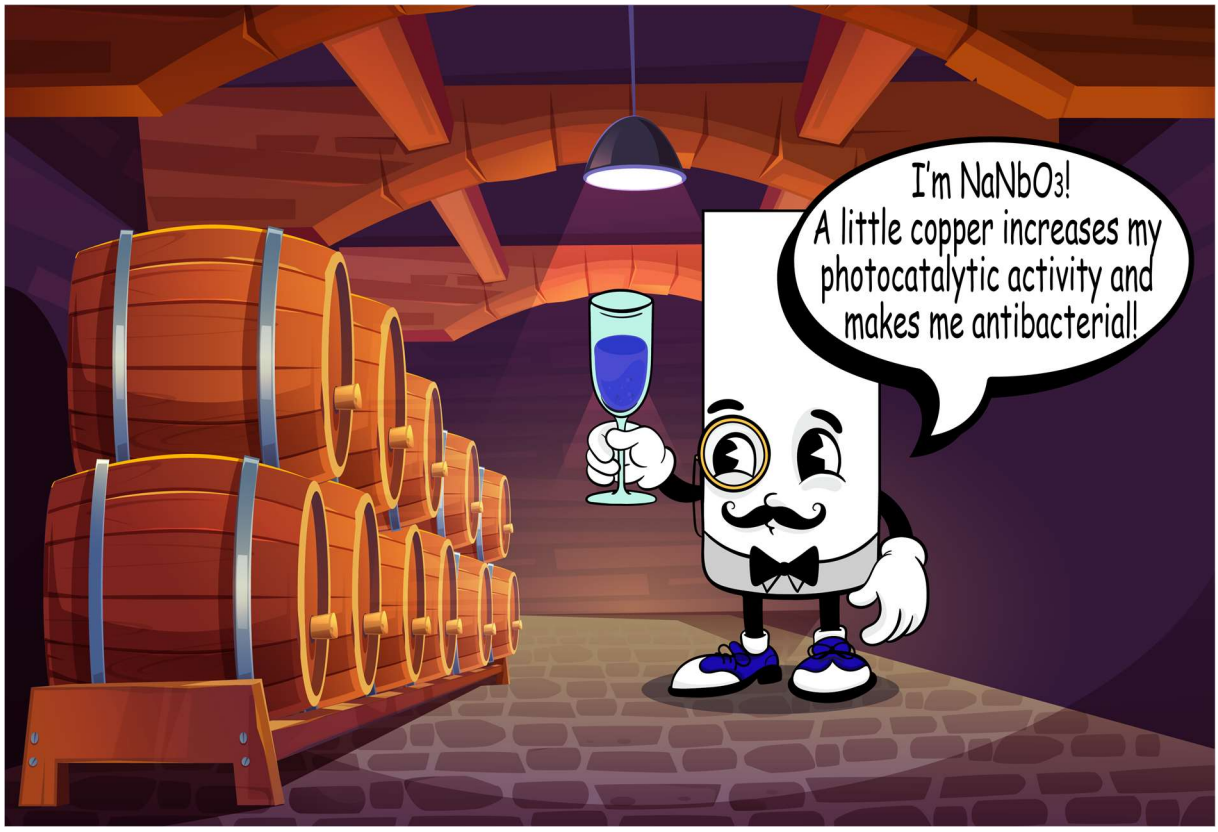

Figura 12 - Resumo gráfico Artigo 3.

Fonte: Elaborado pela autora, 2024.

Cu-doped $NaNbO_3$ nanorods: enhanced photocatalytic activity for RhB dye removal and antibacterial activity against *E. coli*

Daiane Fernandes[a,*], Ramon D. Carvalho[b,c], Carla M. Trassante[d], Vagner da S. Dias[b], Luize G. B. de Melo[d], Cristiane W. Raubach[a], Mario L. Moreira[a,b], Pedro L. G. Jardim[a,b], Mateus M. Ferrer[a], Eduardo C. Moreira[e], Carlos Frederico de O. Graeff[f,g], Rafael G. Lund[h], Rodrigo de A. Vaucher[d], Sergio da S. Cava[a,b]

[a]Post-Graduate Program in Materials Science and Engineering, Federal University of Pelotas, 96010-610, Pelotas, RS, Brazil

[b]Post-Graduate Program in Physics, Federal University of Pelotas, 96160-000, Capão do Leão, RS, Brazil

[c]Department of Chemistry, São Carlos Federal University, 13565-905, São Carlos, SP, Brazil

[d]Post-Graduate Program in Microbiology and Parasitology, Federal University of Pelotas, 96160-000, Capão do Leão, RS, Brazil

[e]Spectroscopy Laboratory, Federal University of Pampa, 96413-172, Bagé, RS, Brazil

[f]Post-Graduate Program in Materials Science and Technology, São Paulo State University, 17033-360, Bauru, SP, Brazil

[g]Department of Physics, São Paulo State University, 17033-360, Bauru, SP, Brazil

[h]School of Dentistry, Federal University of Pelotas, 96010-560, Pelotas, RS, Brazil

*Corresponding author: daiane.fg.eng@outlook.com

A B S T R A C T

Sodium niobate ($NaNbO_3$) nanorods with Cu (0.00, 0.01, 0.02 and 0.04 mmol) insertion were prepared by the microwave-assisted hydrothermal method and the photocatalytic and antibacterial activity was explored for the first time. X-ray diffraction confirms the coexistence of two orthorhombic phases (P21ma and Pbma) for all samples, with the percentage of each phase being strongly influenced by doping. The micrographs reveal that doping did not alter the shape or size of the grains (nanorods, with a diameter of ~200 nm and a length of tens micrometers). The samples of pure $NaNbO_3$ and those with 0.01 and 0.02 mmol of Cu showed an average band gap value of 3.08 eV. However, the sample containing 0.04 mmol of Cu exhibited a slight redshift. The photocatalytic activity of the samples was assessed by the removal of Rhodamine B dye (RhB), under ultraviolet light. All doped samples exhibited superior performance, with the sample containing 0.02 mmol of Cu showing the best photocatalytic activity, achieving 100% RhB removal in 50 minutes. This was attributed to a lower rate of recombination of photogenerated charges, as evaluated through photoluminescence analysis. Additionally, the photocatalyst demonstrated excellent recyclability over three cycles. Pure $NaNbO_3$ nanorods showed no antibacterial activity, but doping with 0.04 mmol of Cu reduced the growth of *Escherichia coli.*

Keywords: sodium niobate, nanorods, Cu-doping, photocatalysis, antibacterial activity.

1. Introduction

Water pollution represents a global challenge, as this natural resource is vital for all biodiversity, and the inadequate disposal of untreated industrial effluents exacerbates the problem. Among the contaminants found in wastewater, dyes represent a significant fraction due to their wide use in various industrial sectors [1]. In particular, Rhodamine B (RhB) is a widely used xanthene cationic dye and is highly toxic, carcinogenic, and mutagenic. Due to its high chemical stability and resistance to degradation, it persists in the environment for long periods, making its removal from wastewater crucial [2,3]. Notably, photocatalytic degradation has proven to be an effective technology [3-9]. The photocatalytic mechanism involves the activation of a semiconductor by the absorption of photons. Electrons are promoted from the valence band (VB) to the conduction band (CB), forming electron/hole pairs (e^-/h^+), which then participate in oxidation/reduction reactions. To improve the efficiency of photocatalysts, doping has been recognized as a promising approach [7-10]. Appropriate insertion of ions into the semiconductor lattice can reduce the band gap, thus requiring less energy to generate e^-/h^+ pairs [7-10]. Additionally, the recombination of photogenerated charges can be delayed by the formation of intermediate energy levels, which extends their useful life [7-10].

Sodium niobate ($NaNbO_3$) is a multifunctional ceramic with a Perovskite-type structure. Among its technological applications, it exhibits high photocatalytic activity [4,5,11-13]. The possibility of obtaining one-dimensional $NaNbO_3$ through calcination of the metastable phase $Na_2Nb_2O_6.H_2O$, synthesized by hydrothermal methods, represents a significant advantage [4,5,12]. The nanoscale one-dimensionality, higher crystallinity, and anisotropic nature of this type of structure confer superior photocatalytic activity when compared to cubic grains [11-13]. Studies on the doping of $NaNbO_3$ with several ions have been conducted to evaluate structural and luminescent properties [14-22]. However, few have focused on photocatalytic applications. Doping with N, Ca, K, V, and Ta has been reported for this purpose [23-27], demonstrating that a wide range of ions can be explored. In particular, doping with copper (Cu) ions has shown promising results [28-30].

Antibacterial properties in any material can be an important differentiator, as many strains pose a serious public health problem [31]. In particular, Cu is known for its strong and effective antibacterial action. Cu ions, especially Cu^{2+}, can penetrate

bacterial cells, alter protein synthesis, promote DNA degradation, interfere with cellular metabolism and membrane function, resulting in cell death or growth inhibition [32-34]. Research incorporating this metal into polymers, activated carbon, and semiconductors, for example, has shown outstanding results [35-38]. In this context, we report for the first time the synthesis of $NaNbO_3$ nanorods with different concentrations of Cu (0.01, 0.02, and 0.04 mmol). The effect of doping on photocatalytic and antibacterial activity was investigated through the removal of Rhodamine B (RhB) dye and inhibiting the growth of *Escherichia coli* (*E. coli*), respectively.

2. Materials and methods

Pure $NaNbO_3$ (SN) was obtained according to our previous studies [4,5], with some modifications. 0.25 mol of NaOH (Merck, 99.0%) and 3.76 mmol of Nb_2O_5 (supplied by CBMM) were solubilized in 30 mL distilled water by magnetic stirring at room temperature. The final solution was heated to 150 ºC in the adapted-microwave (800 W, PANASONIC) for 105 min. The obtained precipitate was washed and centrifuged until the pH was neutralized and then dried in an oven. The final powder was subjected to a thermal treatment at 550 °C for 2 h and naturally cooled. To prepare the doped samples, $Cu(NO_3)_2{\cdot}3H_2O$ (Sigma-Aldrich, 97.0%) was added to the solution to obtain 0.01 (SNC1), 0.02 (SNC2) and 0.04 (SNC3) mmol of Cu.

The crystalline structure was determined by X-ray diffraction (XRD) (Ultima IV, RIGAKU) with Cu-Kα radiation (λ=1.5406 Å). Scanning electron microscopy (SEM) images were obtained using an electron microscope (Helios Nanolab 600i, FEI), operating at 5 kV. Band gap energies were estimated by diffuse reflection spectroscopy using an Uv-vis spectrometer (HR2000+, OCEAN OPTICS). The photoluminescence (PL) was analyzed using a fluorescence spectrometer (Cary Eclipse, AGILENT), with excitation laser of 250 nm.

The photocatalytic activity was evaluated under ultraviolet light (06 lamps of 15 W each, λ = 254 nm). The photocatalytic reaction was carried out with 50 mg of each photocatalyst dispersed in 50 mL of RhB solution (1×10^{-5} M), under stirring magnetic at room temperature. All samples were stirred in the dark for 30 min to achieve adsorption-desorption equilibrium. The variation in RhB concentration was recorded by absorbance at 554 nm, using a UV-Vis spectrophotometer (SP200 UV, BEL

PHOTONICS). In the reuse experiment, after each analysis the photocatalyst was separated by centrifugation and dried overnight. The proportion between the photocatalyst and the dye solution was maintained at 1 mg/1 mL. All experiments were carried out in triplicate.

The antimicrobial test was conducted using the macrodilution method, in accordance with CLSI M7-A6. In a glass tube, 1 mL of MacConkey broth (KASVI) 100 µL of inoculum prepared with the *E. coli* strain, and 100 µL of the diluted sample (12 mg of powder and 3 mL of dimethyl sulfoxide (Synth, 99.9%)) were added. For the positive control, a tube containing 1 mL of MacConkey broth and 100 µL of inoculum was prepared. For the negative control, a tube with only 1 mL of MacConkey broth was used. The tubes were incubated under agitation for 24 hours. After this period, the contents of the tubes were plated on Petri dishes containing MacConkey agar. The experiments were performed in triplicate.

3. Results and discussion

The diffractograms (Fig. 1) indicate that all samples are composed of two orthorhombic symmetries: space group P21ma and space group Pbma. Structural refinement using the Rietveld method showed good agreement between theoretical and experimental data (Fig. S1a-d). This polymorphism was recently detailed by Teixeira et al. [39]. Studies has reported that sub-micrometer particles favor the polar P21ma phase [40,41]. The polar phase is also favored by crystallization at relatively low temperatures (600 °C), but it transforms at higher temperatures (below 950 °C) into the stable centrosymmetric Pbma structure [42]. The second-order Jahn-Teller distortion of Nb^{5+} is pronounced in the P21ma lattice due to the same mirror symmetry shared by the two Na atoms. In Pbma, the Na atoms occupy sites with distinct symmetries, contributing to competing bonds that render the [NbO_6] octahedron less distorted and more rigid [42]. The parameters obtained in the refinement are described in Table 1. The SN sample showed a higher percentage of the P21ma, in accordance with previous descriptions. For doped samples, a significant variation in phase proportions is observed. It is widely recognized that Cu (II) induces distortions in octahedra due to the pronounced Jahn-Teller effect, resulting from its d^9 electronic configuration [43]. Although no studies have specifically examined the effect of inserting this ion into the $NaNbO_3$ lattice, our preliminary results indicate that it is

present in the structure and is capable of inducing accentuated symmetry transitions. This investigation has potential to be explored in future research.

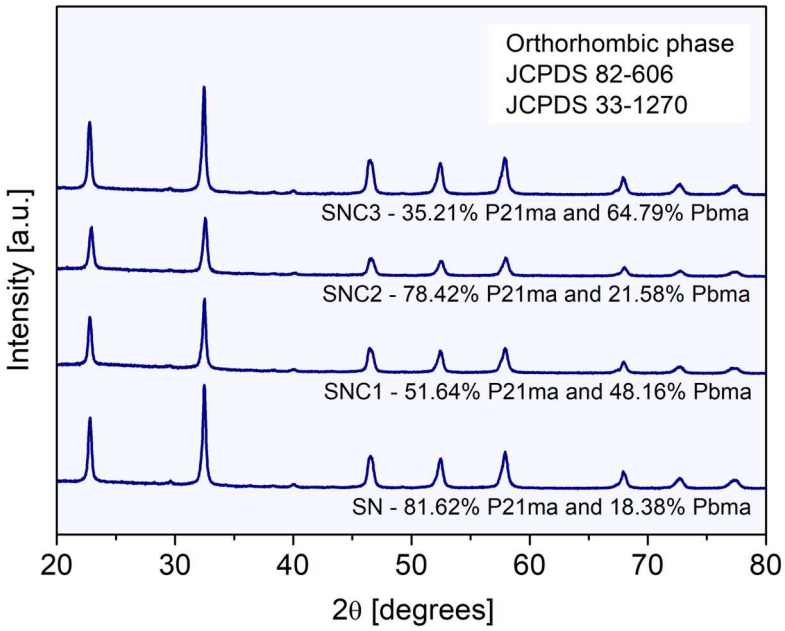

Figure 1. XRD patterns.

The SEM images shown in Fig. 2 (a-d) clearly reveal that the insertion of the dopant did not alter the shape or size of the grains. All samples exhibit rod-like shape, with average dimensions of ~200 nm in diameter and lengths of tens micrometers. Additionally, an elemental analysis of the samples was performed using energy-dispersive X-ray spectroscopy (EDX). The EDX spectra confirm the presence of Cu in all doped samples (Fig. S2a-c).

Fig. 3a shows the photocatalytic activity of the samples. C_0 is the initial concentration of RhB and C is the point concentration over time. The addition of the SN sample to the solution induced ~60.7% dye removal in 50 min, a lower activity when compared to all doped samples. An improvement in photocatalytic activity is observed with increasing doping concentration. Samples SNC1 and SNC2 were able to remove 73.2% and 100% of RhB, respectively. However, the sample SNC3 removed 70.4% of the dye, demonstrating that there is a limit beyond which the insertion of impurity ions ceases to be beneficial in the photocatalytic process. In additional, reuse and active species experiments were conducted with sample SNC2.

The addition of disodium ethylenediaminetetraacetate (EDTA), isopropyl alcohol (C_3H_8O), and p-benzoquinone ($C_6H_4O_2$) significantly reduced the removal of RhB, indicating that h^+, •OH (hydroxyl radical), and $•O_2^-$ (superoxide radical anion) respectively, are crucial active species in the photocatalytic reaction (Fig. 3b). With the presence of silver nitrate ($AgNO_3$) the discoloration was the same, indicating that the e^- are not active species (Fig. 3b). The SNC2 sample demonstrated consistent performance, confirming its stability and high efficiency as a photocatalyst after three consecutive 50-minute cycles. According to the results, a mechanism for photocatalytic removal of RhB is proposed. Under UV light, the photocatalyst produces e^-/h^+ pairs in the CB and VB, respectively. The h^+ can react with water to form •OH or directly oxidize the dye. Meanwhile, the e^- can react with oxygen to form $•O_2^-$, that can react with water to produce •OH. All species are reactive and lead to the degradation of RhB.

Table 1

Structural parameters from Rietveld refinement.

P21ma				
Parameters	**SN**	**SNC1**	**SNC2**	**SNC3**
Wt% phase	81.62	51.84	78.42	35.21
a [Å]	5.54136	5.56269	5.56611	5.56205
b [Å]	7.78181	7.78490	7.79443	7.77850
c [Å]	5.51198	5.51557	5.52143	5.50502
V [$Å^3$]	237.687	238.852	239.545	238.171
χ^2	1.96	1.65	1.56	1.56
Pbma				
Parameters	**SN**	**SNC1**	**SNC2**	**SNC3**
Wt% phase	18.38	48.16	21.58	64.79
a [Å]	5.57206	5.54143	5.57206	5.55378
b [Å]	15.54886	15.55726	15.54886	15.56148
c [Å]	5.50672	5.50314	5.50672	5.51143
V [$Å^3$]	477.098	474.423	475.993	476.326
χ^2	1.96	1.65	1.56	1.56

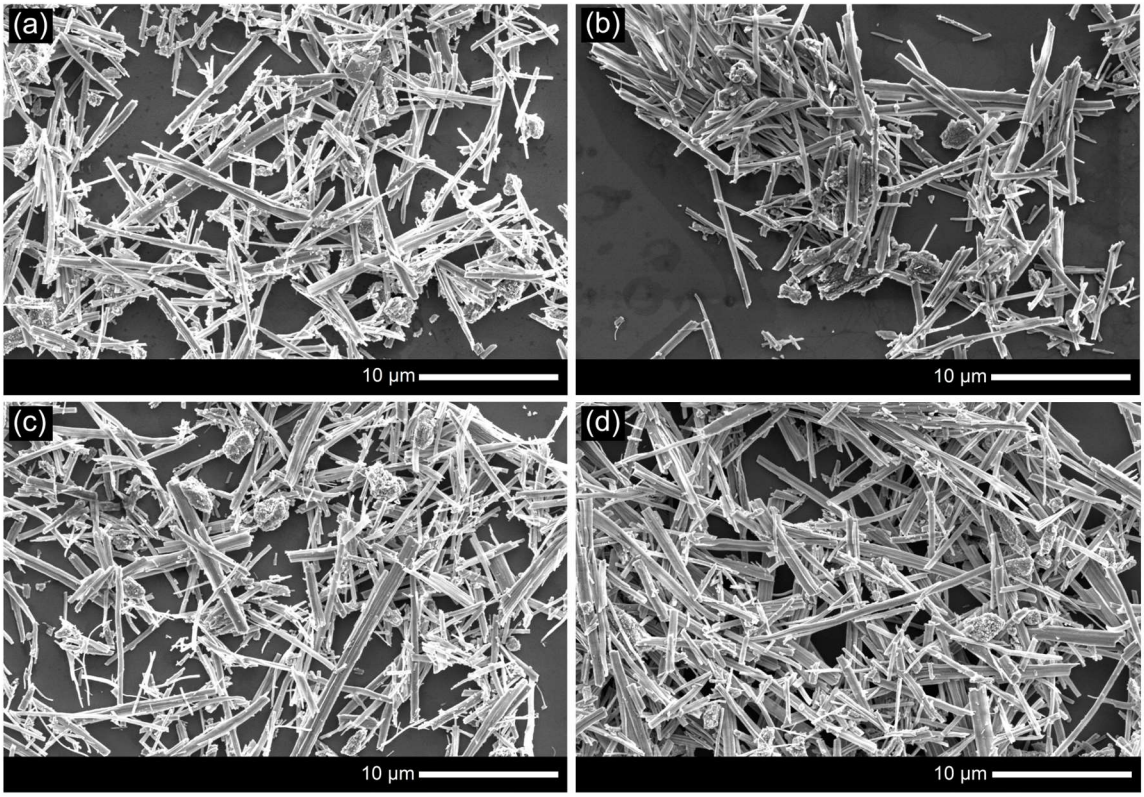

Figure 2. SEM images: (a) SN, (b) SNC1, (c) SNC2 and (d) SNC3.

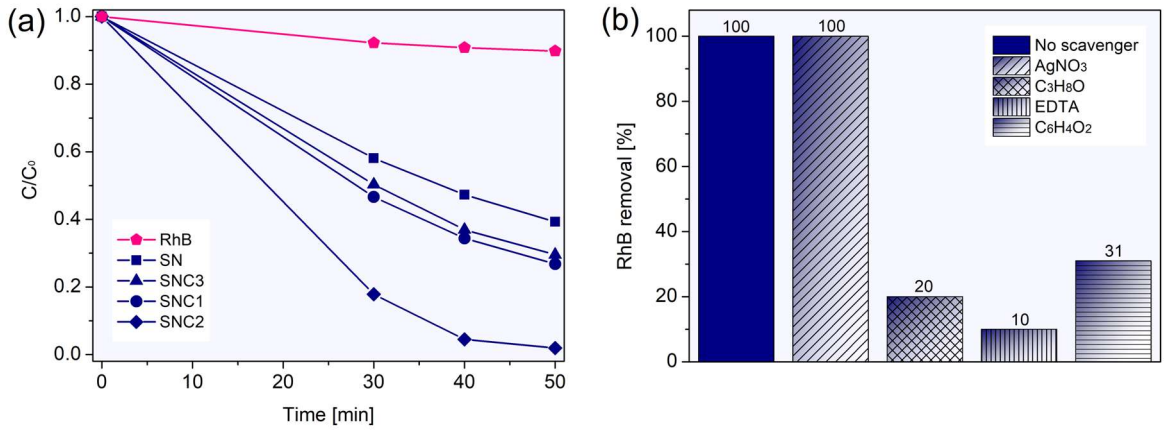

Figure 3. (a) Photocatalytic activity and (b) Experiment of active species.

The band gap energies were estimated using the Wood/Tauc method [44] and are presented in Fig. 4a. Although the samples exhibit coexistence of the P21ma and Pbma space groups, Gouget et al. [42] reported that the electronic structure of both are similar. The CB is mainly composed of Nb4d orbitals and the VB of O2p orbitals,

so the optical gap is determined by direct transitions between these orbitals [5,45]. In the SN, SNC1, and SNC2 samples, no significant change in the band gap was observed, probably due to the low concentration of Cu. The estimated energies for these samples averaged 3.08 eV. However, in the SNC3 sample, a slight redshift is observed. This occurs because the increased concentration of Cu shifts the Fermi level toward the CB due to its higher valence. The reduction of the band gap is important in photocatalysis, as it requires less energy to activate the photocatalyst. However, in this study, the energies were similar and did not serve as a determining factor in explaining the photocatalytic activity. Additionally, it is important to note that in the doped samples, an absorption band extending between the yellow and red regions was identified. This absorption, also reported by Choudhury et al. [43], is attributed to the d-d electronic transition of Cu^{2+}.

Fig. 4b-e display the photoluminescence (PL) emission spectra. All samples presented similar profiles with emission in the blue and green regions, indicating that recombination occurs via a multiphonon transitions. Fig. 4f shows that the luminescence emission decreases for the SNC1 and SNC2 samples compared to SN. This decrease in intensity suggests a reduced rate of photogenerated charge recombination, which favors the photocatalytic process [8,24]. This explains the superior performance of the SNC1 and SNC2 photocatalysts. For sample SNC3, the emission was significantly higher, which explains its lower photocatalytic activity compared to the doped samples. Although the emission was also greater than that of the SN sample, the smaller band gap likely offset the higher recombination rate of the e^-/h^+ pairs, resulting in slightly superior activity.

The antimicrobial activity is shown in Fig. 5. Compared to the positive control, the SN sample did not inhibit the growth of *E. coli* (Fig. 5a). Interestingly, the SNC2 sample promoted bacterial growth (Fig. 5b). Cu is essential for many organisms, including *E. coli*, acting as a cofactor for various enzymes required for cellular processes, thus being considered a nutrient at low concentrations [46]. However, at higher concentrations, its toxic effects become predominant, leading to growth inhibition or even bacteria death [47]. This behavior is clearly observed in the SNC3 sample, which inhibited bacterial growth (Fig. 5c). The cell wall of *E. coli* (Gram-negative) is composed of anionic surfaces [36,48], which confer a high affinity for cation. Consequently, direct contact between the bacterium and the Cu^{2+} ions may

lead to bacterial lysis and also facilitate the penetration of these ions into the cell, thereby altering essential metabolic processes.

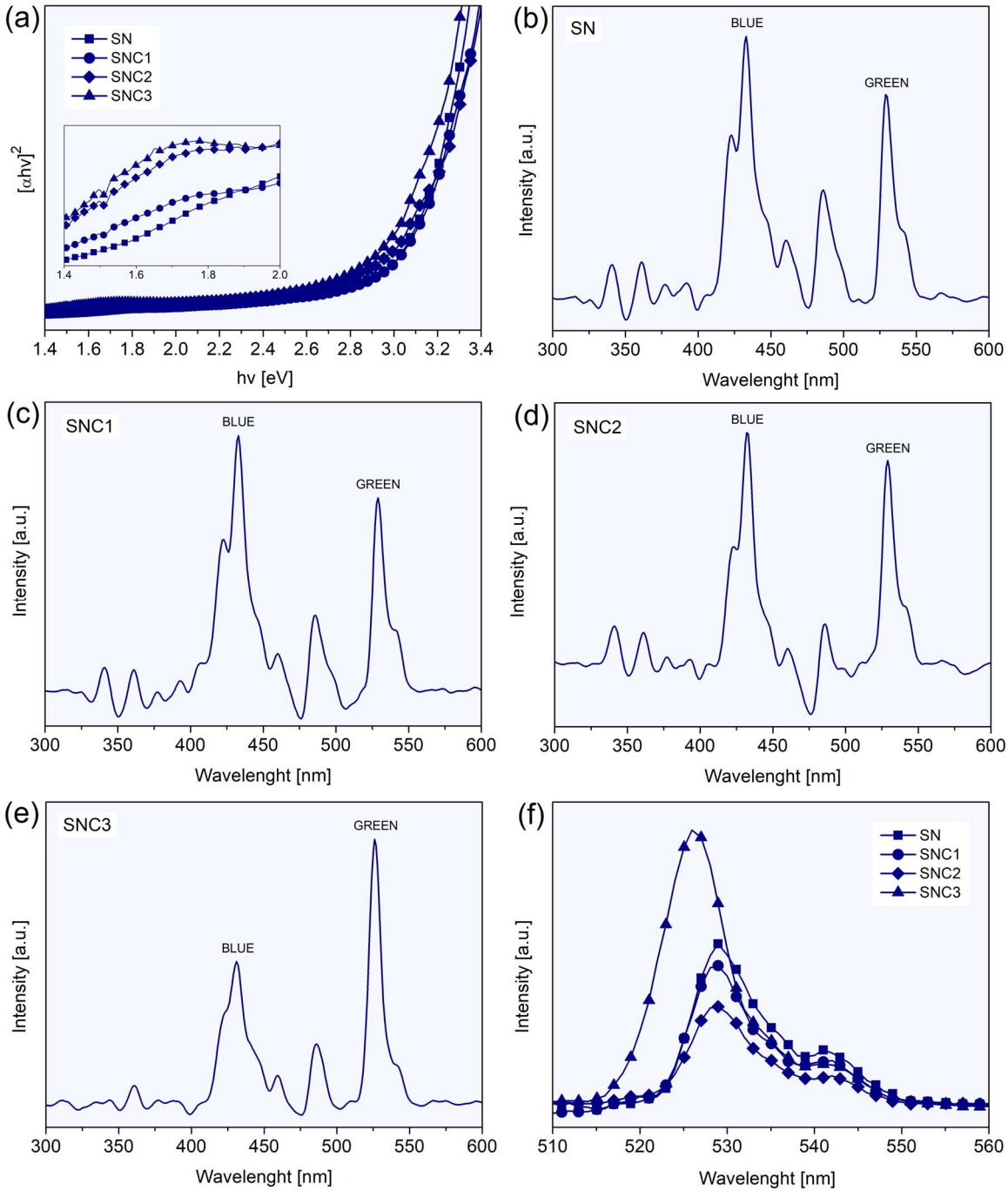

Figure 4. (a) Band gap energies and (b-f) PL emission.

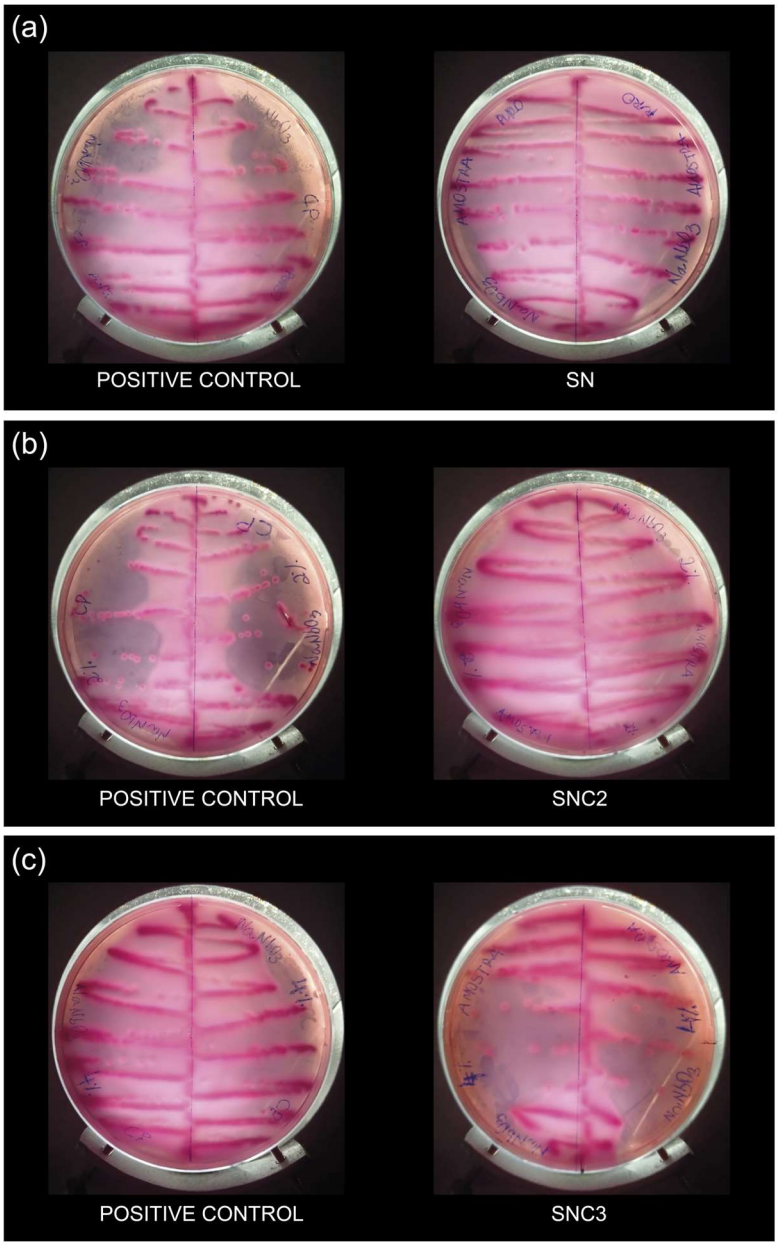

Figure 5. Antibacterial activity against *E. coli*: (a) SN, (b) SNC2 and (c) SNC3.

4. Conclusions

In conclusion, pure $NaNbO_3$ nanorods and with different concentrations of Cu were successfully prepared using the microwave-assisted hydrothermal technique. All samples exhibited the coexistence of two orthorhombic symmetries, and doping significantly influenced the percentage of each phase. SEM images revealed that doping did not alter the shape or size of the grains. Doping increased the photocatalytic activity of $NaNbO_3$. While pure $NaNbO_3$ nanorods did not exhibit antibacterial activity, doping with 0.004 mmol Cu led to inhibition of *E. coli* growth.

Overall, the insertion of Cu ions into the $NaNbO_3$ lattice proved beneficial for photocatalytic activity and imparted antibacterial properties to the ceramic. Therefore, this study is expected to serve as a reference for future research on $NaNbO_3$ doping for photocatalytic and antibacterial applications.

Acknowledgments

The authors thank Companhia Brasileira de Metalurgia e Mineração (CBMM) and Núcleo de Apoio à Pesquisa em Ciência e Engenharia de Materiais (NAPCEM-UNIFESP Campus São José dos Campos). This research received support from Coordenação de Aperfeiçoamento de Pessoal de Nível Superior (CAPES), Conselho Nacional de Desenvolvimento Científico e Tecnológico (CNPq - Process nº 406160/2023-6, nº 406311/2023-4 and n° 406193/2022-3 INCT-NAMITEC) and Fundação de Amparo à Pesquisa do Estado do Rio Grande do Sul (FAPERGS - Process nº 17/2551-0000889-8 and n° 19/2551-0001974-2).

References

[1] S. Sudarshan, S. Harikrishnan, G. RathiBhuvaneswari, V. Alamelu, S. Aanand, A. Rajasekar, M. Govarthanan, Impact of textile dyes on human health and bioremediation of textile industry effluent using microorganisms: current status and future prospects, J. Appl. Microbiol. 134 (2023) 1-2. https://doi.org/10.1093/jambio/lxac064.

[2] A. K. Al-Buriahi, A. A. Al-Gheethi, P. S. Kumar, R. M. S. R. Mohamed, H. Yusof, A. F. Alshalif, N. A. Khalifa, Elimination of rhodamine B from textile wastewater using nanoparticle photocatalysts: A review for sustainable approaches, Chemosphere 287 (2022) 132162. https://doi.org/10.1016/j.chemosphere.2021.132162.

[3] L. Guganathan, R. Ramasamy, K. Sathishkumar, K. Vanitha, Khalid M. Batoo, A. A. Ibrahim, S. Ragupathy, Critical assessment of a Ce-doped SnO2 loaded on PPSAC composite photocatalyst on improved photocatalytic activity under visible light, Ionics. 30 (2024) 2915-2926. https://doi.org/10.1007/s11581-024-05461-0.

[4] D. Fernandes, C. W. Raubach, P. L. G. Jardim, M. L. Moreira, S. S. Cava, Synthesis of NaNbO3 nanowires and their photocatalytic activity, Ceram. Int. 47 (2021) 10185-10188. https://doi.org/10.1016/j.ceramint.2020.12.070.

[5] D. Fernandes, M. M. Ferrer, C. W. Raubach, M.L. Moreira, P. L. G. Jardim, E. C. Moreira, C. F. O. Graeff, S. S. Cava, Fast synthesis of NaNbO3 nanoparticles with high photocatalytic activity for degradation of organic dyes, J. Am. Ceram. Soc.106 (2022) 399-409. https://doi.org/10.1111/jace.18740.

[6] D. Fernandes, C. W. Raubach, M. M. Ferrer, P. L. G. Jardim, C. F. O. Graeff, M. L. Moreira, E. C. Moreira, V. R. Mastelaro, S. S. Cava, NaNbO3/Eumelanin composite: A new photocatalyst under visible light, Ceram. Int. 49 (2023) 7099-7104. https://doi.org/10.1016/j.ceramint.2022.12.094.

[7] C. L. Ücker, S. R. Almeida, M. L. Vitale, F. C. Riemke, M. M. Ferrer, E. C. Moreira, C. W. Raubach, S. Cava, Photocatalytic performance of Al and Nb-doped TiO2 nanoparticles prepared by microwave-assisted hydrothermal method. Int. J. Appl. Ceram. Technol. 2 (2023) 1963-1977. https://doi.org/10.1111/ijac.14294.

[8] C. L. Ücker, V. Goetzke, F. C. Riemke, M. E. Oliveira, N. L. V. Carreno, F. D. P. Morisso, M. D. Teodoro, V. R. Mastelaro, M. L. Moreira, C. W. Raubach, S. S. Cava, The photocatalytic performance of Fe inserted in Nb2O5 obtained by microwave-assisted hydrothermal synthesis: Factorial design of experiments, J. Photochem. Photobiol. A: Chem. 435 (2023) 114294. https://doi.org/10.1016/j.jphotochem.2022.114294.

[9] M. Geetha, S. Renukadevi, D. S. Kumar, S. Ragupathy, Efficient photocatalytic degradation of rhodamine B using Ag-doped TiO2-loaded groundnut shell activated carbon under solar light, Ionics. 30 (2024) 1167-1176. https://doi.org/10.1007/s11581-023-05344-w.

[10] K. Sathishkumar, P. Harishsenthil, S. M. Naidu, B. Srividhya, L. Guganathan, K. M. Batoo, M. F. Ijaz, M. Ramamoorthy, S. Ragupathy, Impact of metal doping and non metal loading on the photocatalytic degradation of organic pollutants using tin dioxide catalyst under sunlight irradiation, J. Mol. Struct. 1321 (2025) 13984. https://doi.org/10.1016/j.molstruc.2024.139841.

[11] H. Shi, T. Wang, J. Chen, C. Zhu, J. Ye, Z. Zou, Photoreduction of Carbon Dioxide Over NaNbO3 Nanostructured Photocatalysts, Catal. Lett. 141 (2011) 525-530. https://doi.org/10.1007/s10562-010-0482-1.

[12] Q. Liu, L. Zhang, Y. Chai, W.-L. Dai, Facile fabrication and mechanism of single crystal sodium niobate photocatalyst: insight into the structure features influence on

photocatalytic performance for H2 evolution, J. Phys. Chem. C. 121 (2017) 25898-25907. https://doi.org/10.1021/acs.jpcc.7b08819.
[13] C. Yan, B. Li, J. Wang, A Comparative Study of Photodegradation Behavior Sodium Niobate Nanowires and Microcubes, Key Eng. Mater. 861 (2020) 221-227. https://doi.org/10.4028/www.scientific.net/KEM.861.221.
[14] P. Vlazan, S. Florina Rus, M. Poienar, P. Sfirloaga, The effect of dopant concentrations on the structural, morphological and optical properties of NaNbO3 semiconductor materials, Mater. Sci. Semicond. Process.102 (2019) 104602. https://doi.org/10.1016/j.mssp.2019.104602.
[15] X. Yang, L. Zhao, W. Chen, Z. Liu, X. Fan, S. Tian, X. Xu, J. Qiu, X. Yu, Low-temperature red long-persistent luminescence of Pr3+ doped NaNbO3 with a perovskite structure, J. Lumin. 208 (2019) 290-295. https://doi.org/10.1016/j.jlumin.2018.12.066.
[16] J. F. da Silva, C. Jacinto, A. L. Moura, Giant sensitivity of an optical nanothermometer based on parametric and non-parametric emissions from Tm3+ doped NaNbO3 nanocrystals, J. Lumin. 226 (2020) 117475. https://doi.org/10.1016/j.jlumin.2020.117475.
[17] H. Ji, J. Tang, X. Tang, Z. Yang, H. Zhang, Y. Qian, Enhanced up conversion emissions of NaNbO3:Er3+/Yb3+ nanocrystals via Mg2+ ions doping, Mater. Lett. 302 (2021) 130348. https://doi.org/10.1016/j.matlet.2021.130348.
[18] S. S.A. Gillani, M. N. Ali, T. Hussain, M. Shakil, R. Ahmad, U. Shuaib, A. Zia, Cubic to tetragonal structural phase transformation in NaNbO3 with peculiar Mg and Ca doping and its repercussions on optoelectronic properties, Optik. 247 (2021) 168017. https://doi.org/10.1016/j.ijleo.2021.168017.
[19] R. Nain, R. K. Dwived, Effect of tuning of charge defects by K, Ba, La doping on structural and electrical behaviour of NaNbO3, Mater. Chem. Phys. 306 (2023) 127999. https://doi.org/10.1016/j.matchemphys.2023.127999.
[20] A. Yadav, S. Sahoo, S. Singh, I. P. Raevski, P. M. Sarun, Influence of Mn-doping on the structure, high-temperature dielectric, and conductive properties of NaNbO3 ceramics, Mater. Sci. Eng. B. 297 (2023) 116796. https://doi.org/10.1016/j.mseb.2023.116796.

[21] P. Vlazan, M. Poienar, I. Malaescu, C. N. Marin, C. Casut, P. Sfrloaga, Exploiting the Bi-doping effect on the properties of NaNbO3 perovskite-type materials, Chem. Phys. 579 (2024) 112203. https://doi.org/10.1016/j.chemphys.2024.112203.
[22] C. S. Htet, A. M. Manjon-Sanz, J. Liu, C. Babori, M. Barati, F. P. Marlton, L. Daniel, M. R. V. Jørgensen, A. Pramanick, Local structural mechanism for enhanced energy storage properties in heterovalent doped NaNbO3 ceramics, J. Eur. Ceram. Soc. 44 (2024) 1597-1609. https://doi.org/10.1016/j.jeurceramsoc.2023.10.072.
[23] R. Jana, A. Gupta, R. Choudhary, O. P. Pandey, Influence of cationic doping at different sites in NaNbO3 on the photocatalytic degradation of methylene blue dye, J. Sol-Gel Sci. Technol. 96 (2020)405-415. https://doi.org/10.1007/s10971-020-05365-1.
[24] U. Farooq, J. Ahmed, S. M. Alshehri, Y. Mao, T. Ahmad, Self-Assembled Interwoven Nanohierarchitectures of NaNbO3 and NaNb1−xTaxO3 (0.05 ≤ x ≤ 0.20): Synthesis, Structural, Characterization, Photocatalytic Applications, and Dielectric Properties, ACS Omega 7 (2022) 16952-16967. https://doi.org/10.1021/acsomega.1c07250.
[25] J. Wu, W. Li, S. Guan, X. Chen, H. Gao, X. Liu, Study on the performance of vanadium doped NaNbO3 photocatalyst degradation antibiotics, Inorg. Chem. Commun. 131 (2021). 108669.https://doi.org/10.1016/j.inoche.2021.108669.
[26] H. Shi, Xi. Li, H. Iwai, Z. Zou, J. Ye, 2-Propanol photodegradation over nitrogen-doped NaNbO3 powders under visible-light irradiation, J. Phys. Chem. Solids. 70 (2009) 931-935. https://doi.org/10.1016/j.jpcs.2009.05.002.
[27] A. S. Vig, N. Rani, A. Gupta, O. P. Pandey, Influence of Ca-doped NaNbO3 and its heterojunction with g-C3N4 on the photoredox performance, Solar Energy. 185 (2019) 469-479. https://doi.org/10.1016/j.solener.2019.04.088.
[28] M. Rashid, M. Ikram, A. Haider, S. Naz, J. Haider, A. Ul-Hamid, A. Shahzadie, M. Aqeel, Photocatalytic, dye degradation, and bactericidal behavior of Cu-doped ZnO nanorods and their molecular docking analysis, Dalton Trans. 2020 (49) 8314-8330. https://doi.org/10.1039/D0DT01397H.
[29] M. Ikram, E. Umar, A. Raza, A. Haider, S. Naz, A. Ul-Hamid, J. Haider, I. Shahzadi, J. Hassan, S. Ali, Dye degradation performance, bactericidal behavior and molecular docking analysis of Cu-doped TiO2 nanoparticles, RSC Adv. 10 (2020) 24215-24233. https://doi.org/10.1039/D0RA04851H.

[30] R. Ghorbali, G. Essalah, A. Ghoudi, H. Guermazi, S. Guermazi, A. E. Hdiy, H. Benhayoune, B. Duponchel, A. Oueslati, G. Leroy, The effect of (In, Cu) doping and co-doping on physical properties and organic pollutant photodegradation efficiency of ZnO nanoparticles for wastewater remediation, Ceram. Int. 49 (2023) 33828-33841. https://doi.org/10.1016/j.ceramint.2023.08.076.

[31] S. Nasrollahian, J. P. Graham, M. Halaji, A review of the mechanisms that confer antibiotic resistance in pathotypes of E. coli, Front. Cell. Infect. Microbiol. 14 (2024) 01-28. https://doi.org/10.3389/fcimb.2024.1387497

[32] A. K. Chatterjee, R. Chakraborty, T. Basu, Mechanism of antibacterial activity of copper nanoparticles, Nanotechnology. 25 (2014) 135101. https://doi.org/10.1088/0957-4484/25/13/135101.

[33] S. Ali, N. Faqir, F. Naz, M. I. Jan, N. Khan, A. Alotaibi, R. Ullah, A Comprehensive Mechanistic Antibacterial and Antibiofilm Study of Potential Bioactive ((BpA)2bp)Cu/Zn Complexes via Bactericidal Mechanisms against Escherichia coli, Molecules. 28 (2023) 2215. https://doi.org/10.3390/molecules28052215.

[34] S. Elmehrath, K. Ahsan, N. Munawar, A. Alzamly, H. L. Nguyen, Y. Greish, Antibacterial efficacy of copper-based metal–organic frameworks against Escherichia coli and Lactobacillus, RSC Adv. 14 (2024) 15821-15831. https://doi.org/10.1039/D4RA01241K.

[35] L. Azizova, V. Chernyshenko, D. Korolova, I. U. Allan, S. Mikhalovsk, L. Mikhalovska, Argatroban- and copper-modifed polymers with improved thromboresistance and antimicrobial properties, J. Mater. Sci. Res. (2024). https://doi.org/10.1557/s43578-024-01389-3.

[36] T. Mahlangu, I. Arunachellan, S. S. Ray, M. Onyango, A. Maity, Preparation of Copper-Decorated Activated Carbon Derived from Platamus occidentalis Tree Fiber for Antimicrobial Applications, Materials. 15 (2022) 5939. https://doi.org/10.3390/ma15175939.

[37] I. E. Medina-Ramírez, M. A. Arzate-Cardenas, A. Mojarro-Olmos, M. A. Romo-López, Synthesis, characterization, toxicological and antibacterial activity evaluation of Cu@ZnO nanocomposites, Ceram. Int. 45 (2019) 17476-17488. https://doi.org/10.1016/j.ceramint.2019.05.309.

[38] A. Jacobs, G. Renaudin, N. Charbonnel, J.-M. Nedelec, C. Forestier, S. Descamps, Copper-Doped Biphasic Calcium Phosphate Powders: Dopant Release,

Cytotoxicity and Antibacterial Properties, Materials. 14 (2021) 2393. https://doi.org/10.3390/ma14092393.
[39] G. F. Teixeira, H. S. Seleghini, W. B. Bastos, N. Jacomaci, B. Stojadinovic, Z. Dohcevic-Mitrovic, F. Colmati, M. A. San-Miguel, E. Longo, M. A. Zaghet, On the coexistence of ferroelectric and antiferroelectric polymorphs in NaNbO3 fibers at room temperature, J. Mater. Chem. C. 11 (2023) 5524-5533. https://doi.org/10.1039/D2TC04039E.
[40] Y. Shiratori, A. Magrez, J. Dornseiffer, F.-H. Haegel, C. Pithan, R. Waser, Polymorphism in Micro-, Submicro-, and Nanocrystalline NaNbO3, J. Phys. Chem. B. 109 (2005) 20122-20130. https://doi.org/10.1021/jp052974p.
[41] Y. Shiratori, A. Magrez, W. Fischer, C. Pithan, R. Waser, Temperature-induced Phase Transitions in Micro-, Submicro-, and Nanocrystalline NaNbO3, J. Phys. Chem. C. 111 (2007) 18493-18502. https://doi.org/10.1021/jp0738053.
[42] G. Gouget, M. Duttine, E. Durand, A. Villesuzanne, V. Rodriguez, F. Adamietz, T. Le Mercier, M.-D. Braida, A. Demourgues, Isolating the Two Room-Temperature Polymorphs of NaNbO3: Structural Features, Optical Band Gap, and Reactivity, ACS Appl. Electron. Mater. 1 (2019) 513-522. https://doi.org/10.1021/acsaelm.8b00125.
[43] B. Choudhury, M. Dey, A. Choudhury, Defect generation, d-d transition, and band gap reduction in Cu-doped TiO2 nanoparticles, Int. Nano Lett. 3 (2013) 25. https://doi.org/10.1186/2228-5326-3-25.
[44] D. L. Wood, J. Tauc, Weak Absorption Tails in Amorphous Semiconductors, Phys. Rev. B. 5 (1972) 3144-3151. https://doi.org/10.1103/PhysRevB.5.3144.
[45] H. Shi, B. Lan, C. Zhang, E. Ye, Y. Nie, B. Bian, Effects of nonmetal doping on electronic structures of NaNbO3 based on hybrid density functional calculation, Mod. Phys. Lett. B. 30 (2016)1650350. https://doi.org/10.1142/S0217984916503504.
[46] K. K. Sharma, D. Singh, S. V. Mohite, P. R. Williamson, J. F. Kennedy, Metal manipulators and regulators in human pathogens: A comprehensive review on microbial redox copper metalloenzymes “multicopper oxidases and superoxide dismutases”, Int. J. Biol. Macromol. 233 (2023) 123534. https://doi.org/10.1016/j.ijbiomac.2023.123534.
[47] E.-I. Koh, A. E. Robinson, N. Bandara, B. E. Rogers, J. P. Henderson, copper import in Escherichia coli by the yersiniabactin metallophore system, Nat. Chem. Biol. 13 (2017) 1016-1021. https://doi.org/10.1038/nchembio.2441.

[48] G. Cárdenas-Triviño, M. J. Saludes-Betanzo, L. Vergara-González, Bactericides Properties of Chitosan Metal Quantum Dots Microbial Pathogenicity Against E. coli, S. aureus, and S. Typhi, Int. J. Polym. Sci. 2020 (2020) 5920941. https://doi.org/10.1155/2020/5920941.

Supplementary Material for

Cu-doped $NaNbO_3$ nanorods: enhanced photocatalytic activity for RhB dye removal and antibacterial activity against *E. coli*

RIETVELD REFINEMENT

Rietveld refinement of the XRD patterns was performed using the FullProf software. The Peak and background profiles were refined according to pseudo-Voigt function.

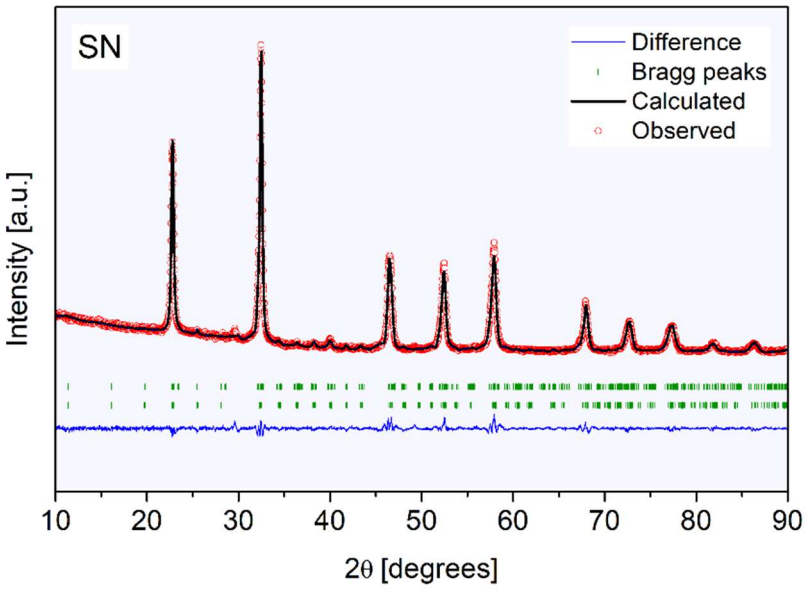

Figure S1-a: SN Rietveld refinement.

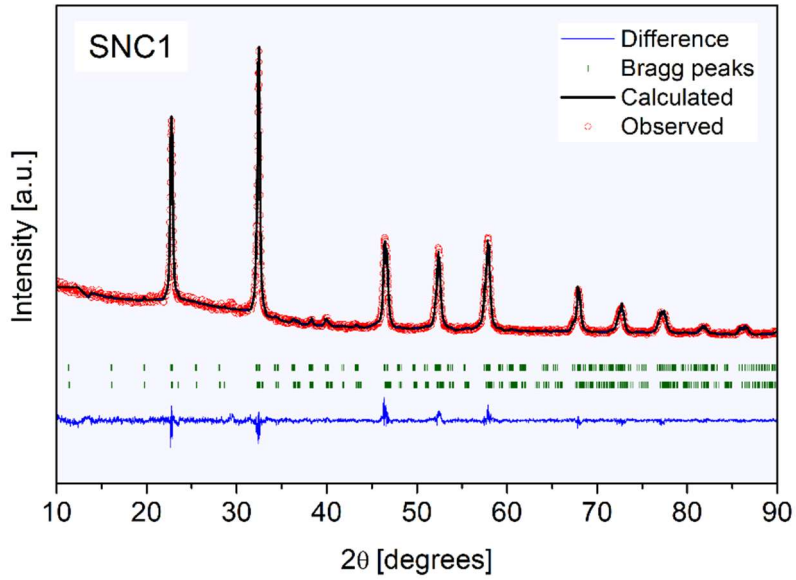

Figure S1-b: SNC1 - Rietveld refinement.

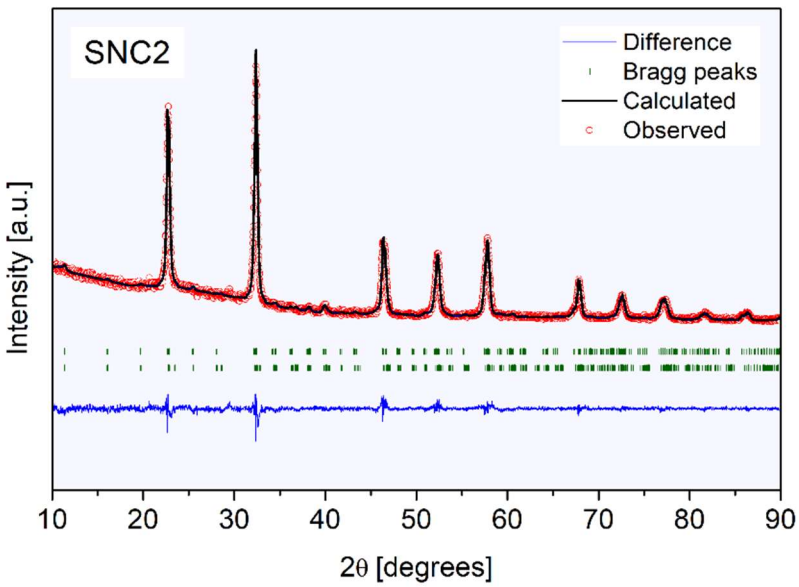

Figure S1-c: SNC2 - Rietveld refinement.

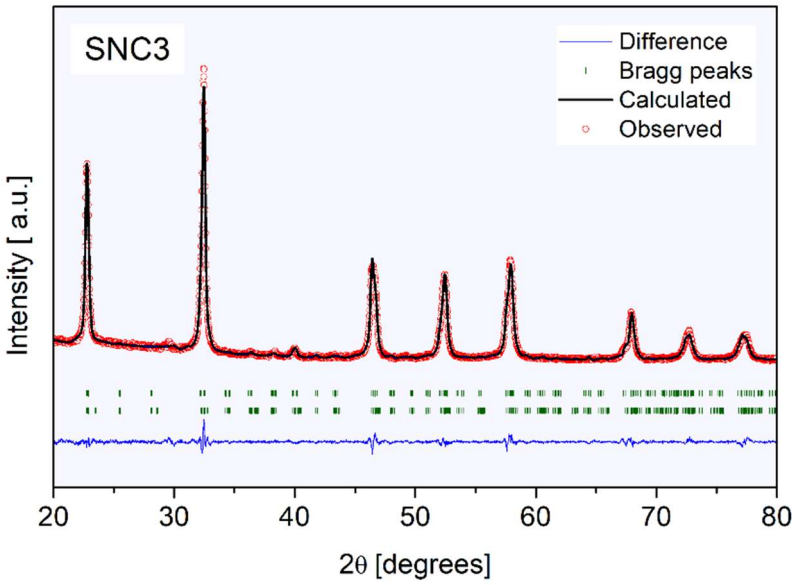

Figure S1-d: SNC3 - Rietveld refinement.

ENERGY-DISPERSIVE X-RAY SPECTROSCOPY

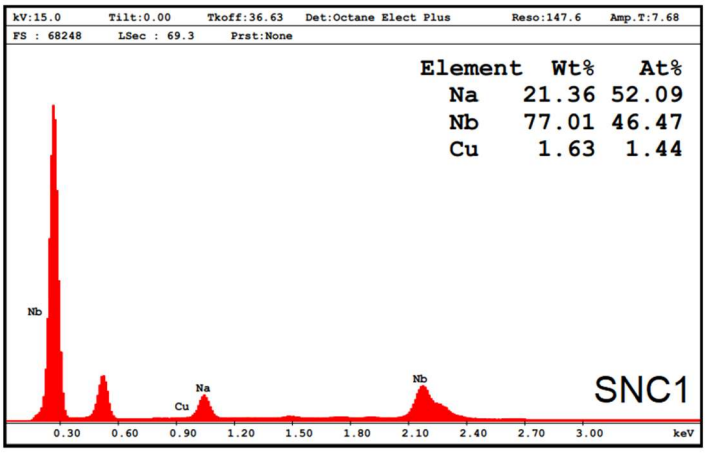

Figure S2-a: SNC1 - EDX spectrum.

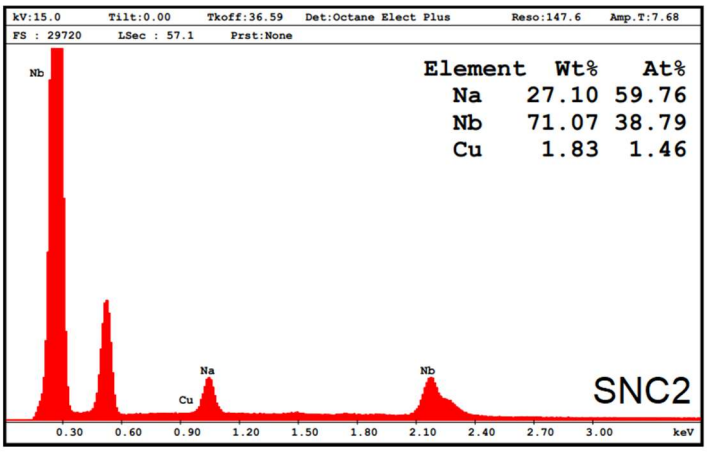

Figure S2-b: SNC2 - EDX spectrum.

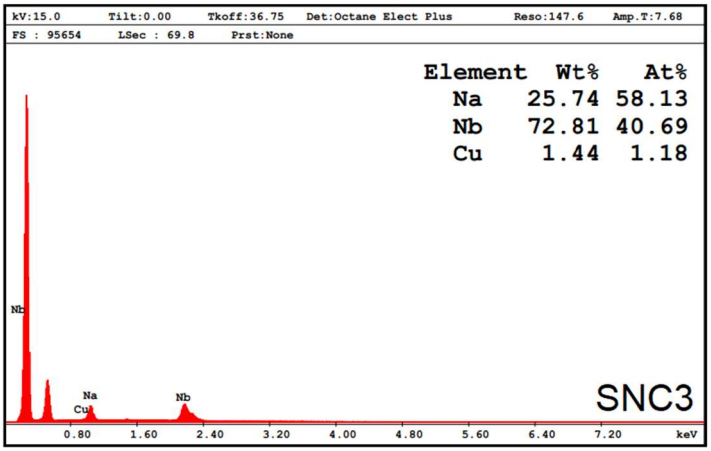

Figure S2-c: SNC3 - EDX spectrum.

3.4 Artigo 4

O artigo intitulado *“Synthesis of Al-doped $NaNbO_3$ rods with enhanced photocatalytic activity”* é apresentado conforme publicado no periódico *Journal of Physics and Chemistry of Solids (Online* ISSN:1879-2553 *and Print* ISSN: 0022-3697), classificação A2 na área de Materiais.

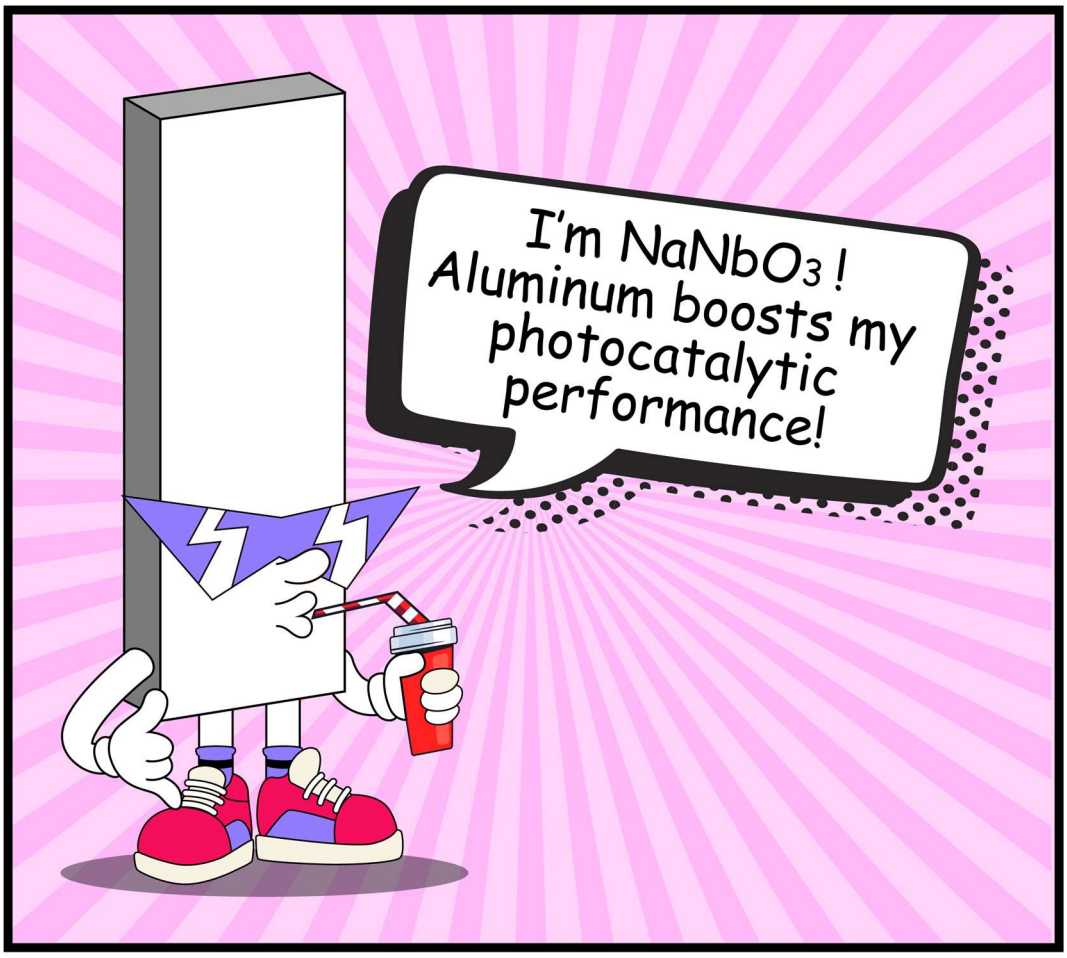

Figura 13 - Resumo gráfico Artigo 4.

Fonte: Elaborado pela autora, 2024.

Synthesis of Al-doped $NaNbO_3$ rods with enhanced photocatalytic activity

Daiane Fernandes[a,*], Cristiane W. Raubach[a], Vagner da S. Dias[b], Ramon D. Carvalho[c], Mario L. Moreira[a,b], Pedro L. G. Jardim[a,b], Mateus M. Ferrer[a], Eduardo C. Moreira[d], Carlos Frederico de O. Graeff[e,f], Elson Longo[c], Sergio da S. Cava[a,b]

[a]Post-Graduate Program in Materials Science and Engineering, Federal University of Pelotas, 96010-610, Pelotas, RS, Brazil

[b]Post-Graduate Program in Physics, Federal University of Pelotas, 96160-000, Capão do Leão, RS, Brazil

[c]Functional Materials Development Center, São Carlos Federal University, 13565-905, São Carlos, SP, Brazil

[d]Spectroscopy Laboratory, Federal University of Pampa, 96413-172, Bagé, RS, Brazil

[e]Post-Graduate Program in Materials Science and Technology, São Paulo State University, 17033-360, Bauru, SP, Brazil

[f]Department of Physics, São Paulo State University, 17033-360, Bauru, SP, Brazil

*Corresponding author: daiane.fg.eng@outlook.com

A B S T R A C T

In this paper, we synthesized $NaNbO_3$ rods with Al(III) (0.00, 0.05 and 0.1 mmol) by the microwave-assisted hydrothermal method and evaluated the influence of doping on photocatalytic activity. The diffractograms reveal the coexistence of two orthorhombic space groups (P21ma and Pbma) for all samples, with the fraction of each varying with the doping concentration. The micrographs show that pure $NaNbO_3$ exhibits a rod-like shape (diameter of ~200 nm and a length on the order of tens of micrometers). Doping did not induce significant morphological changes; however, the appearance of some cubic grains of varying sizes was observed. The bandgap of the doped samples (3.23 eV) was reduced compared to the pure sample (3.32 eV). The doped samples exhibited superior photocatalytic activity, as evidenced by the removal of the dye Rhodamine B (RhB). The sample containing 0.1 mmol of the impurity ion showed the best photocatalytic discoloration result, achieving 100% RhB removal in 45 minutes. The reduced bandgap, greater ability to absorb light, and the lower electron-hole recombination rate (as revealed by photoluminescence emission) contributed to the enhanced photocatalytic performance of the doped samples. Therefore, this study provides a new a reference for future investigations into $NaNbO_3$ doping for photocatalytic applications.

Keywords: sodium niobate, rods, Al-doping, photocatalysis.

1. Introduction

The contamination of water has become a global problem, given the importance of this natural resource for sustaining life on Earth. Several approaches for water purification have been proposed, including heterogeneous photocatalysis [1-3]. The photocatalytic process involves the activation of a semiconductor by photons. Electrons are promoted from the valence band (VB) to the conduction band (CB), thus forming electron/hole pairs (e^-/h^+). These charge carriers can directly oxidize/reduce various pollutants and also generate reactive species, which subsequently react with the substance of interest [1-3]. Doping has emerged as an effective strategy to enhance the performance of photocatalysts [4-14]. Controlled incorporation of impurity ions can reduce the bandgap, thereby decreasing the energy required to generate e^-/h^+ pairs. Furthermore, it can delay the recombination of photogenerated charges due to the formation of intermediate energy levels, thus improving photocatalytic activity.

Sodium niobate ($NaNbO_3$) is a semiconductor that has proven to be highly efficient as a photocatalyst to degrade various contaminants [1,2,15-17]. In particular, presents an interesting grain growth mechanism. Under hydrothermal conditions a metastable phase of sodium hexaniobate ($Na_2Nb_2O_6{\cdot}H_2O$) wires initially forms [18-22]. As the synthesis progresses, nucleation of cubic crystals occurs on the wires through Ostwald ripening process, transforming the shape particles [19,22]. However, the calcination of this $Na_2Nb_2O_6{\cdot}H_2O$ phase allows the formation of one-dimensional $NaNbO_3$ [18,22] with superior photocatalytic activity when compared to cubes [22-24]. Regarding the doping of the $NaNbO_3$, studies are primarily focused on structural and luminescent analyses [25-33]. Few studies have explored the photocatalytic activity [34-38], highlighting the potential for exploring a broad range of ions. Notably, studies on doping semiconductors with aluminum (Al) ions show encouraging results, with the additional benefit of the low cost of this metal [5-14].

Considering the above, we synthesized $NaNbO_3$ rods with Al(III) (0.00, 0.05 and 0.10 mmol) by the microwave-assisted hydrothermal technique. The impact of doping on photocatalytic activity was evaluated by the removal of Rhodamine B (RhB) dye. The results obtained were very promising and demonstrate that $NaNbO_3$ doped with Al(III) presents good prospects for photocatalytic applications.

2. Experimental methods

2.1. Synthesis

Pure $NaNbO_3$ (SN) was synthesized based on previous studies, with modifications [1-3]. First, 10 g of NaOH (Merck, 99.0%) was dissolved in distilled water, and 1 g of Nb_2O_5 (supplied by CBMM) was added, followed by magnetic stirring at room temperature. The solution was then heated to 150 °C in an adapted-microwave (800 W) for 105 min. The resulting solid was washed with distilled water until neutral pH, and dried at 90 °C overnight. The final powder was calcined at 550 °C for 2 h. For the doped samples, $Al(NO_3)_2 \cdot 9H_2O$ (Sigma-Aldrich, 97.0%) was added to the precursor solution to obtain 0.05 mmol (SNA1) and 0.1 mmol (SNA2) of Al (III), repeating the same procedure and conditions.

2.2. Characterization

All samples were characterized by X-ray diffraction (XRD) (Ultima IV, RIGAKU) with Cu-Kα radiation (λ=1.5406 Å). Morphological investigations were carried out by scanning electron microscopy (SEM) using a Field Emission Gun-Electron Microscope (Supra 35, ZEISS), operating at 5 kV. Band gap energies were estimated using the Wood/Tauc method through the diffuse reflection spectroscopy by a UV-Vis spectrometer (HR2000 +, OCEAN OPTICS). The photoluminescence (PL) was analyzed using a fluorescence spectrometer (Cary Eclipse, AGILENT), with excitation laser of 260 nm.

2.3. Photocatalytic activity

The photocatalytic activity was evaluated by removing RhB dye (1×10^{-5} M) under UV irradiation (06 lamps of 15 W each, λ = 254 nm). The photocatalyst dosage was 50 mg for 50 mL of dye solution. All samples were stirred for 30 min in the dark to achieve adsorption-desorption equilibrium. The variation in RhB concentration was determined by absorbance, using a UV-Vis spectrophotometer (SP200 UV, BEL PHOTONICS). The removal percentage of RhB was defined by the equation $(C_0 - C)/C_0 \times 100\%$, where C_0 and C are initial and residual RhB concentrations, respectively. The experiments were performed in triplicate.

3. Results and discussion

The XRD patterns (Fig. 1a) indicate the coexistence of two orthorhombic symmetries in all samples, space groups P21ma and Pbma, as according to the crystallographic cards JCPDS 82-606 and JCPDS 33-1270, respectively. This polymorphism is consistent with the literature [39-41]. As observed by Teixeira et al. [39] and Htet et al. [41], the two-phase mixture provided the best fit in structural refinement compared to individual phases. Structural refinement was performed using the Rietveld method (Fig. S1a-c) and the lattice parameters and percentage of each phase are presented in Table 1. Gouget et al. [40] reported that crystallization at low temperatures (600 °C) favors the acentric P21ma phase, while higher temperatures (below 950 °C) promote the formation of the centrosymmetric Pbma structure. All samples were crystallized at the same temperature (550 °C), and it was observed that the phase ratio varies among the samples. This suggests that the lattice structure of $NaNbO_3$ may be influenced by doping with Al(III), possibly due to charge compensation. This finding opens up a range of possibilities for future research with other impurity ions.

The SEM micrographs are shown in Fig. 1b-d. The SN sample has rod-like shape, with an average diameter of approximately 200 nm and lengths in the range of tens of micrometers. Although the incorporation of the dopant did not induce significant morphological changes, largely preserving the rod-like shape, the emergence of some cubic grains of varying sizes was observed. This result indicates that Al(III) may have exerted a catalytic effect, accelerating particle coalescence through the Ostwald ripening process. In the study by Valzan et al. [42] using Zr as dopant, an inverse effect was observed, where Zr delayed the coalescence of particles. Initially, the sample exhibited a cubic morphology, which transformed into wire-like structures as the concentration of the impurity ion increased.

The photocatalytic experiment (Fig. 2a) showed that the doped samples showed higher activity, indicating that the doping was highly beneficial. After 45 minutes of light irradiation, the percentages of dye removal by the action of photocatalysts SN, SNA1 and SNA2 were 57%, 87% and 100%, respectively. To understand the photocatalytic mechanism, an experiment with radical scavengers was conducted using the SNA2 photocatalyst (Fig. 2b). In the presence of isopropanol (C_3H_8O), a typical hydroxyl radical (•OH) scavenger, and disodium ethylenediaminetetraacetate

(EDTA), h^+ scavenger, the dye removal decreased to 10% and 25%, respectively. This suggests that •OH and h^+ are crucial active species. In contrast, the presence of silver nitrate ($AgNO_3$) had no effect on discoloration, suggesting that e^- are not directly active species in the photocatalytic reaction. Additionally, a reuse experiment was conducted with the SNA2 sample. After three consecutive cycles, no significant decrease in photocatalytic activity was observed. This indicates that the photocatalyst can be considered stable.

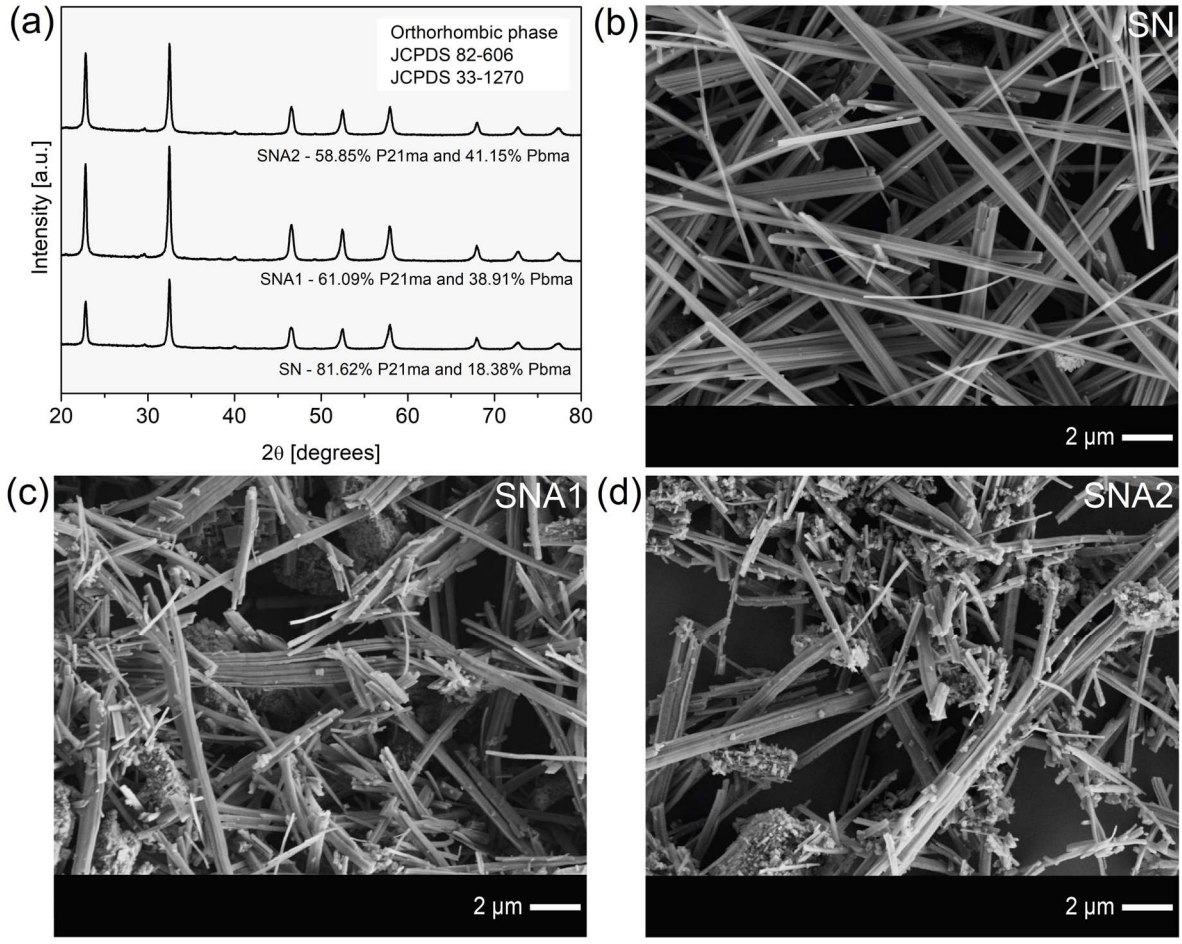

Figure 1. (a) XRD patterns and (b-d) SEM images.

Table 1

Structural parameters from Rietveld refinement.

P21ma			
Parameters	**SN**	**SNA1**	**SNA2**
Wt% phase	81.62	61.09	58.85
a [Å]	5.54136	5.55417	5.56196
b [Å]	7.78181	7.77939	7.78260
c [Å]	5.51198	5.51265	5.50417
V [Å^3]	237.687	238.191	238.257
χ^2	1.96	1.88	1.67
Pbma			
Parameters	**SN**	**SNA1**	**SNA2**
Wt% phase	18.38	38.91	41.15
a [Å]	5.57206	5.51671	5.51193
b [Å]	15.54886	15.57152	15.55821
c [Å]	5.50672	5.51456	5.54190
V [Å^3]	477.098	473.721	475.249
χ^2	1.96	1.88	1.67

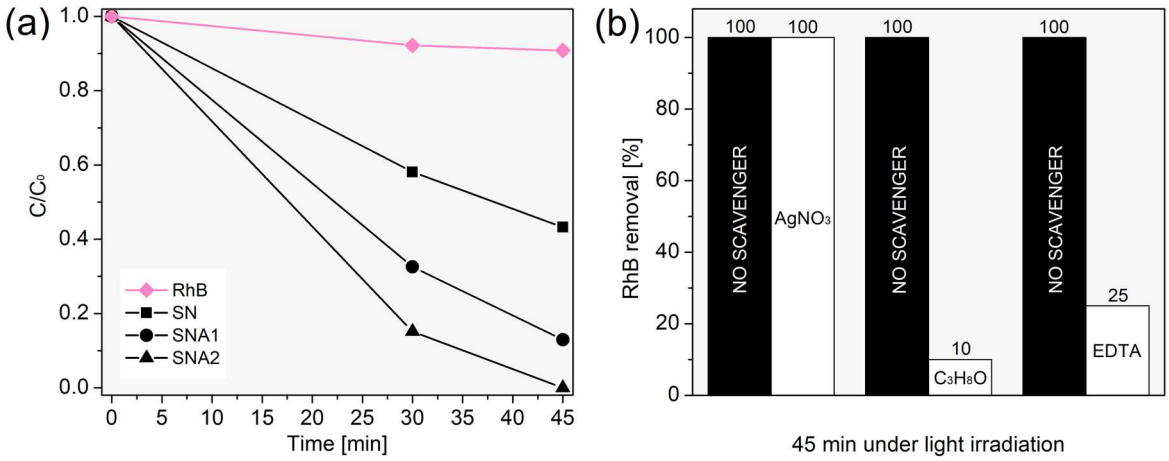

Figure 2. (a) Photocatalytic activity and (b) Experiment of active species.

All samples show strong absorption in the UV region (Fig. 3a), referring to the electronic transitions from the O2p orbitals in the valence band to the Nb4d orbitals in the conduction band [40]. In the doped samples, a slight red shift is observed, indicating that the photocatalysts can be excited with lower light energy, which is highly beneficial for photocatalytic processes. In addition, the increase in the doping concentration gradually led to improved light absorption capabilities. This explains the greater activity of the SNA1 and SNA2 samples. The inset shows the estimated band gap energies, where the SN exhibits a band gap of 3.32 eV, while the doped samples of approximate 3.23 eV. The band gap reduction can be attributed to the difference in valence between the metal ions, which introduces intermediate electronic states. Additionally, the presence of dopants can cause distortions in the crystal lattice, which also affects the overlap of the orbitals and, consequently, the energy of the optical gap. This behavior has also been observed in others doping studies with Al(III) [9,10,12,14].

The photoluminescence analysis (PL) is shown in Fig. 3b-c. The observed emissions are similar across all samples and suggest that recombination occurs through a multiphoton process, with main contributions in the blue and green regions. These emissions are associated with levels of surface and deep defects, respectively [43]. The photoluminescence emission is directly related to the recombination velocity of the e^-/h^+ pairs, where a lower emission indicates a lower recombination rate of the photogenerated charges [4,5,13,14]. Generally, this is correlated with an increase in photocatalytic activity, as it indicates that the e^-/h^+ pairs have more time to participate in oxidation-reduction reactions. This behavior was observed in this study, as evidenced by the reduction in blue emission intensity. Therefore, doping at these concentrations was able to reduce the recombination rate of photogenerated charges at surface levels, resulting in greater photocatalytic activity.

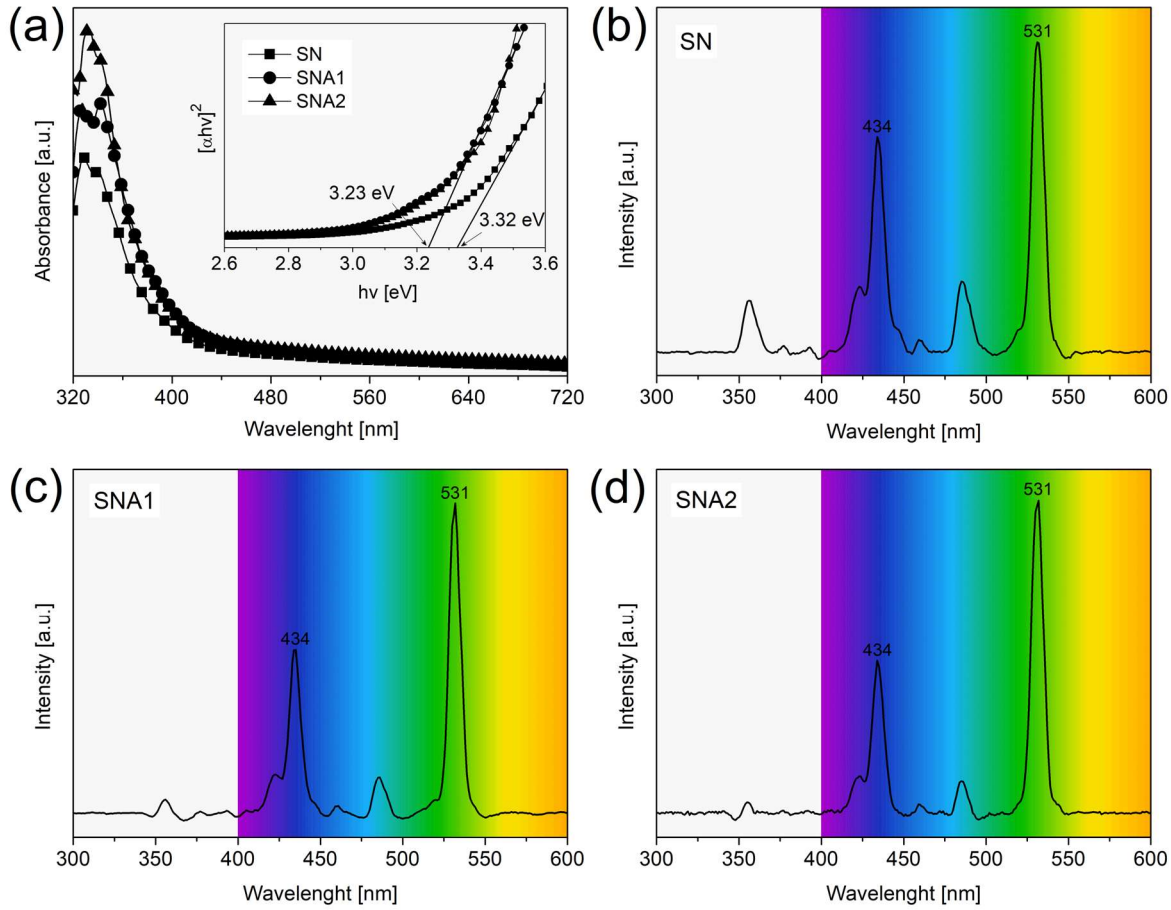

Figure 3. (a) Band gap and (b-d) PL emission.

4. Conclusions

$NaNbO_3$ rods with Al(III) (0.00, 0.05, and 0.1 mmol) were prepared using the microwave-assisted hydrothermal synthesis. All samples exhibited two orthorhombic space groups, with doping altering the proportion of each phase. In contrast, doping did not significantly alter the shape or size of the grains. As the concentration of Al(III) increased, an enhancement in photocatalytic activity was observed. This improvement can be attributed to the reduced recombination of photogenerated charge carriers, decrease in the optical gap, and greater ability to absorb light. In conclusion, this study demonstrated that doping $NaNbO_3$ with Al(III) was highly beneficial for photocatalytic activity. Thus, we hope that this research will serve as a new reference to expand investigations into the doping of $NaNbO_3$ for photocatalytic purposes.

Acknowledgments

The authors thank Companhia Brasileira de Metalurgia e Mineração (CBMM), Núcleo de Apoio à Pesquisa em Ciência e Engenharia de Materiais (NAPCEM-UNIFESP Campus São José dos Campos), and Rorivaldo Camargo from the Laboratório Interdisciplinar de Eletroquímica e Cerâmica (LIEC) at the Universidade Federal de São Carlos for the micrographs obtained. This research received support from Coordenação de Aperfeiçoamento de Pessoal de Nível Superior (CAPES), Conselho Nacional de Desenvolvimento Científico e Tecnológico (CNPq - Process nº 406160/2023-6, nº 406311/2023-4 and n° 406193/2022-3 INCT-NAMITEC), Fundação de Amparo à Pesquisa do Estado do Rio Grande do Sul (FAPERGS - Process nº 17/2551-0000889-8 and n° 19/2551-0001974-2), and Fundação de Amparo à Pesquisa do Estado de São Paulo (FAPESP - Process nº 2013/07296-2 and n° 2024/10185-2).

References

[1] D. Fernandes, C. W. Raubach, P. L. G. Jardim, M. L. Moreira, S. S. Cava, Synthesis of NaNbO3 nanowires and their photocatalytic activity, Ceram. Int. 47 (2021) 10185-10188. https://doi.org/10.1016/j.ceramint.2020.12.070.

[2] D. Fernandes, M. M. Ferrer, C. W. Raubach, M.L. Moreira, P. L. G. Jardim, E. C. Moreira, C. F. O. Graeff, S. S. Cava, Fast synthesis of NaNbO3 nanoparticles with high photocatalytic activity for degradation of organic dyes, J. Am. Ceram. Soc.106 (2022) 399-409. https://doi.org/10.1111/jace.18740.

[3] D. Fernandes, C. W. Raubach, M. M. Ferrer, P. L. G. Jardim, C. F. O. Graeff, M. L. Moreira, E. C. Moreira, V. R. Mastelaro, S. S. Cava, NaNbO3/Eumelanin composite: A new photocatalyst under visible light, Ceram. Int. 49 (2023) 7099-7104. https://doi.org/10.1016/j.ceramint.2022.12.094.

[4] C. L. Ücker, V. Goetzke, F. C. Riemke, M. E. Oliveira, N. L. V. Carreno, F. D. P. Morisso, M. D. Teodoro, V. R. Mastelaro, M. L. Moreira, C. W. Raubach, S. S. Cava, The photocatalytic performance of Fe inserted in Nb2O5 obtained by microwave-assisted hydrothermal synthesis: Factorial design of experiments, J. Photochem. Photobiol. A: Chem. 435 (2023) 114294. https://doi.org/10.1016/j.jphotochem.2022.114294.

[5] H. J. Lee, J. H. Kim, S. S. Park, S. S. Hong, G. D. Lee, Degradation kinetics for photocatalytic reaction of methyl orange over Al-doped ZnO nanoparticles, J. Ind. Eng. Chem. 25 (2015) 199-206. http://dx.doi.org/10.1016/j.jiec.2014.10.035.
[6] O. Saber, H. Alomair, M. Abu-Abdeen, A. Aljaafari, Fast Degradation of Green Pollutants Through Nanonets and Nanofibers of the Al-Doped Zinc Oxide, Acta Metall. Sin. (Engl. Lett.). 31 (2018) 533-546. https://doi.org/10.1007/s40195-017-0682-4.
[7] S. Kim, H. Ryou, I. G. Lee, M. Shin, B. J. Cho, W. S. Hwang, Impact of Al doping on a hydrothermally synthesized β-Ga2O3 nanostructure for photocatalysis applications, RSC Adv. 11 (2021) 7338-7346. https://doi.org/10.1039/D1RA00021G.
[8] H. A. Rafaie, N. A. A. M. Nazam, N. I. T. Ramli, R. Mohamed, M. F. Kasim, Synthesis, characterization and photocatalytic activities of Al-doped ZnO for degradation of methyl orange dye under UV light irradiation, J. Aust. Ceram. Soc. 57 (2021) 479-488. https://doi.org/10.1007/s41779-020-00541-6.
[9] J. He, X. Han, H. Xiang, R. Ran, W. Wang, W. Zhou, Z. Shao, Aluminum Cation Doping in Ruddlesden-Popper Sr2TiO4 Enables High-Performance Photocatalytic Hydrogen Evolution, Hydrogen. 3 (2022) 501-511. https://doi.org/ 10.3390/hydrogen3040032.
[10] C. L. Ücker, S. R. Almeida, M. L. Vitale, F. C. Riemke, Mateus M. Ferrer, E. C. Moreira, C. W. Raubach, S. Cava, Photocatalytic performance of Al and Nb-doped TiO2 nanoparticles prepared by microwave-assisted hydrothermal method, Int. J. Appl. Ceram. Technol. 20 (2023) 1963-1977. https://doi.org/10.1111/ijac.14294.
[11] P. Gaffuri, T. Dedova, E. Appert, M. Danilson, A. Baillard, O. Chaix-Pluchery, F. Güell, I. Oja-Acik, V. Consonni, Enhanced photocatalytic activity of chemically deposited ZnO nanowires using doping and annealing strategies for water remediation, Appl. Surf. Sci. 582 (2022) 152323. https://doi.org/10.1016/j.apsusc.2021.152323.
[12] A. F. Abdulrahman, A. N. Abdulqodus, M. A. Almessiere, Biosynthesis of Al-doped ZnO nanoparticles with different Al doping ratio for methylene orange dye degradation activity, Ceram. Int. 49 (2023) 34920-34936. https://doi.org/10.1016/j.ceramint.2023.08.165.

[13] C. Shi, L. Zhang, Z. Shi, Z. Wang, J. Ma, Mechanistic investigation of cellulose regulating the morphology and photocatalytic activity of Al-doped ZnO, Int. J. Biol. Macromol. 228 (2023) 435-444. https://doi.org/10.1016/j.ijbiomac.2022.12.222.
[14] H. Kumar, A. Giri, A. Rai, Photocatalytic degradation of naphthol blue black dye using undoped and Al-doped cobalt ferrite nanoparticles, KJS. 51 (2024) 100208. https://doi.org/10.1016/j.kjs.2024.100208.
[15] N. D. Van, Template-free synthesis and photocatalytic activity of {0 0 1}-facets exposed rhombohedral Nanbo3 microcrystals, Ceram. Int. 44 (2018) 19945-19949. https://doi.org/10.1016/j.ceramint.2018.07.260.
[16] U. Farooq, R. Phul, S. M. Alshehri, J. Ahmed, T. Ahmad, Electrocatalytic and enhanced photocatalytic applications of sodium niobate nanoparticles developed by citrate precursor route, Sci Rep. 9 (2019) 4488. https://doi.org/10.1038/s41598-019-40745-w.
[17] J. Wu, W. Li, S. Guan, X. Chen, H. Gao, X. Liu, Study on the performance of vanadium doped NaNbO3 photocatalyst degradation antibiotics, Inorg. Chem. Commun. 131 (2021) 108669. https://doi.org/10.1016/j.inoche.2021.108669.
[18] T.-Y. Ke, H.-A. Chen, H.-S. Sheu, J.-W. Yeh, H.-N. Lin, C.-Y. Lee, H.-T. Chiu, Sodium niobate nanowire and its piezoelectricity, J. Phys. Chem. C 112 (2008) 8827-8831. https://doi.org/10.1021/jp711598j.
[19] A. J. Paula, M. A. Zaghete, E. Longo, J. A. Varela, Microwave-assisted hydrothermal synthesis of structurally and morphologically controlled sodium niobates by using niobic acid as a precursor, Eur. J. Inorg. Chem 8 (2008) 1300-1308. https://doi.org/10.1002/ejic.200701138.
[20] H. Shi, X. Li, D. Wang, Y. Yuan, Z. Zou, J. Ye, NaNbO3 nanostructures: facile synthesis, characterization, and their photocatalytic properties, Catal. Lett. 132 (2009) 205-212. https://doi.org/10.1007/s10562-009-0087-8.
[21] A. Yu, J. Qian, L. Liu, H. Pan, X. Zhou, Surface sprouting growth of Na2Nb2O6·H2O nanowires and fabrication of NaNbO3 nanostructures with controlled morphologies, Appl. Surf. Sci. 258 (2012) 3490-3496. https://doi.org/10.1016/j.apsusc.2011.08.133.
[22] Q. Liu, L. Zhang, Y. Chai, W.-L. Dai, Facile fabrication and mechanism of single-crystal sodium niobate photocatalyst: insight into the structure features influence on

photocatalytic performance for H2 evolution, J. Phys. Chem. C 121 (2017) 25898-25907. https://doi.org/10.1021/acs.jpcc.7b08819.
[23] H. Shi, T. Wang, J. Chen, C. Zhu, J. Ye, Z. Zou, Photoreduction of Carbon Dioxide Over NaNbO3 Nanostructured Photocatalysts, Catal. Lett. 141 (2011) 525-530. https://doi.org/10.1007/s10562-010-0482-1.
[24] C. Yan, B. Li, J. Wang, A Comparative Study of Photodegradation Behavior Sodium Niobate Nanowires and Microcubes, Key Eng. Mater. 861 (2020) 221-227. https://doi.org/10.4028/www.scientific.net/KEM.861.221.
[25] P. Vlazan, S. Florina Rus, M. Poienar, P. Sfirloaga, The effect of dopant concentrations on the structural, morphological and optical properties of NaNbO3 semiconductor materials, Mater. Sci. Semicond. Process.102 (2019) 104602. https://doi.org/10.1016/j.mssp.2019.104602.
[26] X. Yang, L. Zhao, W. Chen, Z. Liu, X. Fan, S. Tian, X. Xu, J. Qiu, X. Yu, Low-temperature red long-persistent luminescence of Pr3+ doped NaNbO3 with a perovskite structure, J. Lumin. 208 (2019) 290-295. https://doi.org/10.1016/j.jlumin.2018.12.066.
[27] J. F. da Silva, C. Jacinto, A. L. Moura, Giant sensitivity of an optical nanothermometer based on parametric and non-parametric emissions from Tm3+ doped NaNbO3 nanocrystals, J. Lumin. 226 (2020) 117475. https://doi.org/10.1016/j.jlumin.2020.117475.
[28] H. Ji, J. Tang, X. Tang, Z. Yang, H. Zhang, Y. Qian, Enhanced up conversion emissions of NaNbO3:Er3+/Yb3+ nanocrystals via Mg2+ ions doping, Mater. Lett. 302 (2021) 130348. https://doi.org/10.1016/j.matlet.2021.130348.
[29] S. S.A. Gillani, M. N. Ali, T. Hussain, M. Shakil, R. Ahmad, U. Shuaib, A. Zia, Cubic to tetragonal structural phase transformation in NaNbO3 with peculiar Mg and Ca doping and its repercussions on optoelectronic properties, Optik. 247 (2021) 168017. https://doi.org/10.1016/j.ijleo.2021.168017.
[30] R. Nain, R. K. Dwived, Effect of tuning of charge defects by K, Ba, La doping on structural and electrical behaviour of NaNbO3, Mater. Chem. Phys. 306 (2023) 127999. https://doi.org/10.1016/j.matchemphys.2023.127999.
[31] A. Yadav, S. Sahoo, S. Singh, I. P. Raevski, P. M. Sarun, Influence of Mn-doping on the structure, high-temperature dielectric, and conductive properties of NaNbO3

ceramics, Mater. Sci. Eng. B. 297 (2023) 116796. https://doi.org/10.1016/j.mseb.2023.116796.
[32] P. Vlazan, M. Poienar, I. Malaescu, C. N. Marin, C. Casut, P. Sfrloaga, Exploiting the Bi-doping effect on the properties of NaNbO3 perovskite-type materials, Chem. Phys. 579 (2024) 112203. https://doi.org/10.1016/j.chemphys.2024.112203.
[33] C. S. Htet, A. M. Manjon-Sanz, J. Liu, C. Babori, M. Barati, F. P. Marlton, L. Daniel, M. R. V. Jørgensen, A. Pramanick, Local structural mechanism for enhanced energy storage properties in heterovalent doped NaNbO3 ceramics, J. Eur. Ceram. Soc. 44 (2024) 1597-1609. https://doi.org/10.1016/j.jeurceramsoc.2023.10.072.
[34] R. Jana, A. Gupta, R. Choudhary, O. P. Pandey, Influence of cationic doping at different sites in NaNbO3 on the photocatalytic degradation of methylene blue dye, J. Sol-Gel Sci. Technol. 96 (2020)405-415. https://doi.org/10.1007/s10971-020-05365-1.
[35] U. Farooq, J. Ahmed, S. M. Alshehri, Y. Mao, T. Ahmad, Self-Assembled Interwoven Nanohierarchitectures of NaNbO3 and NaNb1−xTaxO3 (0.05 ≤ x ≤ 0.20): Synthesis, Structural, Characterization, Photocatalytic Applications, and Dielectric Properties, ACS Omega 7 (2022) 16952-16967. https://doi.org/10.1021/acsomega.1c07250.
[36] J. Wu, W. Li, S. Guan, X. Chen, H. Gao, X. Liu, Study on the performance of vanadium doped NaNbO3 photocatalyst degradation antibiotics, Inorg. Chem. Commun. 131 (2021). 108669.https://doi.org/10.1016/j.inoche.2021.108669.
[37] H. Shi, Xi. Li, H. Iwai, Z. Zou, J. Ye, 2-Propanol photodegradation over nitrogen-doped NaNbO3 powders under visible-light irradiation, J. Phys. Chem. Solids. 70 (2009) 931-935. https://doi.org/10.1016/j.jpcs.2009.05.002.
[38] A. S. Vig, N. Rani, A. Gupta, O. P. Pandey, Influence of Ca-doped NaNbO3 and its heterojunction with g-C3N4 on the photoredox performance, Solar Energy. 185 (2019) 469-479. https://doi.org/10.1016/j.solener.2019.04.088.
[39] G. F. Teixeira, H. S. Seleghini, W. B. Bastos, N. Jacomaci, B. Stojadinovic, Z. Dohcevic-Mitrovic, F. Colmati, M. A. San-Miguel, E. Longo, M. A. Zaghet, On the coexistence of ferroelectric and antiferroelectric polymorphs in NaNbO3 fibers at room temperature, J. Mater. Chem. C. 11 (2023) 5524-5533. https://doi.org/10.1039/D2TC04039E.

[40] G. Gouget, M. Duttine, E. Durand, A. Villesuzanne, V. Rodriguez, F. Adamietz, T. Le Mercier, M.-D. Braida, A. Demourgues, Isolating the Two Room-Temperature Polymorphs of NaNbO3: Structural Features, Optical Band Gap, and Reactivity, ACS Appl. Electron. Mater. 1 (2019) 513-522. https://doi.org/10.1021/acsaelm.8b00125.
[41] C. S. Htet, A. M. Manjon-Sanz, J. Liu, C. Babori, M. Barati, F. P. Marlton, L. Daniel, M. R. V. Jørgensen, A. Pramanick, Local structural mechanism for enhanced energy storage properties in heterovalent doped NaNbO3 ceramics, J. Eur. Ceram. Soc. 44 (2024) 1597-1609. https://doi.org/10.1016/j.jeurceramsoc.2023.10.072
[42] P. Vlazan, S. Florina Rus, M. Poienar, P. Sfirloaga, The effect of dopant concentrations on the structural, morphological and optical properties of NaNbO3 semiconductor materials, Mater. Sci. Semicond. Process.102 (2019) 104602. https://doi.org/10.1016/j.mssp.2019.104602.
[43] G. F. Teixeira, E. Silva Junior, A. Z. Simoes, E. Longo, M. A. Zaghete, Unveiling the correlation between structural order-disorder character and photoluminescence emissions of NaNbO3, CrystEngComm, 19 (2017) 4378-4392. https://doi.org/10.1039/C7CE00218A.

Supplementary Material for

Synthesis of Al-doped $NaNbO_3$ rods with enhanced photocatalytic activity

RIETVELD REFINEMENT: Rietveld refinement of the XRD patterns was performed using the FullProf software. The Peak and background profiles were refined according to pseudo-Voigt function.

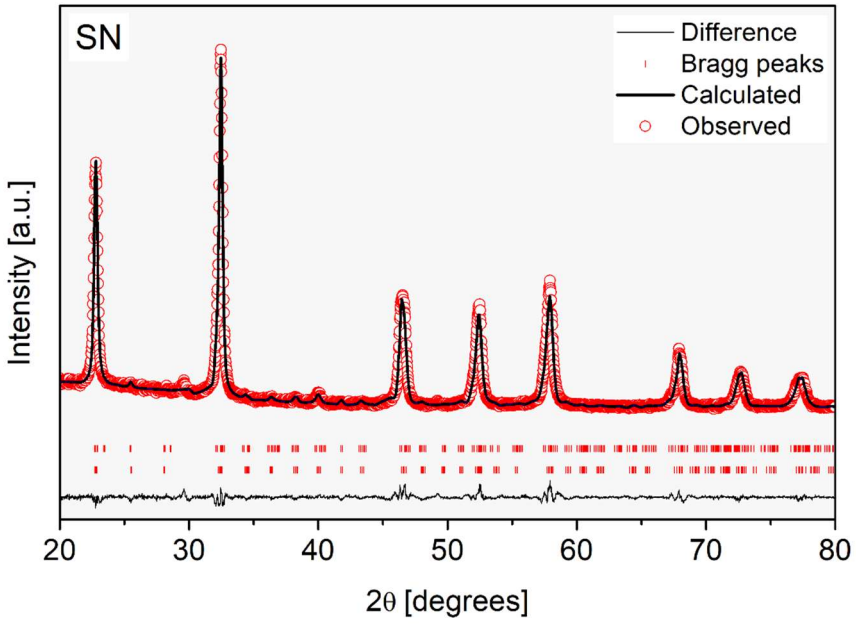

Figure S1-a: SN Rietveld refinement.

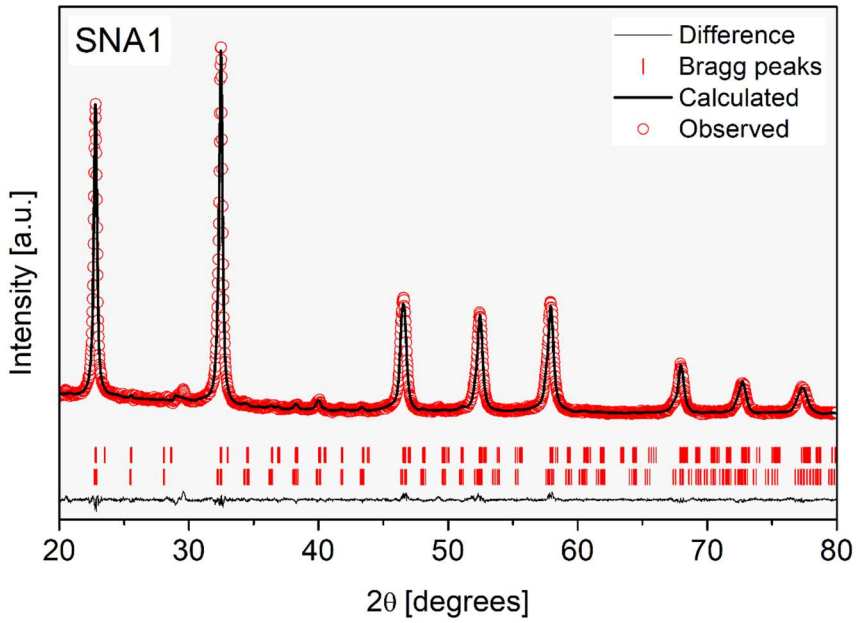

Figure S1-b: SNA1 Rietveld refinement.

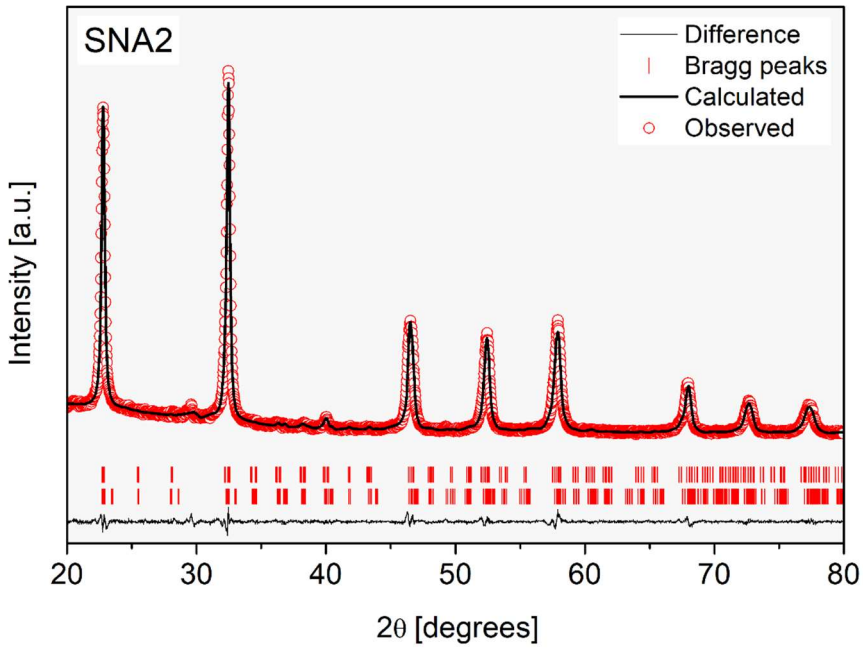

Figure S1-c: SNA2 Rietveld refinement.

3.5 Artigo 5

O artigo intitulado *"Sodium niobate with high photocatalytic activity for the removal of organic dye and inactivation of Escherichia coli, Staphylococcus aureus, and Klebsiella pneumoniae bacteria: the effect of Zn doping on these properties"* é apresentado conforme publicado no periódico *Ceramics International (Online ISSN:1873-3956 and Print ISSN:0272-8842),* classificação A1 na área de Materiais.

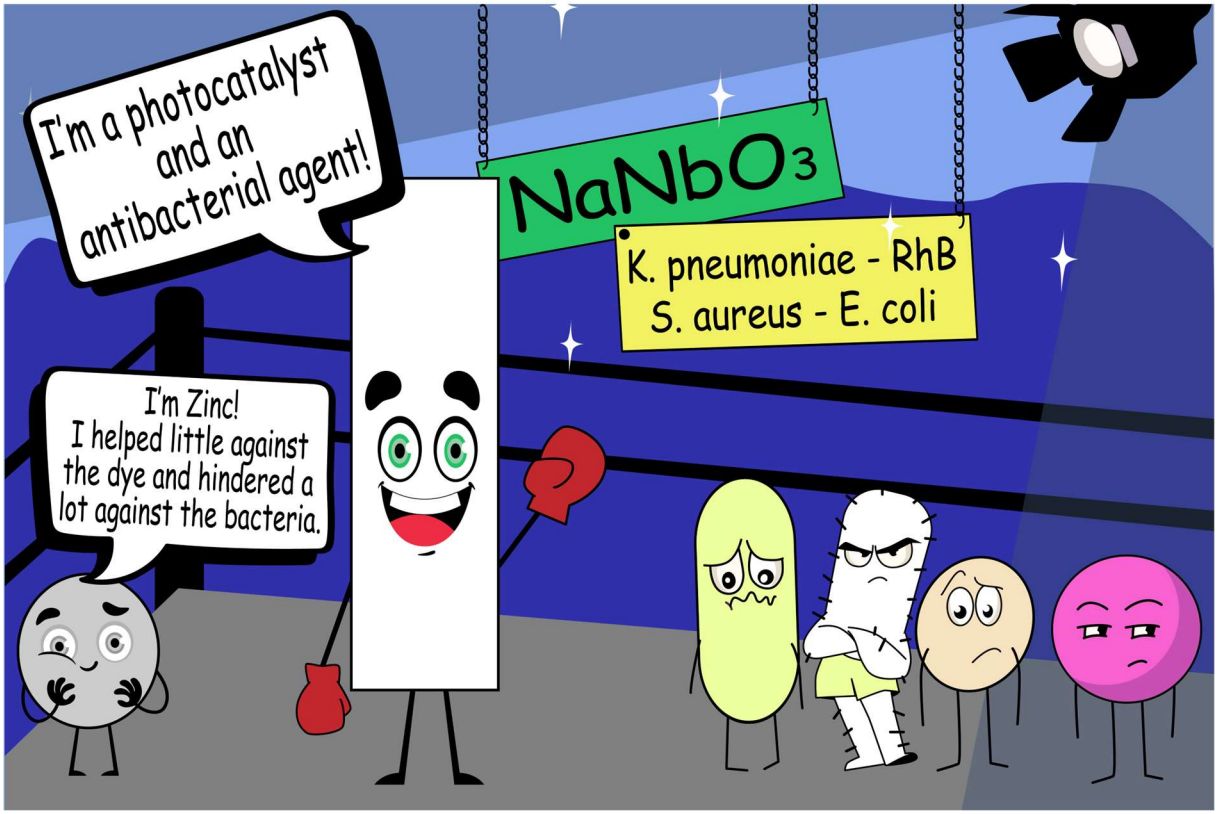

Figura 14 - Resumo gráfico Artigo 5.

Fonte: Elaborado pela autora, 2024.

Sodium niobate with high photocatalytic activity for the removal of organic dye and inactivation of *Escherichia coli, Staphylococcus aureus*, and *Klebsiella pneumoniae* bacteria: the effect of Zn doping on these properties

Daiane Fernandes[a,*], Cristiane Raubach[a], Carla Trassante[b], Vagner Dias[c], Luize Melo[b], Marcelle Silveira[b], Ramon Carvalho[d], Mario Moreira[a,c], Pedro Jardim[a,c], Mateus Ferrer[a], Janice Giongo[b], Rodrigo Vaucher[b], Elson Longo[d], Sergio Cava[a,c]

[a]Post-Graduate Program in Materials Science and Engineering, Federal University of Pelotas, 96010-610, Pelotas, RS, Brazil

[b]Post-Graduate Program in Microbiology and Parasitology, Federal University of Pelotas, 96160-000, Capão do Leão, RS, Brazil

[c]Post-Graduate Program in Physics, Federal University of Pelotas, 96160-000, Capão do Leão, RS, Brazil

[d]Functional Materials Development Center, São Carlos Federal University, 13565-905, São Carlos, SP, Brazil

*Corresponding author: daiane.fg.eng@outlook.com

A B S T R A C T

$NaNbO_3$ doped with Zn (0.00, 0.02, and 0.05 mmol) was synthesized by the microwave-assisted hydrothermal method. Photocatalytic and antibacterial activities were investigated. X-ray diffraction revealed the coexistence of two orthorhombic symmetries (P21ma and Pbma), with doping promoting a progressive increase in the Pbma fraction. All samples exhibited a fiber-like shape (diameter of ~200 nm), which remained unchanged with doping. The low Zn content (0.02 mmol) reduced the band gap energy from 3.08 to 2.95 eV. As a result, this sample exhibited superior photocatalytic activity, achieving 100% RhB dye degradation within 45 min, under UV light. Scavenger tests revealed that hydroxyl radicals, holes, and superoxide radical anions were the main active species involved in the photocatalytic reaction. Additionally, the photocatalyst demonstrated excellent recyclability over three consecutive cycles. Pure $NaNbO_3$ exhibited strong antibacterial activity, completely inhibiting the growth of *S. aureus*, *E. coli*, and *K. pneumoniae* at the tested concentrations. Although the Zn-doped sample also demonstrated antibacterial action, the response was concentration-dependent. This study is the first report on Zn doping in $NaNbO_3$, as well as the first investigation of its antibacterial activity against *K. pneumoniae* and *S. aureus*.

Keywords: sodium niobate, zinc, doping, photocatalysis, antibacterial action.

1. Introduction

Photocatalysis has been recognized as an effective technology for addressing environmental challenges [1]. However, the efficiency of photocatalysts is often limited by their narrow light absorption range and the rapid recombination of photogenerated electron/hole pairs (e^-/h^+). Among the various strategies to overcome these limitations, doping stands out as a promising approach, as it alters the electronic structure of the host material [2,3]. The incorporation of impurity ions can reduce the optical band gap and delay the recombination of charge carriers. As a result, the photocatalytic activity can be substantially improved.

Sodium niobate ($NaNbO_3$) has emerged as a promising photocatalyst [1,2,4,5]. It is thermodynamically stable, resistant to corrosion, and exhibits low toxicity, properties that are particularly attractive for photocatalytic applications. However, studies investigating the influence of doping on its photocatalytic activity remain scarce. Research involving dopants such as N, Ca, Al, K, V, and Ta has been conducted, demonstrating significant improvements in photocatalytic performance [2,6-10]. Despite these advances, no studies to date have explored the use of Zn as a dopant, although it has shown promising results in other semiconductor lattices and offers the additional advantage of low cost [11-13].

Despite the growing interest in antibacterial materials, studies on the use of $NaNbO_3$ for this purpose remain limited. Most existing research focuses on its ability to generate reactive oxygen species under external stimuli, leading to bacterial inactivation. For instance, *E. coli* has been inactivated via photopiezocatalysis using $NaNbO_3$ and $NaNbO_3$/ZnO [14,15], while the $NaNbO_3$/CdS proved effective against *Salmonella* through the pyroelectric effect [16]. Notable results against *E. coli* were also obtained using sintered and polarized $NaNbO_3$ ceramics modified with Ca and Mg ions [17]. In the absence of external stimuli, antibacterial activity against *E. coli* and *S. aureus* was only reported for the $BiFeO_3$/ $NaNbO_3$ composite [18]. In this context, evaluating the antibacterial activity of $NaNbO_3$ through direct interaction with bacteria, without external stimuli, represents a relevant approach. In this context, evaluating the antibacterial activity of $NaNbO_3$ through direct interaction with bacteria, without external stimuli, represents a relevant approach. Additionally, exploring whether Zn doping enhances this response is of particular interest, given that Zn ions are recognized for their strong antimicrobial properties [19,20].

In this study, Zn-doped $NaNbO_3$ (0.00, 0.02, and 0.05 mmol) was synthesized to investigate the effects of Zn incorporation on its photocatalytic and antibacterial properties. The photocatalytic activity was evaluated through the degradation of Rhodamine B (RhB), an industrial dye known for its high toxicity, resistance to degradation, and carcinogenic and mutagenic effects on biodiversity [21-23]. The antibacterial activity was investigated against clinically relevant bacteria: *Klebsiella pneumoniae (K. pneumoniae), S. aureus, and E. coli.*

2. Experimental

2.1. Synthesis

NaOH (Merck, 99.0%), N_2bO_5 (donated by CBMM), and $Zn(NO_3)_2{\cdot}6H_2O$ (Sigma-Aldrich,97.0%) were used as precursor materials. The synthesis of the samples was based on a previously reported methodology, with some modifications [2]. Briefly, an aqueous solution containing NaOH, N_2bO_5, and varying concentrations of Zn ions was prepared. This solution was transferred to a reaction cell coupled to an adapted-microwave (800 W, 2.45 GHz) and heated at 150 °C for 90 min. The resulting solid was washed several times, dried overnight at 90 °C, and calcined at 550 °C for 2 h. The samples were designated as SN (undoped), SNZ1 (0.02 mmol), and SNZ2 (0.05 mmol).

2.2. Characterization

X-ray diffraction (XRD) analysis was performed using a diffractometer (Ultima IV, RIGAKU) with Cu-Kα radiation (λ=1.5406 Å). Morphological characterization was carried out by scanning electron microscopy (SEM) using a Field Emission Gun-Electron Microscope (Supra 35, ZEISS), operating at 5 kV. UV-Vis diffuse reflectance was recorded using a UV-vis spectrophotometer (HR2000+, OCEAN OPTICS), and the band gap energy was estimated using the Wood/Tauc equation.

2.3. Photocatalytic activity

The photocatalytic experiment was conducted under UV lamps (6x15 W, λmax=254 nm). Firstly, 50 mg of photocatalyst was stirred in 50 mL of RhB dye ($1x10^{-5}$ $mol.L^{-1}$) under dark conditions for 30 min to achieve adsorption-desorption equilibrium. An adsorption experiment was performed (Fig. S1). Subsequently, the

solution was exposed to light, and aliquots were collected at specific time intervals. The aliquots were analyzed by measuring the absorbance at 554 nm, which corresponds to the maximum absorption wavelength of RhB, using a UV-Vis spectrophotometer (SP200 UV, BEL PHOTONICS). The removal efficiency of RhB was calculated using the C/C_0 ratio, where C_0 and C represent the initial and residual concentrations of RhB, respectively. In the reuse test, the ratio between the photocatalyst and the dye solution was maintained at 1 mg/1 mL. The experiments to determine the active species were conducted using disodium ethylenediaminetetraacetate (EDTA), isopropyl alcohol (C_3H_8O), silver nitrate ($AgNO_3$), and p-benzoquinone ($C_6H_4O_2$) as scavengers of h^+, •OH (hydroxyl radical), e^-, and $•O_2$- (superoxide radical anion), respectively.

2.4. Antibacterial activity

Strains of *K. pneumoniae* (ATCC 10031), *S. aureus* (ATCC 25923), and *E. coli* (ATCC 25922) were grown on Mueller-Hinton (MH) agar for 24 h at 37 °C. The samples were diluted in dimethyl sulfoxide (DMSO) and then added to MH medium at concentrations of 2.5 mg/mL and 1.25 mg/mL. The prepared medium was immediately dispensed into sterile Petri dishes. The bacterial strains were then subcultured on MH agar and incubated for 24 h at 37 °C in the presence of the medium containing different sample concentrations. For the negative control, only MH medium was used, and for the positive control, the bacteria were inoculated in MH medium without the addition of samples. After the incubation period, colony-forming units (CFU) were counted and converted to log CFU/mL for graphical analysis. Data are expressed as mean ± standard deviation from duplicate measurements. Means were compared using two-way analysis of variance (ANOVA), followed by Dunnett's multiple comparison test. $p \leq 0.05$ indicated a statistically significant difference.

3. Results and discussion

3.1. Structural analysis (XRD and SEM)

XRD patterns (Fig. 1a) show the coexistence of two orthorhombic symmetries, corresponding to the space groups P21ma and Pbma (JCPDS82-606 and JCPDS33-1270, Fig. 1b). This polymorphism is consistent with the literature [2,24-26]. The acentric P21ma phase is favored under low-temperature crystallization conditions

[25], and indeed, the undoped sample (SN) exhibited a higher fraction of this symmetry. Upon doping, a progressive increase in the Pbma phase fraction was observed. This evolution can be attributed to the charge disorder introduced into the crystal lattice by the incorporation of the dopant. Such disorder contributes to the formation of 180° twin domains of the P21ma phase, in which the local polarizations are reversed [26]. When these twinned regions are periodically arranged, the resulting average structure corresponds to the centrosymmetric Pbma phase [25,26]. This mechanism is consistent with the findings reported by Htet et al. [26], who observed similar behavior in $NaNbO_3$ doped with Ca/Zr. The structural refinement using the Rietveld method showed good agreement between the theoretical and experimental patterns (Fig. S2a-c), and the corresponding lattice parameters are presented in Table 1.

SEM images (Fig. 1c) reveal that all samples exhibit a fiber-like shape, with an average diameter of ~200 nm and lengths on the order of several tens of micrometers. Doping did not induce significant morphological changes (Fig. 2a–d). This one-dimensional (1D) morphology is obtained through dehydration of the $Na_2Nb_2O_6.H_2O$ phase [1,4] and offers advantages over the typical cubic grain shape of $NaNbO_3$. Due to its greater surface/volume ratio and anisotropy, this 1D structure favors the transport and separation of charges, in addition to providing more active sites for reactions [1,4,5].

3.2. UV-vis analysis

All samples exhibited band gap energies in the UV region (Fig. 2), referring to electronic transitions from O2p orbitals in the VB to Nb4d orbitals in the CB [1]. Among them, the SNZ1 sample showed the lowest band gap, estimated at 2.95 eV. Zn ions have fully filled 3d orbitals, which can easily hybridize with O2p orbitals, shifts the top of the VB towards the Fermi level and a consequent reduction in the band gap [27]. This slight red shift is beneficial for the photocatalytic process, as it means that less energy is required to activate the photocatalyst. However, increasing the doping level (SNZ2) resulted in a band gap of 3.08 eV, approaching that of the undoped sample. This phenomenon may be attributed to the Burstein-Moss effect. The increase in charge carrier density pushes the Fermi level into the CB, thereby increasing the energy required for a photon to induce an electronic transition and consequently

widening the optical band gap [28]. A similar behavior was observed by X et al. upon doping $NaNbO_3$ with Ca [10].

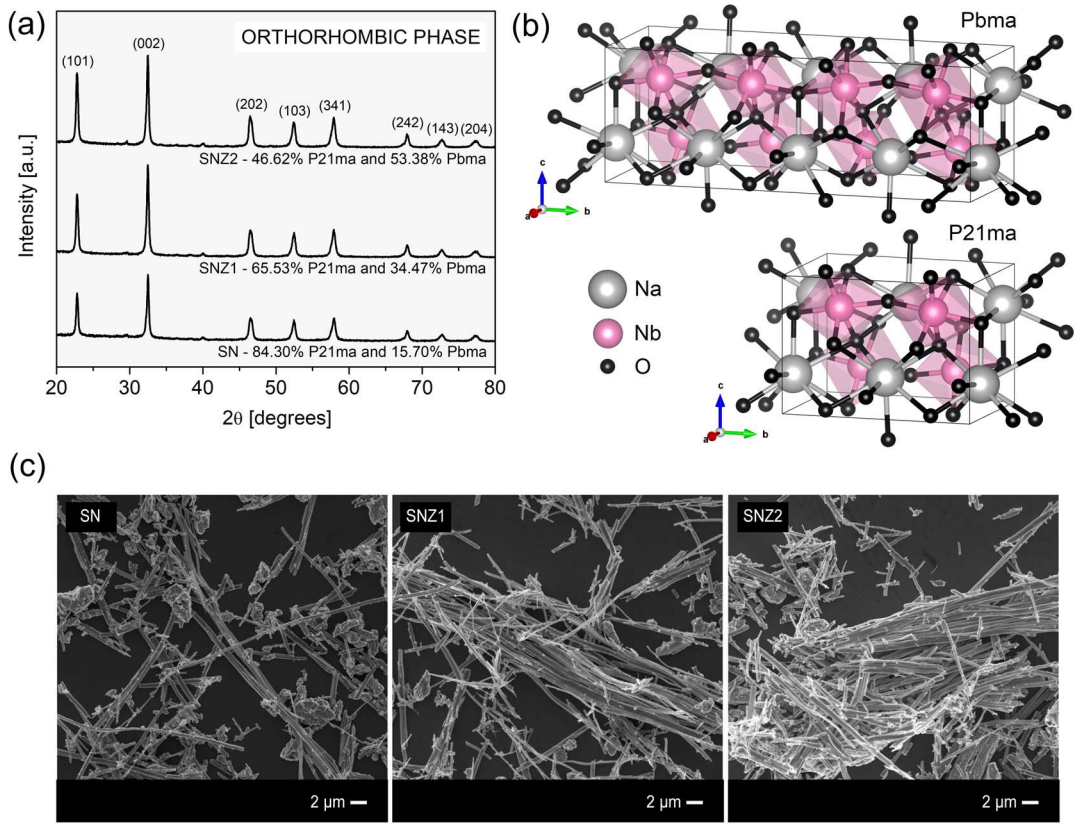

Figure 1. (a) XRD patterns, (b) Crystal structures, and (c) SEM images.

Table 1

Crystallographic data obtained from Rietveld refinement.

Parameters	Symmetry P21ma			Symmetry Pbma		
	SN	SNZ1	SNZ2	SN	SNZ1	SNZ2
Wt% phase	84.30	65.53	46.62	15.70	34.47	53.38
a [Å]	5.54980	5.56708	5.56194	5.54020	5.54498	5.53718
b [Å]	7.78291	7.78730	7.78516	15.61409	15.56814	15.57306
c [Å]	5.50994	5.52073	5.51741	5.48980	5.50514	5.50471
χ^2	1.82	1.81	1.68	1.82	1.81	1.68

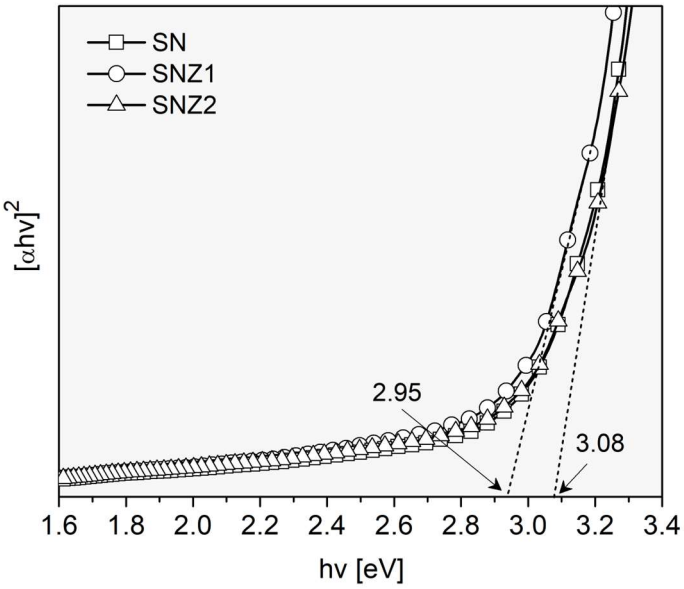

Figure 2. Band gap energies.

3.3. Photocatalytic activity

The SNZ1 sample exhibited superior photocatalytic activity, achieving 100% RhB decolorization within 45 min (Fig. 3a). In comparison, SN and SNZ2 reached approximately 88% removal in the same period. This enhanced response of SNZ1 is attributed to its smaller band gap energy, which reduces the energy required to generation e^-/h^+ pairs. These results indicate that the incorporation of a small concentration of Zn into the $NaNbO_3$ lattice was highly beneficial for improving the photocatalytic performance.

The experiment to determine the active species involved in the photocatalytic process (Fig. 3b) showed that scavenging •OH, h^+, and $•O_2^-$ reduced the RhB removal to 8%, 20%, and 9%, respectively. This demonstrates that these are the key reactive species in the photocatalytic reaction. In contrast, the elimination of e^- did not influence the photocatalytic activity, suggesting that they are not directly involved as active species. Additionally, the SNZ1 sample was tested over three consecutive 45-minute cycles, maintaining a consistent photocatalytic response, which confirms its stability for RhB pollutant degradation.

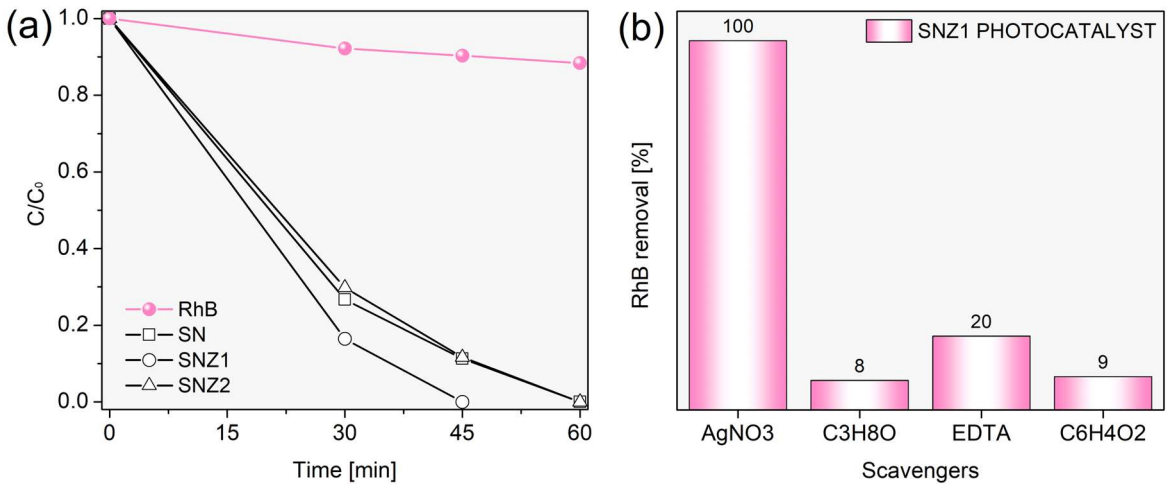

Figure 3. (a) Photocatalytic activity and (b) Scavenger experiment.

3.4. Antibacterial activity

The SN sample exhibited strong antimicrobial activity, completely inhibiting the growth of all bacteria at both concentrations tested (Table 2). The SNZ2 sample also demonstrated antibacterial action, though in a concentration-dependent manner. At 2.50 mg/mL, complete inhibition was observed for all bacteria. However, at 1.25 mg/mL, only *K. pneumoniae* was fully inhibited, while *S. aureus* and *E. coli* showed residual growth values of 3.85 and 4.10 log CFU/mL, respectively. The heightened sensitivity of *K. pneumoniae* may be attributed to its anionic surface, which promotes stronger interactions with Zn ions, increasing its susceptibility to their toxic effects. Although *E. coli* is also a Gram-negative bacterium, structural differences can influence its response to the compound may account for its reduced sensitivity. Interestingly, *S. aureus*, a Gram-positive bacterium, was more easily inhibited than *E. coli*. This is possibly due to the less complex chemical composition of its cell wall, composed predominantly of peptidoglycan [29]. The behavior observed for SNZ2 sample may be associated to the dual role of Zn in bacterial metabolism [30]. At appropriate levels, can act as an enzymatic cofactor, promoting cell growth. However, at high levels its toxic effects prevail. Therefore, the antibacterial efficacy of the doped sample depends not only on the concentration, but also on the biological characteristics of each bacterial strain. Given the pronounced antibacterial action of

$NaNbO_3$, doping with Zn did not lead to any significant improvement under the tested conditions.

Table 2

Bacterial activity.

SN				
Concentration [mg/mL]	Positive control [Log CFU/mL]	*K. pneumoniae* [Log CFU/mL]	*S. aureus* [Log CFU/mL]	*E. coli* [Log CFU/mL]
1.25	5.30	0	0	0
2.50	5.30	0	0	0
SNZ2				
Concentration [mg/mL]	Positive control [Log CFU/mL]	*K. pneumoniae* [Log CFU/mL]	*S. aureus* [Log CFU/mL]	*E. coli* [Log CFU/mL]
1.25	5.30*	0	3.85*	4.10*
2.50	5.30*	0	0	0

Statistical significance was indicated when *$p \leq 0.05$.

4. Conclusions

In conclusion, Zn-doped $NaNbO_3$ samples were successfully synthesized using the microwave-assisted hydrothermal method. Structural analysis confirmed the coexistence of orthorhombic symmetries, with doping progressively altering their fractions without affecting the fiber-like morphology. The photocatalytic activity of $NaNbO_3$ was enhanced by the addition of 0.02 mmol of Zn, which is attributed to a reduction in the band gap. The material exhibited effective degradation of RhB dye under UV light. However, when the Zn content was increased to 0.05 mmol, the band gap widened, reaching a value similar to that of the undoped sample, and the photocatalytic activity remained similar to pure $NaNbO_3$. Antibacterial tests revealed that undoped $NaNbO_3$ exhibits potent antimicrobial activity against *K. pneumoniae*, *S. aureus*, and *E. coli*. The incorporation of Zn introduced a concentration-dependent effect and did not enhance the antibacterial response under the tested conditions,

highlighting the critical role of this ion in bacterial metabolism. As far as we are aware, this is the first report on Zn doping in $NaNbO_3$, as well as the first to explore its antibacterial action against *K. pneumoniae* and *S. aureus*. These findings not only expand the understanding of doping effects on the photocatalytic activity of $NaNbO_3$ but also highlight its potential application in combating pathogenic microorganisms.

Acknowledgments

Companhia Brasileira de Metalurgia e Mineração (CBMM), Núcleo de Apoio à Pesquisa em Ciência e Engenharia de Materiais (NAPCEM-UNIFESP Campus São José dos Campos), Laboratório Interdisciplinar de Eletroquímica e Cerâmica (LIEC-UFSCar), Coordenação de Aperfeiçoamento de Pessoal de Nível Superior (CAPES), Conselho Nacional de Desenvolvimento Científico e Tecnológico (CNPq - Process nº 406160/2023-6, nº 406311/2023-4, and n° 406193/2022-3 INCT-NAMITEC), Fundação de Amparo à Pesquisa do Estado do Rio Grande do Sul (FAPERGS - Process nº 17/2551-0000889-8 and n° 19/2551-0001974-2), and Fundação de Amparo à Pesquisa do Estado de São Paulo (FAPESP - Process nº 2013/07296-2 and n° 2024/10185-2).

References

[1] D. Fernandes, M. M. Ferrer, C. W. Raubach, M. L. Moreira, P. L. G. Jardim, E. C. Moreira, C. F. O. Graeff, S. S. Cava, Fast synthesis of $NaNbO_3$ nanoparticles with high photocatalytic activity for degradation of organic dyes, J. Am. Ceram. Soc.106 (2022) 399-409. https://doi.org/10.1111/jace.18740

[2] D. Fernandes, C. W. Raubach, V. S. Dias, R. D. Carvalho, M. L. Moreira, P. L. G. Jardim, M. M. Ferrer, E. C. Moreira, C. F. O. Graeff, E. Longo, S. S. Cava, Synthesis of Al-doped $NaNbO_3$ rods with enhanced photocatalytic activity, J. Phys. Chem. Solids. 200 (2025) 112607. https://doi.org/10.1016/j.jpcs.2025.112607

[3] K. Sathishkumar, P. Harishsenthil, S. M. Naidu, B. Srividhya, L. Guganathan, K. M. Batoo, M. F. Ijaz, M. Ramamoorthy, S. Ragupathy, Impact of metal doping and non-metal loading on the photocatalytic degradation of organic pollutants using tin dioxide catalyst under sunlight irradiation, J. Mol. Struct. 1321 (2025) 13984. https://doi.org/10.1016/j.molstruc.2024.139841

[4] Q. Liu, L. Zhang, Y. Chai, W.-L. Dai, Facile fabrication and mechanism of single crystal sodium niobate photocatalyst: insight into the structure features influence on photocatalytic performance for H_2 evolution, J. Phys. Chem. C. 121 (2017) 25898-25907. https://doi.org/10.1021/acs.jpcc.7b08819

[5] C. Yan, B. Li, J. Wang, A Comparative Study of Photodegradation Behavior Sodium Niobate Nanowires and Microcubes, Key Eng. Mater. 861 (2020) 221-227. https://doi.org/10.4028/www.scientific.net/KEM.861.221

[6] F. R. Praxedes, M. A. L. Nobre, P. S. Poon, J. Matos, S. Lanfredi, Nanostructured $K_xNa_{1-x}NbO_3$ hollow spheres as potential materials for the photocatalytic treatment of polluted water, Appl. Catal. B: Environ. 298 (2021) 120502. https://doi.org/10.1016/j.apcatb.2021.120502

[7] U. Farooq, J. Ahmed, S. M. Alshehri, Y. Mao, T. Ahmad, Self-Assembled Interwoven Nanohierarchitectures of $NaNbO_3$ and $NaNb_{1-x}Ta_xO_3$ ($0.05 \leq x \leq 0.20$): Synthesis, Structural, Characterization, Photocatalytic Applications, and Dielectric Properties, ACS Omega 7 (2022) 16952-16967. https://doi.org/10.1021/acsomega.1c07250

[8] J. Wu, W. Li, S. Guan, X. Chen, H. Gao, X. Liu, Study on the performance of vanadium doped $NaNbO_3$ photocatalyst degradation antibiotics, Inorg. Chem. Commun. 131 (2021). 108669.https://doi.org/10.1016/j.inoche.2021.108669

[9] H. Shi, Xi. Li, H. Iwai, Z. Zou, J. Ye, 2-Propanol photodegradation over nitrogen-doped $NaNbO_3$ powders under visible-light irradiation, J. Phys. Chem. Solids. 70 (2009) 931-935. https://doi.org/10.1016/j.jpcs.2009.05.002

[10] A. S. Vig, N. Rani, A. Gupta, O. P. Pandey, Influence of Ca-doped $NaNbO_3$ and its heterojunction with g-C_3N_4 on the photoredox performance, Solar Energy. 185 (2019) 469-479. https://doi.org/10.1016/j.solener.2019.04.088

[11] J. A. Joseph, S. B. Nair, S. S. John, S. K. Remillard, S. Shaji, R. R. Philip, Zinc-doped iron oxide nanostructures for enhanced photocatalytic and antimicrobial applications, J. Appl. Electrochem. 51 (2021) 521-538. https://doi.org/10.1007/s10800-020-01512-2

[12] M. Siddique et al., Synthesis, characterization, photocatalytic activity and gas sensing properties of zinc doped manganese oxide nanoparticles, Physica B: Condensed. Matter. 602 (2021) 412504. https://doi.org/10.1016/j.physb.2020.412504

[13] L. V. Thaninki, S. N. Arputharaj, A. Manasai, Facile wet chemical synthesis and characterization of zinc doped gadolinium oxide nanoparticles for enhanced photodegradation of Rhodamine B dye under illumination of UV light, Iran. J. Catal. 12 (2022) 315-336. https://doi.org/10.30495/ijc.2022.1948621.1904

[14] A. Sharma, U. Bhardwaj, D. Jain, H. S. Kushwaha, $NaNbO_3$ Nanorods: Photopiezocatalysts for Elevated Bacterial Disinfection and Wastewater Treatment, ACS Omega. 7 (2022) 7595−7605. https://doi.org/10.1021/acsomega.1c06109

[15] A. Sharma, U. Bhardwaj, D. Jain, H. S. Kushwaha, $NaNbO_3$/ZnO piezocatalyst for non-destructive tooth cleaning and antibacterial activity, iScience. 25 (2022) 104915. https://doi.org/10.1016/j.isci.2022.104915

[16] J. Min, H. Hao, Y. Zhao, Y. Hu, Q. Huang, F. Zhu, G. Zhang, J. Bi, S. Yan, H. Hou, Construction of $NaNbO_3$/CdS nanorods composites with pyroelectric effect for enhanced pyrocatalytic and antibacterial activity under room-temperature cold-hot cycles, Colloids Surf. A: Physicochem. Eng. Asp. 650 (2022) 129529. https://doi.org/10.1016/j.colsurfa.2022.129529

[17] L. Zhang, Y. Yang, Y. Pu, M. Chen, N. Xu, X. Wu, Novel $NaNbO_3$-based, ferroelectric ceramics with excellent polarization and electric potential for antibacterial applications. Mater. Today Phys. 49 (2024) 101583. https://doi.org/10.1016/j.mtphys.2024.101583

[18] R. P. Ummer, S. Perumbilavil, J. Jose, S. Thomas, P. Gopinath, N. Kalarikkal, Exploring the optical limiting, photocatalytic and antibacterial properties of the $BiFeO_3$–$NaNbO_3$ nanocomposite system, RSC Adv. 11 (2021) 8450-8458. https://doi.org/10.1039/D0RA09776D

[19] L. Zuo, Y. Bao, K. Wu, S. Li, Z. Qu, Y Lyu, X. Li, H. Meng, Y. He, Hollow-structured Zn-doped CeO_2 mesoporous spheres boost enhanced antioxidant activity and synergistic bactericidal effect, Colloids Surf. B Biointerfaces. 246 (2025) 114381. https://doi.org/10.1016/j.colsurfb.2024.114381

[20] M. Hassan, A. El-Faham, A. Barakat, M. Haukka, R. Tatikonda, M. A. M. Abu-Youssef, S. M. Soliman, A. Yousri, Synthesis, X-ray Structure, Cytotoxic, and Anti-Microbial Activities of Zn(II) Complexes with a Hydrazono s-Triazine Bearing Pyridyl Arm, Inorganics. 12 (2024) 176. https://doi.org/10.3390/inorganics12070176

[21] T. L. Yusuf, B. O. Orimolade, D. Masekela, B. Mamba, N. Mabuba, The application of photoelectrocatalysis in the degradation of rhodamine B in aqueous

solutions: a review. RSC Advances. 12 (2022) 26176. https://doi.org/10.1039/D2RA04236C

[22] A. K. Al-Buriahi, A. A. Al-Gheethi, P. S. Kumar, R. M. S. R. Mohamed, H. Yusof, A. F. Alshalif, N. A. Khalifa, Elimination of rhodamine B from textile wastewater using nanoparticle photocatalysts: A review for sustainable approaches. Chemosphere. 287 (2022) 132162. https://doi.org/10.1016/j.chemosphere.2021.132162

[23] A. V. Mohod, M. Momotko, N. S. Shah, M. Marchel, M. Imran, L. Kong, G. Boczkaj, Degradation of Rhodamine dyes by Advanced Oxidation Processes (AOPs) – Focus on cavitation and photocatalysis - A critical review. Water Resour. Ind. 30 (2023) 100220. https://doi.org/10.1016/j.wri.2023.100220

[24] G. F. Teixeira, H. S. Seleghini, W. B. Bastos, N. Jacomaci, B. Stojadinovic, Z. Dohcevic-Mitrovic, F. Colmati, M. A. San-Miguel, E. Longo, M. A. Zaghet, On the coexistence of ferroelectric and antiferroelectric polymorphs in $NaNbO_3$ fibers at room temperature, J. Mater. Chem. C. 11 (2023) 5524-5533. https://doi.org/10.1039/D2TC04039E

[25] G. Gouget, M. Duttine, E. Durand, A. Villesuzanne, V. Rodriguez, F. Adamietz, T. Le Mercier, M.-D. Braida, A. Demourgues, Isolating the Two Room-Temperature Polymorphs of $NaNbO_3$: Structural Features, Optical Band Gap, and Reactivity, ACS Appl. Electron. Mater. 1 (2019) 513-522. https://doi.org/10.1021/acsaelm.8b00125

[26] C. S. Htet, A. M. Manjon-Sanz, J. Liu, C. Babori, M. Barati, F. P. Marlton, L. Daniel, M. R. V. Jørgensen, A. Pramanick, Local structural mechanism for enhanced energy storage properties in heterovalent doped $NaNbO_3$ ceramics, J. Eur. Ceram. Soc. 44 (2024) 1597-1609. https://doi.org/10.1016/j.jeurceramsoc.2023.10.072

[27] F. Benlakhdar, M. A. Ghebouli, Z. Zerrougui, K. Bouferrache, Y. Slimani, B. Ghebouli, I. Bouchama, T. Chihi, M. Fatmi, S. A. Mouhammad, N. Algethami, S. Alomairy, Structural, elastic, mechanical and optoelectronic properties of zinc-doped $SrTiO_3$ perovskite compounds, Mod. Phys. Lett. B. 38 (2024) 2350200. https://doi.org/10.1142/S0217984923502007

[28] Z. Zarhri, A. D. Cano, O. Oubram, Y. Ziat, A. Bassam, Optical measurements and Burstein Moss effect in optical properties of Nb-doped $BaSnO_3$ perovskite, Micro and Nanostructures. 166 (2022) 207223. https://doi.org/10.1016/j.micrna.2022.207223

[29] A. Batool, A. Azizullah, K. Ullah, S. Shad, F. U. Khan, M. F. Seleiman, T. Aziz, U. Zeb, reen synthesis of Zn-doped TIO_2 nanoparticles from Zanthoxylum armatum, BMC Plant Biology. 24 (2024) 820. https://doi.org/10.1186/s12870-024-05525-3
[30] J. D. Helmann, Metals in Motion: Understanding Labile Metal Pools in Bacteria, Biochemistry. 64 (2025) 329-345. https://doi.org/10.1021/acs.biochem.4c00726

Supplementary Material for

Sodium niobate with high photocatalytic activity for the removal of organic dye and inactivation of *Escherichia coli*, *Staphylococcus aureus*, and *Klebsiella pneumoniae* bacteria: the effect of Zn doping on these properties

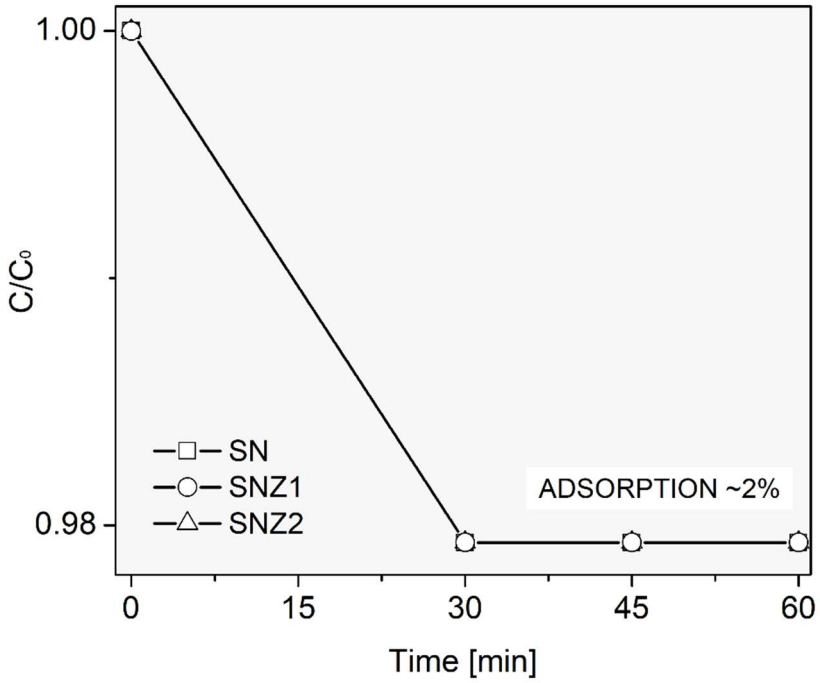

Figure S1: Adsorption experiment.

RIETVELD REFINEMENT: Rietveld refinement of the XRD patterns was performed using the FullProf software. The Peak and background profiles were refined according to pseudo-Voigt function.

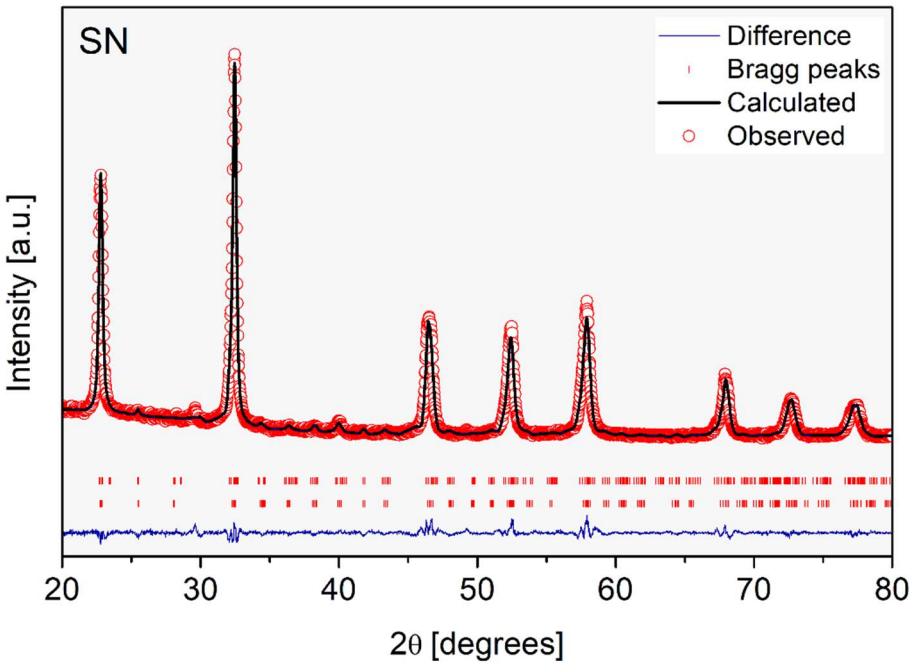

Figure S2-a: SN Rietveld refinement.

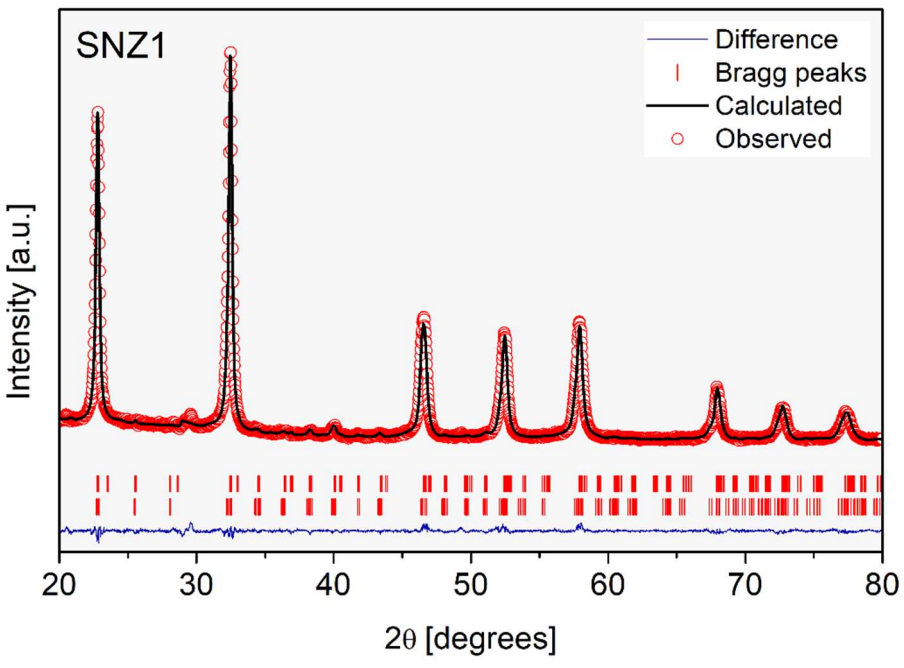

Figure S2-b: SNA1 Rietveld refinement.

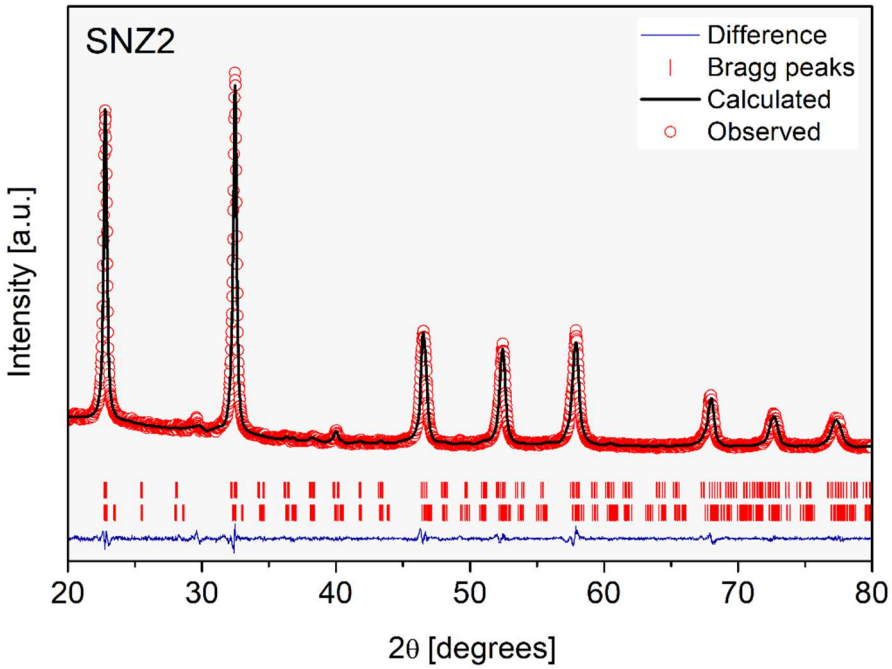

Figure S2-c: SNA2 Rietveld refinement.

4 Considerações finais

Esta tese foi construída a partir de cinco artigos científicos que investigaram o uso do $NaNbO_3$, uma perovskita livre de chumbo, como fotocatalisador e agente antimicrobiano. O desenvolvimento da pesquisa aconteceu de forma progressiva, partindo da síntese de nanofios e nanograos de $NaNbO_3$, passando pela construção de uma heteroestrutura com eumelanina e, por fim, modificações via dopagem com íons metálicos de Cu(II), Al(III) e Zn(II).

No primeiro artigo, foi demonstrado que a síntese hidrotérmica assistida por micro-ondas é uma técnica eficiente para a obtenção de nanofios de $NaNbO_3$, com tempo de síntese inferior aos relatados na literatura. Ademais, o aumento da temperatura de calcinação transformou os nanofios em nanograos, os quais apresentaram desempenho fotocatalítico superior, promovendo a degradação total do corante RhB em aproximadamente 50 minutos. Essa alta eficiência foi atribuída à combinação entre cristalinidade, que reduz a taxa de recombinação dos pares e^-/h^+, e a morfologia dos nanograos, devido à maior proporção de átomos com coordenação incompleta, que os torna mais reativos.

No segundo artigo, foi desenvolvido um fotocatalisador heteroestruturado composto pelos nanograos de $NaNbO_3$, previamente sintetizados, e eumelanina. O compósito exibiu alta atividade fotocatalítica sob luz visível, evidenciada pela degradação total do corante RhB, representando um avanço significativo em termos de aproveitamento energético. A escolha da eumelanina, pigmento abundante na fauna e na flora, se deu por sua capacidade de absorver um amplo espectro de luz, além de ser um material de baixo custo e de fácil extração. Neste estudo, a fonte do pigmento foi resíduo de cabelo humano, que teria como destino o lixo comum. Assim, a reutilização desse material reforça a abordagem desta pesquisa, voltada à remediação ambiental.

Nos três artigos seguintes, a influência da dopagem na rede hospedeira do $NaNbO_3$ 1D foi analisada. A inserção de Cu(II), Al(III) e Zn(II) promoveu alterações na simetria cristalina e influenciou significativamente as propriedades ópticas da perovskita. Em concentrações otimizadas, a dopagem reduziu o *band gap* e a taxa de recombinação das cargas fotogeradas. Isso resultou em uma maior eficiência na degradação do corante RhB, com remoção total em menos de 50 minutos. De acordo

com o estado da arte, não há investigações envolvendo $NaNbO_3$ 1D dopado com esses íons, o que evidencia o ineditismo e a relevância científica desta pesquisa.

Com relação à atividade antimicrobiana, a dopagem com Cu(II) resultou na inibição do crescimento da bactéria *E. coli*, com a ação influenciada pela concentração do íon dopante. Em baixa concentração, o Cu(II) possivelmente atuou como cofator enzimático, favorecendo o crescimento bacteriano, enquanto que em concentrações mais elevadas o efeito tóxico foi predominante. No estudo com Zn(II), o $NaNbO_3$ apresentou atividade antibacteriana expressiva contra *E. coli*, *S. aureus* e *K. pneumoniae*. Embora o material dopado também tenha exibido ação antibacteriana, sua resposta foi inferior à do material não dopado. Esse comportamento pode ser atribuído ao papel duplo do Zn(II), atuando como cofator ou agente tóxico. Além disso, nenhuma pesquisa anterior havia reportado a atividade antibacteriana do $NaNbO_3$, sem estímulo adicional, contra *E. coli*, assim como não foram encontrados estudos sobre sua ação contra *K. pneumoniae* e *S. aureus*, evidenciando que esta pesquisa pode contribuir de forma significativa para a comunidade científica.

Dessa forma, os resultados obtidos nesta tese demonstraram o grande potencial do $NaNbO_3$, como fotocatalisador para a purificação de águas residuais, além de sua atuação como agente antimicrobiano. A dopagem e a formação de heteroestruturas mostraram-se abordagens eficazes para aprimorar a atividade fotocatalítica. A perovskita também apresentou boa estabilidade nos testes de reutilização realizados nos experimentos fotocatalíticos, característica importante para aplicações práticas.

Como perspectivas futuras, há a possibilidade de desenvolver compósitos utilizando eumelanina extraída de outras fontes. Existe também uma vasta gama de íons dopantes que ainda podem ser investigados, bem como a atividade fotocatalítica do $NaNbO_3$ frente a outros tipos de contaminantes. Outra linha de pesquisa promissora são estudos mais aprofundados sobre os mecanismos envolvidos na inativação bacteriana, assim como a análise do desempenho da perovskita frente a outros patógenos, como fungos, por exemplo.

Referências

[1] TEO, S. H. et al. Sustainable toxic dyes removal with advanced materials for clean water production: A comprehensive review. **Journal of Cleaner Production**, v. 332, p. 130039, 2022.

[2] ISAEV, A. B. et al. Electrochemical oxidation of azo dyes in water: a review. **Environmental Chemistry Letters**, v. 21, p. 2863-2911, 2023.

[3] ALI, A. E. et al. Removal of Azo Dyes from Aqueous Effluent Using Bio-Based Activated Carbons: Toxicity Aspects and Environmental Impact. **Separations**, v. 10, p. 506, 2023.

[4] YUSUF, T. L. et al. The application of photoelectrocatalysis in the degradation of rhodamine B in aqueous solutions: a review. **RSC Advances**, v. 12, p. 26176, 2022.

[5] AL-BURIAHI, A. K. et al. Elimination of rhodamine B from textile wastewater using nanoparticle photocatalysts: A review for sustainable approaches. **Chemosphere**, v. 287, p. 132162, 2022.

[6] MOHOD, A. V. et al. Degradation of Rhodamine dyes by Advanced Oxidation Processes (AOPs) – Focus on cavitation and photocatalysis - A critical review. **Water Resources and Industry**, v. 30, p. 100220, 2023.

[7] DESHMUKH, N. S.; DEOSARKAR, M. P. A review on ultrasound and photocatalysis-based combined treatment processes for pesticide degradation. **Materials Today: Proceedings**, v. 57, p. 1575-1584, 2022.

[8] GONZAGA, I. M. D.; ALMEIDA, C. V. S.; MASCARO, L. H. A Critical Review of Photo-Based Advanced Oxidation Processes to Pharmaceutical Degradation. **Catalysts**, v. 13, p. 221, 2023.

[9] ÜCKER, C. L. et al. Influence of Nb_2O_5 crystal structure on photocatalytic efficiency. **Chemical Physics Letters**, v. 764, p. 138271, 2021.

[10] KHAN, S. et al. Photocatalytic Dye Degradation from Textile Wastewater: A Review. **ACS Omega**, v. 9, p. 21751-21767, 2024.

[11] VINAYAGAM, V. et al. Recent developments on advanced oxidation processes for degradation of pollutants from wastewater with focus on antibiotics and organic dyes. **Environmental Research**, v. 240, p. 117500, 2024.

[12] ÜCKER, C. L. et al. Multi-Photonic behavior of Nb_2O_5 and its correlation with synthetic methods. **Journal of Materials Science**, v. 56, p. 7889-7905, 2021.

[13] BAEISSA, E. S. Photocatalytic degradation of malachite green dye using Au/$NaNbO_3$ nanoparticles. **Journal of Alloys and Compounds**, v. 672, p. 564-570, 2016.

[14] CHEN, S. et al. Preparation and characterization of direct Z-scheme photocatalyst Bi_2O_3/$NaNbO_3$ and its reaction mechanism. **Applied Surface Science**, v. 292, p. 357-366, 2014.

[15] WENG, B. et al. Photocorrosion Inhibition of Semiconductor-Based Photocatalysts: Basic Principle, Current Development, and Future Perspective. **ACS Catalysis**, v. 9, p. 4642-4687, 2019.

[16] ÜCKER, C. L. et al. Photocatalytic performance of Al and Nb-doped TiO_2 nanoparticles prepared by microwave-assisted hydrothermal method. **International Journal of Applied Ceramic Technology**, v. 2, p. 1963-1977, 2023.

[17] ÜCKER, C. L. et al. The photocatalytic performance of Fe inserted in Nb_2O_5 obtained by microwave-assisted hydrothermal synthesis: Factorial design of experiments. **Journal of Photochemistry and Photobiology A: Chemistry**, v. 435, p. 114294, 2023.

[18] SATHISHKUMAR, K. et al. Impact of metal doping and nonmetal loading on the photocatalytic degradation of organic pollutants using tin dioxide catalyst under sunlight irradiation. **Journal of Molecular Structure**, v. 1321, p. 139841, 2025.

[19] ÜCKER, C. L. et al. Study of $CaTiO_3$–ZnS heterostructure obtained by microwave-assisted solvothermal synthesis and its application in photocatalysis. **Journal of Physics and Chemistry of Solids**, v. 172, p. 111050, 2023.

[20] MADKHALI, N. et al. Recent update on photocatalytic degradation of pollutants in waste water using TiO_2-based heterostructured materials. **Results in Engineering**, v. 17, p. 100920, 2023.

[21] LI, P. et al. The effects of crystal structure and electronic structure on photocatalytic H_2 evolution and CO_2 reduction over two phases of perovskite-structured $NaNbO_3$. **The Journal of Physical Chemistry C**, v. 116, p. 7621-7628, 2012.

[22] LIU, Q. et al. Facile fabrication and mechanism of single crystal sodium niobate photocatalyst: insight into the structure features influence on photocatalytic performance for H2 evolution. **The Journal of Physical Chemistry C**, v. 121, p. 25898-25907, 2017.

[23] HAMILTON, A. et al. Flux-mediated synthesis and photocatalytic activity of $NaNbO_3$ particles. **Journal of the American Ceramic Society**, v. 103, p. 454-464, 2019.

[24] FRESNO, F. et al. CO_2 reduction over $NaNbO_3$ and $NaTaO_3$ perovskite photocatalysts. **Photochemical & Photobiological Sciences**, v. 16, p. 17-23, 2017.

[25] YANG, B. et al. Enhanced photocatalytic activity of perovskite $NaNbO_3$ by oxygen vacancy engineering. **Physical Chemistry Chemical Physics**, v. 21, p. 11697-11704, 2019.

[26] YAN, C.; LI, B.; WANG, J. A Comparative Study of Photodegradation Behavior Sodium Niobate Nanowires and Microcubes. **Key Engineering Materials**, v. 861, p. 221-227, 2020.

[27] QILIN, G. et al. Rod-like $NaNbO_3$: mechanisms for stable solvothermal synthesis, temperature-mediated phase transitions and morphological evolution. **RSC Advances**, v. 4, p. 15104, 2014.

[28] TEIXEIRA, G. F. et al. Unveiling the correlation between structural order-disorder character and photoluminescence emissions of $NaNbO_3$. **CrystEngComm**, v. 19, p. 4378-4392, 2017.

[29] FERNANDES, D. et al. Fast synthesis of $NaNbO_3$ nanoparticles with high photocatalytic activity for degradation of organic dyes. **Journal of the American Ceramic Society**, v. 106, p. 399-409, 2023.

[30] VLAZAN, P. et al. The effect of dopant concentrations on the structural, morphological and optical properties of $NaNbO_3$ semiconductor materials. **Materials Science in Semiconductor Processing**, v. 102, p. 104602, 2019.

[31] YANG, X. et al. Low-temperature red long-persistent luminescence of Pr^{3+} doped $NaNbO_3$ with a perovskite structure. **Journal of Luminescence**, v. 208, p. 290-295, 2019.

[32] DA SILVA, J. F.; JACINTO, C.; MOURA, A. L. Giant sensitivity of an optical nanothermometer based on parametric and non-parametric emissions from Tm^{3+} doped $NaNbO_3$ nanocrystals. **Journal of Luminescence**, v. 226, p. 117475, 2020.

[33] JI, H. et al. Enhanced up conversion emissions of $NaNbO_3$:Er^{3+}/Yb^{3+} nanocrystals via Mg^{2+} ions doping. **Materials Letters**, v. 302, p. 130348, 2021.

[34] GILLANI, S. S. A. et al. Cubic to tetragonal structural phase transformation in $NaNbO_3$ with peculiar Mg and Ca doping and its repercussions on optoelectronic properties. **Optik**, v. 247, p. 168017, 2021.

[35] R. NAIN, R.; DWIVED, R. K. Effect of tuning of charge defects by K, Ba, La doping on structural and electrical behavior of $NaNbO_3$. **Materials Chemistry and Physics**, v. 306, p. 127999, 2023.

[36] YADAV, A. et al. Influence of Mn-doping on the structure, high-temperature dielectric, and conductive properties of $NaNbO_3$ ceramics. **Materials Science and Engineering: B**, v. 297, p. 116796, 2023.

[37] VLAZAN, P. et al. Exploiting the Bi-doping effect on the properties of $NaNbO_3$ perovskite-type materials. **Chemical Physics**, v. 579, p. 112203, 2024.

[38] HTET, C. S. et al. Local structural mechanism for enhanced energy storage properties in heterovalent doped $NaNbO_3$ ceramics. **Journal of the European Ceramic Society**, v. 44, p. 1597-1609, 2024.

[39] SHI, H. et al. 2-Propanol photodegradation over nitrogen-doped $NaNbO_3$ powders under visible-light irradiation. **Journal of Physics and Chemistry of Solids**, v. 70, p. 931-935, 2009.

[40] VIG, A. S. et al. Pandey, Influence of Ca-doped $NaNbO_3$ and its heterojunction with g-C_3N_4 on the photoredox performance. **Solar Energy**, v. 185, p. 469-479, 2019.

[41] JANA, R. et al. Influence of cationic doping at different sites in $NaNbO_3$ on the photocatalytic degradation of methylene blue dye. **Journal of Sol-Gel Science and Technology**, v. 96, p. 405-415, 2020.

[42] WU, J. et al. Study on the performance of vanadium doped $NaNbO_3$ photocatalyst degradation antibiotics. **Inorganic Chemistry Communications**, v. 131, p. 108669, 2021.

[43] FAROOQ, U. et al. Self-Assembled Interwoven Nanohierarchitectures of $NaNbO_3$ and $NaNb_{1-x}Ta_xO_3$ ($0.05 \leq x \leq 0.20$): Synthesis, Structural, Characterization, Photocatalytic Applications, and Dielectric Properties. **ACS Omega**, v. 7, p. 16952-16967, 2022.

[44] LV, J. et al. Synthesis and Photocatalytic Activities of $NaNbO_3$ Rods Modified by In_2O_3 Nanoparticles. **The Journal of Physical Chemistry C**, v. 114, p. 6157-6162, 2010.

[45] XU, H. et al. Synthesis, characterization and photocatalytic activity of $NaNbO_3$/ZnO heterojunction photocatalysts. **Journal of Alloys and Compounds,** v. 509, p. 9157-9163, 2011.

[46] KUMAR, S. et al. Achieving Enhanced Visible-Light-Driven Photocatalysis Using Type II $NaNbO_3$/CdS Core/Shell Heterostructures. **ACS Applied Materials & Interfaces Journal**, v. 6, p. 13221-13233, 2014.

[47] FAN, M. et al. Excellent Visible-Light-Driven Photocatalytic Performance of Cu_2O Sensitized $NaNbO_3$ Heterostructure. **New Journal of Chemistry**, v. 39, p. 6171-6177, 2015.

[48] SUN, M. et al. Facile fabrication of BiOI decorated $NaNbO_3$ cubes: A p-n junction photocatalyst with improved visible-light activity. **Applied Surface Science**, v. 416, p. 288-295, 2017.

[49] ZHANG, B. et al. Synthesis of $Ag_2O/NaNbO_3$ p-n junction photocatalysts with improved visible light photocatalytic activities. **Separation and Purification Technology**, v. 178, p. 130-137, 2017.

[50] FENG, Y. et al. Chemical Bonds-Conjugated $Ag_2SO_3/NaNbO_3$ Hybrids as Efficient Photocatalysts: In-situ Fabrication, Characterization and Degradation of Rhodamine B and Methyl Orange. **Nano**, v. 7, p. 1850076, 2018.

[51] CHEN, W.; HU, Y.; BA, M. Surface interaction between cubic phase $NaNbO_3$ nanoflowers and Ru nanoparticles for enhancing visible-light driven photosensitized photocatalysis. **Applied Surface Science**, v. 435, p. 483-493, 2018.

[52] QIAO, Y.; MENG, X.; ZHANG, Z. A new insight into the enhanced visible light-induced photocatalytic activity of $NaNbO_3/Bi_2WO_6$ type-II heterostructure photocatalyst. **Applied Surface Science**, v. 470, p. 645-657, 2019.

[53] ZHANG, D. et al. Photocatalytic degradation of ofloxacin by perovskite-type $NaNbO_3$ nanorods modified g-C_3N_4 heterojunction under simulated solar light: Theoretical calculation, ofloxacin degradation pathways and toxicity evolution. **Chemical Engineering Journal**, v. 400, p. 125918, 2020.

[54] TONG, C. et al. Construction of dual ion (Fe^{3+}/Fe^{2+} and Nb^{5+}/Nb^{4+}) synergy and full spectrum 1D nanorod $Fe_2O_3/NaNbO_3$ photo-Fenton catalyst for the degradation of antibiotic: Effects of H_2O_2, $S_2O_8^{2-}$ and toxicity. **Separation and Purification Technology**, v. 261, p. 118269, 2021.

[55] RAJAN, K. D. et al. Piezo-photocatalytic effect of $NaNbO_3$ interconnected nanoparticles decorated $CuBi_2O_4$ nanocuboids. **Materials Letters**, v. 296, p. 129902, 2021.

[56] SHARMA, A. et al. $NaNbO_3$ Nanorods: Photopiezocatalysts for Elevated Bacterial Disinfection and Wastewater Treatment. **ACS Omega**, v. 7, p. 7595-7605, 2022.

[57] SHARMA, A. et al. $NaNbO_3$/ZnO piezocatalyst for non-destructive tooth cleaning and antibacterial activity. **iScience**, v. 25, p. 104915, 2022.

[58] MIN, J. et al. Construction of NaNbO3/CdS nanorods composites with pyroelectric effect for enhanced pyrocatalytic and antibacterial activity under room-temperature cold-hot cycles. **Colloids and Surfaces A: Physicochemical and Engineering Aspects**, v. 650, p.129529, 2022.

[59] ZHANG, L. et al. Novel $NaNbO_3$-based, ferroelectric ceramics with excellent polarization and electric potential for antibacterial applications. **Materials Today Physics**, v. 49, p.101583, 2024.

[60] UMMER, R. P. et al. Exploring the optical limiting, photocatalytic and antibacterial properties of the $BiFeO_3$–$NaNbO_3$ nanocomposite system. **RSC Advances**, v. 11, p. 8450-8458, 2021.

[61] CHATTERJEE, A. K.; CHAKRABORTY, R.; BASU, T. Mechanism of antibacterial activity of copper nanoparticles. **Nanotechnology**, v. 25, p. 135101, 2014.

[62] ALI, S. et al. A Comprehensive Mechanistic Antibacterial and Antibiofilm Study of Potential Bioactive $((BpA)_2bp)$Cu/Zn Complexes via Bactericidal Mechanisms against Escherichia coli. **Molecules**, v. 28, p. 2215, 2023.

[63] ELMEHRATH, S. et al. Antibacterial efficacy of copper-based metal-organic frameworks against Escherichia coli and Lactobacillus. **RSC Advances**, v. 14, p. 15821-15831, 2024.

[64] JACOBS, A. et al. Copper-Doped Biphasic Calcium Phosphate Powders: Dopant Release, Cytotoxicity and Antibacterial Properties. **Materials**, v. 14, p. 2393, 2021.

[65] MAHLANGU, T et al. Preparation of Copper-Decorated Activated Carbon Derived from Platamus occidentalis Tree Fiber for Antimicrobial Applications. **Materials**, v. 15 p. 5939, 2022.

[66] AZIZOVA, L. et al. Argatroban and copper-modified polymers with improved thromboresistance and antimicrobial properties. **Journal of Materials Research**, v. 39, p. 2332-2347, 2024.

[67] DINKU, D. et al. Desalegn, Synthesis, Molecular Docking, and antibacterial evaluation of Quinoline-Derived Ni(II), Cu(II) and Zn(II) complexes. **Results in Chemistry**, v. 8, p. 101562, 2024.

[68] DOS SANTOS, A. N. et al. Zn(II) loaded silylated bentonites as antibacterial materials: Influence of the surface functionalization. **Applied Surface Science**, v. 659, p. 159878, 2024.

[69] KUMAR, A. et al. In vitro anti-microbial, DNA-binding, In silico pharmacokinetics and molecular docking studies of Schiff-based Cu(II), Zn(II) and Pd(II) complexes. **Journal of Molecular Structure**, v. 1315, p. 138695, 2024.

[70] MORATILLA, S. M. et al. Zinc(II) Iminopyridine Complexes as Antibacterial Agents: A Structure-to-Activity Study. **International Journal of Molecular Sciences**, v. 25, p. 4011, 2024.

[71] LUO, X. et al. A blue fluorescent waterborne polyurethane-based Zn(II) complex with antibacterial activity. **e-Polymers**, v. 24, p. 20230059, 2024.

[72] GIORGI, G.; YAMASHITA, K. Organic-inorganic halide perovskites: an ambipolar class of materials with enhanced photovoltaic performances. **Journal Materials Chemistry A**, v. 3, p. 8981-8991, 2015.

[73] KATZ, E. A. Perovskite: Name Puzzle and German-Russian Odyssey of Discovery. **Helvetica Chimica Acta**, v. 103, p. 2000061, 2020.

[74] MAYRINCKA, C; FONSECA, A. F. V.; SCHIAVON, M. A. Nanocristais de perovskitas coloidais: histórico, propriedades e aplicações. **Química Nova**, v. 43, p. 1264-1276, 2020.

[75] NANA, H.-S.; HUA, X.-Y.; TIAN, H.-W. Recent advances in perovskite oxides for anion-intercalation supercapacitor: A review. **Materials Science in Semiconductor Processing**, v. 94, p. 35-50, 2019.

[76] LI, L. et al. Recent Advances in Perovskite Photodetectors for Image Sensing. **Small**, v. 17, p. 2005606, 2021.

[77] ALOM, M. S.; KANANKE-GAMAGE, C. C. W.; RAMEZANIPOUR, F. Perovskite Oxides as Electrocatalysts for Hydrogen Evolution Reaction. **ACS Omega**, v. 7, p. 7444-7451, 2022.

[78] ZHANG, L. et al. Advances in the Application of Perovskite Materials. **Nano-Micro Letters**, v. 15, p. 177, 2023.

[79] LEE, G. H. et al. Recent Advances in Patterning Strategies for Full-Color Perovskite Light-Emitting Diodes. **Nano-Micro Letters**, v. 16, p. 45, 2024.

[80] SINGH, M.; AKASH; TIWARI, J. P. Solar Cells Based on Pb-Free and Perovskite-Inspired Materials: Futuristic of Perovskite Solar Cells. **ACS Applied Energy Materials**, v. 7 p. 10212-10229, 2024.

[81] TIWARI, B.; BABU, T.; CHOUDHARY, R. N. P. Piezoelectric lead zirconate titanate as an energy material: A review study. **Materials Today: Proceedings**, v. 43, p. 407-412, 2021.

[82] MEGDICH, A.; HABIBI, M.; LAPERRIÈRE, L. A review on 3D printed piezoelectric energy harvesters: Materials, 3D printing techniques, and applications. **Materials Today Communications**, v. 35, p. 105541, 2023.

[83] MIYASAKA, T. et al. Perovskite Solar Cells: Can We Go Organic-Free, Lead-Free,
and Dopant-Free? **Advanced Energy Materials**, v. 10, p. 1902500, 2020.

[84] MAGDALIN, A. E. et al. Development of lead-free perovskite solar cells: Opportunities, challenges, and future technologies. **Results in Engineering**, v. 20, p. 101438, 2023.

[85] JIAJIA SUO, J; PETTERSSON, H.; YANG, B. Sustainable Approaches to Address Lead Toxicity in Halide Perovskite Solar Cells: A Review of Lead Encapsulation and Recycling Solutions. **EcoMat**, v. 7, p.12511, 2025.

[86] LI, W. et al. Mitigating Lead Toxicity in Halide Perovskite Solar Cells: Strategies for Sustainable Development. **Inorganics**, v.13, p.123, 2025.

[87] ZUBAIRI, H. et al. Current development, optimization strategies and future perspectives for lead-free dielectric ceramics in high field and high energy density capacitors. **Chemical Society Reviews**, v. 53, p. 10761-10790, 2024.

[88] TROLIER-MCKINSTRY, S.; RANDALL, C. A. Movers, shakers, and storers of charge: The legacy of ferroelectricians L. Eric Cross and Robert E. Newnham. **Journal of the American Ceramic Society**, v. 100, p. 3346-3359, 2017.

[89] JIANG, J. Enhanced energy storage properties of lead-free $NaNbO_3$-based ceramics via A/B-site substitution. **Chemical Engineering Journal**, v. 422, p. 130130, 2021.

[90] WANG, L. et al. Large piezoelectricity in $NaNbO_3$-based lead-free ceramics via tuning oxygen octahedral tilt. **Materials Horizons**, v. 9, p. 1002-1009, 2022.

[91] SARANAYA, K. et al. Fabrication of nanoporous sodium niobate coating on 316L SS for orthopedics. **Ceramics International**, v. 43, p. 11569-11579, 2017.

[92] NAWAZ, M.; ALMOFTY, S. A.; QURESHI, F. Preparation, formation mechanism, photocatalytic, cytotoxicity and antioxidant activity of sodium niobate nanocubes. **PLoS ONE**, v. 13, p. 0204061, 2018.

[93] BOUGOFFA, A. et al. Photovoltaic properties of new solar cell based on ideal cubic $NaNbO_3$ thin films: a combined experimental and density functional theory study. **RSC Advances**, v. 13, p. 30092, 2023.

[94] DO, M.-T. et al. Stabilized Ferroelectric $NaNbO_3$ Nanowires for Lead-Free Piezoelectric Nanocomposite Applications. **ACS Applied Nano Materials**, v. 6, p. 21027-21036, 2023.

[95] YANG, T. et al. Enhanced piezoelectric catalytic properties of $NaNbO_3$ powder by defects engineering. **Applied Surface Science**, v. 628, p. 157363, 2023.

[96] SOHELI, S. N. et al. Lead-Free $NaNbO_3$-Based Ceramics for Electrostatic Energy Storage Capacitors. **Ceramics**, v. 7, p. 712-734, 2024.

[97] MEGAW, H. D. The seven phases of sodium niobate. **Ferroelectrics**, v. 7, p. 87-89, 1974.

[98] YUZYUK, Y. I. et al. Modulated phases in $NaNbO_3$: Raman scattering, synchrotron x-ray diffraction, and dielectric investigations. **Journal of Physics: Condensed Matter**, v. 17, p. 4977-4990, 2005.

[99] SHIRATORI, Y. et al. Polymorphism in Micro-, Submicro-, and Nanocrystalline $NaNbO_3$. **The Journal of Physical Chemistry B**, v. 109, p. 20122-20130, 2005.

[100] SHIRATORI, Y. et al. Temperature-induced Phase Transitions in Micro-, Submicro-, and Nanocrystalline $NaNbO_3$. **The Journal of Physical Chemistry C**, v. 111, p. 18493-18502, 2007.

[101] GOUGET, G. et al. Isolating the Two Room-Temperature Polymorphs of $NaNbO_3$: Structural Features, Optical Band Gap, and Reactivity. **ACS Applied Electronic Materials Journal**, v. 1, p. 513-522, 2019.

[102] TEIXEIRA, G. F. et al. On the coexistence of ferroelectric and antiferroelectric polymorphs in $NaNbO_3$ fibers at room temperature. **Journal of Materials Chemistry C**, v. 11, p. 5524-5533, 2023.

[103] HTET, C. S. et al. Local structural mechanism for enhanced energy storage properties in heterovalent doped $NaNbO_3$ ceramics. **Journal of the European Ceramic Society**, v. 44, p. 1597-1609, 2024.

[104] MISHRA, S. K. et al. Competing antiferroelectric and ferroelectric interactions in $NaNbO_3$: Neutron diffraction and theoretical studies. **Physical Review B**, v. 76, p. 024110, 2007.

[105] ZHU, H. et al. Structural Evolution in a Hydrothermal Reaction between Nb_2O_5 and NaOH Solution: From Nb_2O_5 Grains to Microporous $Na_2Nb_2O_6.2/3H_2O$ Fibers and $NaNbO_3$ Cubes. **Journal of the American Chemical Society**, v. 128, p. 2373-2384, 2006.

[106] PAULA, A. J. et al. Microwave-Assisted Hydrothermal Synthesis of Structurally and Morphologically Controlled Sodium Niobates by Using Niobic Acid as a Precursor. **European Journal of Inorganic Chemistry**, v. 8, p. 1300-1308, 2008.

[107] KE, T.-Y. et al. Sodium Niobate Nanowire and Its Piezoelectricity. **The Journal of Physical Chemistry C**, v. 112, p. 8827-8831, 2008.

[108] SHI, H. et al. $NaNbO_3$ Nanostructures: Facile Synthesis, Characterization, and Their Photocatalytic Properties. **Catalysis Letters**, v. 132, p. 205-212, 2009.

[109] YU, A. et al. Surface sprouting growth of $Na_2Nb_2O_6{\cdot}H_2O$ nanowires and fabrication of $NaNbO_3$ nanostructures with controlled morphologies. **Applied Surface Science**, v. 258, p. 3490-3496, 2012.

[110] TEIXEIRA, G. F. et al. Synthesis and Characterization of $NaNbO_3$ Mesostructure by a Microwave-Assisted Hydrothermal Method. **MRS Online Proceedings Library**, v. 1675, p. 145-150, 2014.

[111] SKJÆRVØ, S. L. et al. Understanding the Hydrothermal Formation of $NaNbO_3$: Its Full Reaction Scheme and Kinetics. **Inorganic Chemistry**, v. 60, p. 7632-7640, 2021.

[112] GEDYE, R. et al. The use of microwave ovens for rapid organic synthesis. **Tetrahedron Letters**, v. 27, p. 279-282, 1986.

[113] GIGUERE, R. J. et al. Application of commercial microwave ovens to organic synthesis. **Tetrahedron Letters**, v. 27, p. 4945-4948, 1986.

[114] KOMARNENI, S.; ROY, R.; LI, Q. H. Microwave-hydrothermal synthesis of ceramic powders. **Materials Research Bulletin**, v. 27, p. 1393-1405, 1992.

[115] SUN, J.; WANG, W.; YUE, Q. Review on Microwave-Matter Interaction Fundamentals and Efficient Microwave-Associated Heating Strategies. **Materials**, v. 9, p. 231, 2016.

[116] GABRIEL, C. et al. Dielectric parameters relevant to microwave dielectric heating. **Chemical Society Reviews**, v. 27, p. 213-224, 1998.

[117] ZHU, Y.-J.; CHEN, F. Microwave-Assisted Preparation of Inorganic Nanostructures in Liquid Phase. **Chemical Reviews**, v. 114, p. 6462-6555, 2014.

[118] BHATTACHARYA, M.; BASAK, T. A review on the susceptor assisted microwave processing of materials. **Energy**, v. 97, p. 306-338, 2016.

[119] MAKSIMOVA, V. D.; MESKINA, P. E.; CHURAGULOV, B. R. Microwave-Assisted Hydrothermal Synthesis of Fine $BaZrO_3$ and $BaHfO_3$ Powders. **Inorganic Materials**, v. 43, p. 988-993, 2007.

[120] ZHANG, Y.-T. et al. Microwave-assisted synthesis of Zr-based metal-organic polyhedron: Serving as efficient visible-light photocatalyst for Cr(VI) reduction. **Inorganica Chimica Acta**, v. 543, p. 121204, 2022.

[121] SMIJOVÁ, J. et al. Nano-ZnS photocatalytically active both under UV and solar radiation: A comparison of conventional and microwave-assisted hydrothermal syntheses with various reaction conditions. **Journal of Alloys and Compounds**, v. 976, p. 173302, 2024.

[122] ALEXANDRE, M. et al. Piezoelectric properties of polymer/lead-free ceramic composites. **Phase Transitions**, v. 89, p. 708-716, 2016.

[123] JUNG, J. H. et al. In Situ Observation of Dehydration-Induced Phase Transformation from $Na_2Nb_2O_6.H_2O$ to $NaNbO_3$. **The Journal of Physical Chemistry C**, v. 116, p. 22261-22265, 2012.

[124] JUNG, J. H. et al. Lead-Free $NaNbO_3$ Nanowires for a High Output Piezoelectric Nanogenerator, **ACS Nano**, v. 5, p. 10041-10046, 2011.

[125] PEI, L. et al. The key role of photoisomerisation for the highly selective photocatalytic hydrogenation of azobenzene to hydrazobenzene over $NaNbO_3$ fibre photocatalyst. **Journal of Photochemistry and Photobiology A: Chemistry**, v. 400, p.112655, 2020.

[126] WANG, Y. Growth behavior and controllable morphologies of $NaNbO_3$ superfine particles synthesized by hydrothermal method, **Ceramics International,** v. 44, p. 7276-7279, 2018.

[127] WANG, S. et al. Leadfree sodium niobate nanowires with strong piezo-catalysis for dye wastewater degradation, **Ceramics International**, v. 45, p. 11703-11708, 2019.

[128] ZHANG, D. et al. Low temperature synthesis of ribbon-like orthorhombic $NaNbO_3$ fibers and their photocatalytic activities for H_2 evolution. **RSC Advances**, v. 5, p. 33001-33007, 2015.

[129] TEIXEIRA, G. F. et al. Photoluminescence in $NaNbO_3$ particles and films. **Materials Letters**, v. 139, p. 443-446, 2015.

[130] ZHANG, D. et al. Preparation and characterization of orthorhombic $NaNbO_3$ Long Bar. **Ceramics International**, v. 40, p.14279-14285, 2014.

[131] LIU, Z. et al. Silicone-oil-assisted synthesis of high-quality sodium niobate nanowires. **CrystEngComm**, v. 19, p. 3553-3556, 2017.

[132] JI, S. et al. Synthesis, Structure, and Piezoelectric Property of Ferroelectric and Antiferroelectric $NaNbO_3$ Nanostructures. **CrystEngComm**, v. 16, p. 7598-7604, 2014.

[133] LIU, L. et al. Temperature-induced solid-phase oriented rearrangement route to the fabrication of $NaNbO_3$ nanowires. **Chemical Communications**, v. 46, p. 427-429, 2010.

[134] LV, M.; WANG, H.; SHI, H. Construction of Z-scheme $BiVO_4/NaNbO_3$ piezo-photocatalyst with improved carrier separation for efficient removal of tetracycline. **Colloids and Surfaces A: Physicochemical and Engineering Aspects**, v. 679, p. 132579, 2023.

[135] YAN, X. et al. Synergetic piezo-photocatalytic effect in $NaNbO_3/WO_3$ photocatalyst for RhB degradation. **Inorganic Chemistry Communications**, v. 158, p. 111510, 2023.

[136] SUN, S. et al. Engineering ZIF-8 modified $NaNbO_3$ perovskite photocatalyst toward high efficiency photocatalysis based on piezo-phototronic effect. **Catalysis Communications**, v. 181, p. 106713, 2023.

[137] FUJISHIMA, A.; HONDA, K. Electrochemical Photolysis of Water at a Semiconductor Electrode. **Nature**, v. 238, p. 37-38, 1972.

[138] HISATOMI, T. et al. Photocatalytic water splitting for large-scale solar-to-chemical energy conversion and storage. **Frontiers in Science**, v. 2, p. 1411644, 2024.

[139] LAWRYNOWICZ, A. et al. Self-cleaning and UV-blocking cotton – Fabricating effective ZnO structures for photocatalysis. **Journal of Photochemistry & Photobiology**, A: Chemistry, v. 450, p. 115420, 2024.

[140] ASWINI, R. et al. Revolutionizing microorganism inactivation: Magnetic nanomaterials in sustainable photocatalytic disinfection. **Journal of Environmental Management**, v. 370, p. 122738, 2024.

[141] WANG, Q.-s. et al. Research Progress on Photocatalytic CO_2 Reduction Based on Perovskite Oxides. **Small**, v. 19, p. 2301892, 2023.

[142] NAIR, N. et al. Mechanisms in the photocatalytic breakdown of persistent pharmaceutical and pesticide molecules over TiO_2-based photocatalysts: A review. **Journal of Physics: Condensed Matter**, v. 36, p. 413003, 2024.

[143] LOPES, O. F. et al. Óxidos de nióbio: Uma visão sobre a síntese do Nb_2O_5 e sua aplicação em fotocatálise heterogênea. **Química Nova**, v. 38, p. 106-117, 2015.

[144] AL-MAMUN, M. R.; KADER, S.; ISLAM, M. S.; KHAN, M. Z. H. Photocatalytic activity improvement and application of UV-TiO_2 photocatalysis in textile wastewater treatment: A review. **Journal of Environmental Chemical Engineering**, v. 7, p. 103248, 2019.

[145] BACCARO A. L. B.; GUTZ I.G. R. Fotoeletrocatálise em semicondutores: dos princípios básicos até sua conformação à nanoescala. **Química Nova**, v. 41, p. 326-339, 2018.

[146] BURSTEIN, E. Anomalous Optical Absorption Limit in InSb. **Physical Review**, v. 93, p. 632-633, 1954.

[147] MOSS, T. The interpretation of the properties of indium antimonide. **Proceedings of the Physical Society. Section B**, v. 67, p. 775, 1954.

[148] ZARHRI, Z. et al. Optical measurements and Burstein Moss effect in optical properties of Nb-doped $BaSnO_3$ perovskite. **Micro and Nanostructures**, v. 166, p. 207223, 2022.

[149] BUENO, R. T. et al. Semicondutores heteroestruturados: uma abordagem sobre os principais desafios para a obtenção e aplicação em processos fotoquímicos ambientais e energéticos. **Química Nova**, v. 42, p. 661-675, 2019.

[150] WANG, G. et al. Advancements in heterojunction, cocatalyst, defect and morphology engineering of semiconductor oxide photocatalysts. **Journal of Materiomics**, v. 10, 315-338, 2024.

[151] LI, J. et al. Advances in Z-scheme semiconductor photocatalysts for the photoelectrochemical applications: A review. **Carbon Energy**, v. 4, p. 294-331, 2022.

[152] PAULO. K. K.; GIRI, P. K. Plasmonic Metal and Semiconductor Nanoparticle Decorated TiO_2-Based Photocatalysts for Solar Light Driven Photocatalysis. **Encyclopedia of Interfacial Chemistry**, p. 786-794, 2018.

[153] PRAXEDES, R. F. et al. Nanostructured $K_xNa_{1-x}NbO_3$ hollow spheres as potential materials for the photocatalytic treatment of polluted water. **Applied Catalysis B: Environmental**, v. 298, p. 120502, 2021.

Apêndice A: Premiações

1. Trabalho destaque intitulado “Síntese de nanofios de niobato de sódio ($NaNbO_3$) pelo método hidrotérmico assistido por micro-ondas” no XXII Encontro de Pós-Graduação, Universidade Federal de Pelotas, 2020.

2. Trabalho destaque intitulado “Síntese de Nb_2O_5 pelo método hidrotérmico assistido por micro-ondas e seu uso como fotocatalisador para degradação do corante rodamina B” no IV Encontro Multidisciplinar em Ciências Ambientais da Fronteira Sul, Universidade Federal da Fronteira Sul, 2021.

3. Trabalho destaque intitulado “Nanopartículas de niobato de sódio ($NaNbO_3$) e sua atividade fotocatalítica” no XXIII Encontro de Pós-Graduação, Universidade Federal de Pelotas, 2021.

4. Segundo lugar no desafio "Sua tese em 3 min" (3MT), Universidade Federal de Pelotas, 2022.

5. Prêmio Bernhard Gross Award na modalidade pôster com o trabalho *“Fast synthesis of $NaNbO_3$ nanoparticles with high photocatalytic activity*” no XXI B-MRS Meeting, Sociedade Brasileira de Pesquisa em Materiais, 2023.

6. Trabalho destaque intitulado “Nanobastões de $NaNbO_3$ dopados com Cu(II): atividades fotocatalítica e antibacteriana aprimoradas” no XXVI Encontro de Pós-Graduação, Universidade Federal de Pelotas, 2024.

Apêndice B: Outros artigos publicados

1. **D. Fernandes**, C. W. Raubach, P. L. G. Jardim, M. L. Moreira, S. S. Cava, Synthesis of $NaNbO_3$ nanowires and their photocatalytic activity, Ceram. Int. 47 (2021) 10185-10188. https://doi.org/10.1016/j.ceramint.2020.12.070
   QUALIS A1 - MATERIAIS

2. **D. Fernandes,** P. G. Hernandes, M. L. Moreira, C. W. Raubach, P. L. G. Jardim, M. M. Ferrer, E. C. Moreira, V. R. Mastelaro, S. S. Cava, Enhanced sonocatalytic activity of $BaZrO_3$ by insertion of Fe^{3+}, J. Phys. Chem. Solids. 189 (2024) 111972. https://doi.org/10.1016/j.jpcs.2024.111972
   QUALIS A2 - MATERIAIS

3. **D. Fernandes**, P. G. Hernandes, R. D. Carvalho, I. L. Rodrigues, C. W. Raubach, M. L. Moreira, P. L. G. Jardim, M. M. Ferrer, E. C. Moreira, V. R. Mastelaro, C. F. O. Graeff, S. S. Cava, $BaZrO_3$ and its application as a photocatalyst for Rhodamine B removal, Chem. Phys. Lett. 856 (2024) 141633. https://doi.org/10.1016/j.cplett.2024.141633
   QUALIS A3 - MATERIAIS

4. **D. Fernandes**, A. R. N. Stigger, M. L. Moreira, M. M. Ferrer, C. W. Raubach, P. L. G. Jardim, C. F. O. Graeff, V. R. Mastelaro, S. S. Cava, $CaMoO_4$ mesocrystals with sonocatalytic activity for Rhodamine B removal, Inorg. Chem. Commun. 170 (2024) 113221. https://doi.org/10.1016/j.inoche.2024.113221
   QUALIS A3 - MATERIAIS